Quantum Well Intermixing for High Brightness Semiconductor Lasers

by

Craig Lee Walker

Thesis submitted for the degree of

Doctor of Philosophy

to the

Department of Electronics and Electrical Engineering

Faculty of Engineering

University of Glasgow

December, 2002

Abstract

The research presented in this thesis describes how monolithic opto-electronic integration using quantum well intermixing (QWI) can be applied to improve the high brightness performance of single-mode ridge waveguide GaAs/AlGaAs quantum well (QW) lasers. The sputtered SiO_2 QWI technique is explained, and a selective process suitable for device manufacture was demonstrated. This QWI technology was applied to create three distinct devices to address the performance limitations imposed by catastrophic optical damage (COD), spatial mode instability, and overheating.

A non absorbing mirror (NAM) laser technology was successfully demonstrated, capable of significantly improving the COD level of high power lasers prone to mirror degradation. Under pulsed test conditions designed to induce COD, the standard ridge laser suffered COD at 230 mW/facet, compared to 600 mW/facet for the NAM laser, demonstrating an improved COD level by a factor of 2.6. Confirmation of the COD failure mechanism was achieved by facet inspection, and removal of the damaged facets.

Successful demonstration of a high brightness single lateral mode ridge laser with a self-aligned buried heterostructure defined by QWI was achieved. The device benefits from de-coupling of the optical and electrical confinement, allowing enhanced fundamental lateral mode operation up to higher powers; the buried heterostructure improves the lateral mode discrimination, thus suppressing higher order modes. Comparison of the standard ridge laser and the buried heterostructure ridge laser for ridge widths of 5 μm clearly demonstrated the improvement gained; the standard ridge laser was too wide to operate in the fundamental mode, whereas the buried heterostructure ridge laser showed dominantly single-mode operation up to 130 mW/facet.

Investigation of a multi-mode interference coupled array laser using QWI to monolithically integrate active and passive waveguide sections was performed. Although in theory the device offers excellent performance, experimental results were not as initially hoped for. The device showed unstable operation, with a lack of phase locking, suggesting there was no "self-adjustment" phenomenon, and highlighting the crucial role of directional coupling between the amplifiers to stabilise the device.

Acknowledgments

First and foremost, I would like to express my sincere gratitude to John Marsh and Catrina Bryce for their immense help, guidance and encouragement over the course of this PhD work.

I would also like to thank all the staff and students within the department for their assistance and friendship. In particular, I am indebted to past and present members of the Optoelectronics Research Group.

Financial support was provided by the Engineering and Physical Sciences Research Council (EPSRC) and the Defence Evaluation Research Agency (DERA), and I would like express my gratitude to both of these.

Finally, on a personal note, I would like to acknowledge my family and friends for their support, and for helping me keep everything in perspective. Special thanks go to the past and present inhabitants of my office for providing entertainment, refreshments, and for helping me maintain my sanity during the past few months: H. Chong, D. Ross, T. Drysdale, S. Hamill, C. Young, T. Kleckner, C. Haydoon, and S. S. Kim.

Publications

C. L. Walker, A. C. Bryce, and J. H. Marsh, "High Brightness Single-Mode Ridge Laser Utilizing Buried Heterostructure Defined by Quantum-Well Intermixing", *IEEE Photonics Technology Letters*, vol. 14, pp. 1391-1393, October 2002.

C. L. Walker, A. C. Bryce, and J. H. Marsh, "Improved Catastrophic Optical Damage Level From Laser With Nonabsorbing Mirrors", *IEEE Photonics Technology Letters*, vol. 14, pp. 1394-1396, October 2002.

C. L. Walker, A. C. Bryce, and J. H. Marsh, "Improved Lateral Mode Stability From Ridge Laser Using Self-Aligned Buried Heterostructure Defined By Defect Induced Quantum Well Intermixing", *IEEE LEOS Annual Meeting*, paper MK1, Glasgow, November 2002.

C. L. Walker, A. C. Bryce, and J. H. Marsh, "Non Absorbing Mirror Laser With Improved Catastrophic Optical Damage Level", *IEEE LEOS Annual Meeting*, paper ThC2, Glasgow, November 2002.

C. L. Walker, A. C. Bryce, and J. H. Marsh, "Monolithically Integrated Multi-Mode Interferometer Array Laser Using Defect Induced Quantum Well Intermixing", *IEEE LEOS Annual Meeting*, paper ThX4, Glasgow, November 2002.

Contents

Chapter 1

Introduction

Since the birth of the of the semiconductor laser diode in the 1960s, great strides have been made in laser and opto-electronic technology, leading to the successfully applied systems in use today. Even so, the technology still remains largely at a discrete level, limiting potential exploitation. Compare this with electronic integration, where huge technological advances have been driven by the ability to monolithically integrate millions of electronic components onto a single semiconductor chip. Monolithic integration offers tremendous benefits for functionality, performance, robustness, manufacturability, compactness and cost. The issues involved with opto-electronic integration are more complicated than for electronic integration, but the benefits are similar. Although monolithic opto-electronic integration may result in a performance compromise for some of the individual integrated elements, the benefits of integration are great, especially when viewed from a pragmatic perspective. A key technology for monolithic opto-electronic integration is the ability to selectively control the band-gap energy over an entire wafer; this allows the integration of different functional devices on the same chip. Quantum well intermixing (QWI) is such a technology, and has been extensively developed to meet the requirements of monolithic opto-electronic integration. QWI is a post-growth integration technique, where the well is selectively intermixed with the barriers, resulting in a new well profile and associated changes in the band-gap energy and refractive index. Research

into QWI at the University of Glasgow has been actively pursued since the late 1980s, leading to the development of a technique suitable for monolithic integration of III-V opto-electronics, which was used in this research.

Semiconductor laser sources capable of delivering high power are increasingly demanded by the opto-electronics industry, and have found use in applications including optical disk storage, communications, material processing, topographical imaging, medicine and as optical pump sources. High brightness semiconductor lasers are a subset of high power lasers, but with the emphasis on the *quality* of the light generated, typically giving a stable single-lobed beam profile. Although such lasers have requirements dependent upon the specific application, these lasers tend to have performance limitations outlined below; these limitations are described later in the thesis.

- Mirror degradation leading to catastrophic optical damage (COD)
- Spatial mode instability
- Thermal accumulation (overheating)

The research presented in this thesis was performed in collaboration with DERA (now QinetiQ) under the EPSRC 'Optoelectronic Systems Integration' project 'Scanbeam'. The objective of the Scanbeam project was to demonstrate the technology and concepts necessary to develop monolithically integrated beam steerable laser sources for applications including LIDAR (LIght Detection And Ranging). High brightness semiconductor laser sources are required for such systems, and moreover are increasingly demanded in other opto-electronic applications. Researchers at DERA were also interested in multi-mode interference (MMI) couplers and their ability to coherently couple an array of laser elements, hence the motivation for investigating this device. Since the aim of the Scanbeam project was to demonstrate the technology, the material system chosen was GaAs/AlGaAs as this is more mature than other III-V opto-electronic materials.

This thesis describes the research and development of high brightness index-guided GaAs/AlGaAs semiconductor lasers benefiting from the application of QWI technology to address the laser performance limitations. As explained in chapters 4, 5 and 6, three distinct devices were investigated, all of which apply QWI to standard ridge laser technology. The emphasis of this research was on using the QWI technology to demonstrate improved laser performance, but in doing so naturally leads to a greater understanding of the technology. The chapter outline of the thesis is indicated below, including a brief description of the novel devices investigated.

Chapter 2: "Single-Mode Ridge Waveguide Laser"

Since this research was based around applying the QWI technology to index-guided GaAs/AlGaAs quantum well ridge lasers, chapter 2 explains ridge laser technology, including such issues as lateral mode control, waveguide modelling, laser design, fabrication and characterisation. The concepts explained in this chapter form the basic building blocks used by the more advanced lasers developed in chapters 4, 5 and 6.

Chapter 3: "Quantum Well Intermixing"

Quantum well intermixing is described in chapter 3, including an overview of the various technologies, and experiments performed during this research. This chapter also outlines alternative band-gap engineering techniques for monolithic opto-electronic integration.

Chapter 4: "Non Absorbing Mirror Ridge Laser"

This chapter describes the application of the QWI technology to the facet region of a ridge laser to form a non absorbing mirror (NAM) for suppressing facet degradation, consequently increasing the COD power level. The origins of mirror degradation in the GaAs/AlGaAs system are explained, followed by a discussion of the alternative methods used

to suppress degradation. Development and characterisation of the NAM laser is then described, highlighting the improvement gained.

Chapter 5: "Buried Heterostructure Ridge Laser"

A novel high brightness single-mode ridge laser utilizing a self-aligned buried heterostructure defined by QWI is described in chapter 5. This device benefits from independent control of the electrical and optical confinement, which consequently allows modification of the lateral gain profile to suppress higher order lateral modes and thus stabilize fundamental spatial mode operation.

Chapter 6: "Multi-Mode Interference Coupler Array Laser"

Chapter 6 describes the investigation of a novel array laser using a MMI coupler, which has the potential to coherently lock an array of laser elements, suitable for generating a large optical power in a stable fundamental spatial mode. The fact the light is generated by multiple elements means that the device has the potential to reduce overheating problems.

Chapter 7: "Conclusions and Future Work"

Finally, chapter 7 gives the conclusions to the research, and possible further work.

Chapter 2

Single-Mode Ridge Waveguide Lasers

2.1 Introduction

As explained in chapter 1, lasers operating in a single spatial mode are highly desirable devices. Obtaining stable single-mode operation requires careful design and fabrication of the laser. Deterioration of the optical mode is highly undesirable, thus appropriate strategies must be adopted. This chapter explains the design, fabrication and characterisation of edge-emitting single-mode ridge waveguide lasers. For edge-emitting lasers, obtaining single-mode operation in the vertical direction is relatively easy as it is determined by the epitaxial layer design which can be grown accurately; the problem is obtaining single-mode operation in the lateral direction. Section 2.2 describes the difficulties involved in obtaining lateral single-mode operation, and how this can be achieved by lateral mode control. A simple model of a semiconductor laser-diode is introduced in section 2.3. This model and its associated equations explain the basics of the laser operation, and are useful when examining more complicated situations and analysing laser performance. Section 2.4 describes the epitaxial material used in this research and its performance. Since the ridge laser investigated is based around a single-mode index guided waveguide structure, the design and simulation of this waveguide is discussed in section 2.5. Fabrication of the laser is described in section 2.6. Laser characterisation and

evaluation are covered in section 2.7. Conclusions from this chapter are drawn in section 2.8.

Figure 2.1 shows a schematic of the ridge waveguide laser investigated in this research. A ridge is etched into the semiconductor wafer to provide the lateral optical and electrical confinement. Since the effective index is greater under the ridge than under the etched region, lateral waveguiding takes place. Achieving single-mode propagation in the lateral direction requires an appropriate ridge width and height to be chosen, such that higher order modes are cut-off and not supported by the waveguide. Section 2.5 describes modelling performed to determine an appropriate ridge width and height to give single-mode operation. The waveguiding mechanism in the vertical direction is determined by the wafer structure. Injection of current into the quantum wells (QWs) provides the gain. The laser mirrors are formed by cleaved facets.

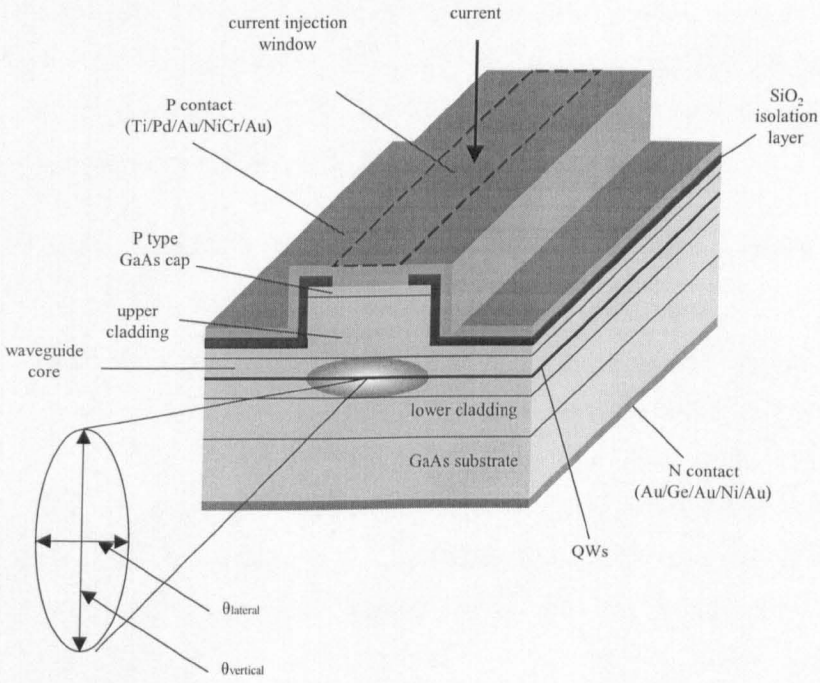

Figure 2.1: Ridge waveguide laser. The etched ridge provides the lateral index step needed for waveguiding, and the current aperture for defining the gain region.

2.2 Lateral Mode Control of Semiconductor Laser

Lateral mode control of edge-emitting semiconductor lasers is essential to obtain stable operation in a single spatial mode. Instability of the lateral mode can result in a kink in the light-current characteristic, and deformation of the optical mode and laser beam profile. Achieving single lateral mode operation is far from trivial, and becomes especially difficult when high output powers are required. Single-mode operation in the vertical direction is much easier to obtain since the waveguide structure is defined by the epitaxial wafer growth, which allows thin layers of accurate material composition (and hence refractive index) to be chosen such that higher order modes are cut-off. Furthermore, since the QWs are usually in the centre of the waveguide core layer, the modal overlap and hence modal gain of the fundamental mode is considerably greater than that of higher order modes, enhancing single-mode operation.

Semiconductor laser diodes are based around a waveguide structure to guide the light. As explained by Kobayashi (1989), there are three possible regimes for waveguiding in a semiconductor laser: 1) gain induced waveguides, 2) refractive index induced waveguides, 3) intermediate waveguides having both gain and refractive index guiding mechanisms. The type of guiding used has a strong impact on the lateral mode stability.

2.2.1 Gain Induced Waveguiding and Lateral Mode Instability

Gain guided lasers are simple to fabricate, and usually consist of a stripe contact to define where current is injected, and therefore the gain region. Due to their relative simplicity, they were investigated in the early stages of laser diode development. Light is guided in the region of high gain; any light travelling in an un-pumped region will experience loss, and therefore will not be guided. The main problem with gain guided lasers is that the optical mode, gain, refractive index and carrier density profiles are strongly dependent upon each other [Carlson (1994), Kobayashi (1989)]; as the carrier density decreases, the refractive index increases. Initially, due to the gain profile, the optical mode is in the centre of the stripe, which causes increased carrier

consumption and spatial hole burning in this region, which consequentially flattens the gain profile and therefore weakens the guiding mechanism that holds the lateral mode in place. A common phenomenon gain guided lasers experience is filamentation, where a self-focussing effect causes deterioration and dynamic instability of the lateral mode [Carlson (1994), Lang *et al* (1994), Kobayashi (1989)]. Any slight asymmetry or imperfection within the device can result in distortion of the lateral mode, which may result in an increased optical intensity at a certain point. The increase in the intensity of the optical mode causes increased carrier consumption, with an associated decrease in the carrier density, which consequentially increases the refractive index, and thus more light is guided through this region, providing a positive feedback effect. This self-focussing effect causes distortion of the lateral mode, and can result in the optical mode shifting towards the stripe edge. This lateral mode deformation means that the optical mode receives less gain than when it was in the centre of the stripe, reducing the lasing efficiency, which results in a kink in the light-current characteristic. In addition to this mode deformation, the laser may also support high order lateral modes, the excitation of which also results in a kink, and deformation of the optical mode and beam, which may now become multi-peaked. Although decreasing the stripe width reduces the lateral mode instability and hence increases the kink power level, the relationship between the optical mode, gain, refractive index and carrier density makes the gain guided laser a poor candidate for achieving high power in a stable single lateral mode [Carlson (1994), Kobayashi (1989)].

2.2.2 Refractive Index Induced Waveguiding

The lateral mode instability problems associated with gain guided lasers can be significantly suppressed by using a laser with a built-in refractive index induced waveguide to guide the optical mode [Kobayashi (1989)]. Since the optical mode is defined by the index induced waveguide rather than the gain, any variations in the gain should not cause deformation of the optical mode, and consequentially self-focussing effects and filamentation can be suppressed. However, a strong index guiding mechanism requires a very narrow waveguide

for single-mode propagation and may mean that the waveguide operates nearer the region where higher order lateral modes can be supported, the excitation of which can become problematic. Choosing an appropriate waveguide regime is therefore important for the laser stability, especially when large output powers are required.

Lasing in a stable single lateral mode can be achieved by suitable design of the index induced waveguide. Various approaches can be used to achieve the lateral index step required for waveguiding, but since this research is concerned with optoelectronic integration using quantum well intermixing, the ridge waveguide laser shown in Figure 2.1 is used. This design avoids the need for epitaxial regrowth and is also suitable for integration of active and passive waveguides with the same guiding mechanism, therefore allowing almost identical mode profiles in the active and passive sections. The ridge waveguide structure is relatively wide, hence the index contrast required for single-mode operation is small, and consequently since the laser is an active device, the gain will have an influence on the waveguiding. Therefore, both gain and index mechanisms are involved in the waveguiding, thus the laser operates in the intermediate waveguiding regime.

2.3 Laser Model

Figure 2.2 shows the main elements of a semiconductor laser diode. Light is guided in the waveguide core, which has upper and lower cladding layers of a lower refractive index. Two partially reflecting mirrors reflect incident light from the cavity back into the cavity. Part of the light is transmitted by the partially reflecting mirrors, thus forming the laser light output. From an electrical point of view the laser diode is essentially a P-I-N structure. Carriers are injected from the p and n-type regions into the intrinsic gain region (a quantum well in this case), where radiative recombination of electron-hole pairs generates photons. The optical mode in the waveguide interacts with the gain region, generating stimulated emission of radiation. Since only a part of the optical mode overlaps with the gain, the modal gain is determined by the

gain of the QW and the overlap of the mode with the QW. During lasing, the optical mode travels back and forth along the length of the cavity, where the mirror and modal losses are counterbalanced by the gain provided by the QW.

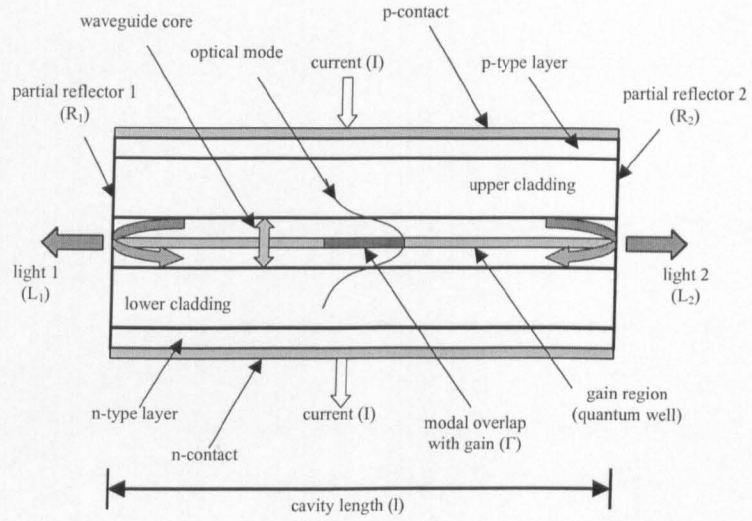

Figure 2.2: Simple side view schematic of semiconductor laser diode.

Figure 2.3 shows an illustration of a laser diode light-current (L-I) characteristic. As the current is increased, the gain increases, and eventually at the threshold current (I_{th}), the laser gain and losses counterbalance each other. Increasing the current beyond the threshold current results in laser emission.

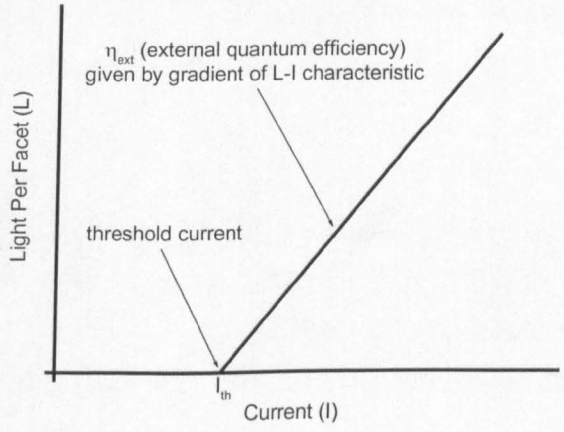

Figure 2.3: Light-current (L-I) characteristic of laser. The intercept on the current axis gives the threshold current, and the gradient the external quantum efficiency.

Assuming a linear L-I characteristic, above threshold the light power per facet (L_{facet}) is given by Eq. 2.1.

$$L_{facet} = (I - I_{th})\frac{dL_{facet}}{dI} \qquad Eq.(2.1)$$

The external quantum efficiency (η_{ext}), defined as the ratio of emitted photons to injected electrons, can be extracted from the gradient of the L-I characteristic, as shown in Eq. 2.2. An alternative name for the external quantum efficiency is the differential quantum efficiency. Eq 2.2 is derived by converting the emitted light per unit time into a number of photons, and the injected current per unit time into a number of electrons, inserting the appropriate constants as required. L_{total} is the total light power emitted from both facets of the laser, and assuming each facet has the same reflectivity, L_{total} is twice L_{facet}. In Eq 2.2, q is the electronic charge magnitude, h is Planck's constant, ν is the frequency of the emitted light, which can be determined from the speed of light (c), and light wavelength (λ).

$$\eta_{ext} = \frac{emitted\ photons}{injected\ electrons} = \frac{q}{h\nu}\frac{dL_{total}}{dI} = 2\frac{q\lambda}{hc}\frac{dL_{facet}}{dI} \qquad Eq.(2.2)$$

Calculation of the modal gain at threshold can be performed by assuming the relationship shown in Eq. 2.3, where L is the light power, of initial value L_0, g and α are the modal gain and losses respectively, and l is the length the mode has travelled.

$$L = L_0 e^{(g-\alpha)l} \qquad Eq.(2.3)$$

At threshold, the gain counterbalances the mirror and mode losses, resulting in Eq. 2.4, where g_{th} is the modal gain at threshold. Eq. 2.4 also includes the condition when both facet reflectivities are equal, and of value R. At threshold the gain becomes clamped and injection of any further carriers results in laser emission.

$$g_{th} = \alpha + \frac{1}{2l}\ln\left(\frac{1}{R_1 R_2}\right) = \alpha + \frac{1}{l}\ln\left(\frac{1}{R}\right) = \text{modal loss} + \text{mirror loss} \qquad Eq.(2.4)$$

The internal quantum efficiency (η_{int}), defined as the fraction of injected carriers that recombine radiatively, is often of interest when assessing laser performance. Empirical determination of η_{int} can be achieved from evaluation of η_{ext}, which can be calculated from Eq. 2.2. Returning to Eq 2.4, it is apparent that the total loss is the summation of the modal loss and the loss due to the mirrors. The mirror loss corresponds to the light output, therefore dividing the mirror loss by the total loss gives the fraction of generated photons that are emitted by the laser. The external quantum efficiency is equal to the internal quantum efficiency multiplied by the fraction of generated photons that are emitted, giving Eq. 2.5.

$$\eta_{ext} = \eta_{int}\frac{mirror\ \ loss}{total\ \ loss} = \eta_{int}\frac{1/l \ln\left(1/R\right)}{\alpha + 1/l \ln\left(1/R\right)} \qquad Eq.(2.5)$$

Rearranging Eq. 2.5 gives Eq. 2.6. Therefore, plotting $1/\eta_{ext}$ as a function of the laser length (l) allows η_{int} and α to be extracted from the intercept and gradient respectively.

$$\frac{1}{\eta_{ext}} = \frac{1}{\eta_{int}} + \frac{\alpha}{\eta_{int}\ln\left(1/R\right)}l \qquad Eq.(2.6)$$

As explained by McIlroy *et al* (1985), the threshold current density at threshold (J_{th}) can be determined by evaluating the relationship between the modal gain and injected current density. Assuming that there are n wells, each of gain G, then the modal gain is given by Eq. 2.7, where Γ_w is the modal overlap per well (assuming it to be the same for each QW).

$$g = n\Gamma_w G \qquad Eq.(2.7)$$

Assuming that the injected current density is equally split between each well (hence each well has the same carrier density), then the gain of a single well can be approximated by Eq. 2.8, where G_0 and J_0 are temperature dependent constants.

$$G = G_0\left[1 + \ln\left(\frac{J}{nJ_0}\right)\right] \qquad Eq.(2.8)$$

Substituting Eq. 2.7 and 2.8 into the threshold condition (Eq. 2.4) gives Eq. 2.9. Plotting $\ln(J_{th})$ as a function of the inverse length therefore allows the quantum well gain parameter (G_0) to be determined.

$$\ln(J_{th}) = \frac{1}{l}\frac{\ln\left(1/R\right)}{n\Gamma_w G_0} + \frac{\alpha}{n\Gamma_w G_0} + \ln(nJ_0) - 1 \qquad Eq.(2.9)$$

Since an infinitely long cavity is free from mirror losses, the threshold current density for such a cavity (J_∞) is useful for assessing material quality and performance, and is free from variations in the facet reflectivity. Eq. 2.9 can be rewritten as shown in Eq. 2.10, and therefore from the plot of $\ln(J_{th})$ as a function of the inverse length, J_∞ can easily be extracted from the intercept on the $\ln(J_{th})$ axis.

$$\ln(J_{th}) = \frac{1}{l}\frac{\ln\left(1/R\right)}{n\Gamma_w G_0} + \ln(J_\infty) \qquad Eq.(2.10)$$

2.4 Material Design and Performance

Since this research was concerned with the application of the quantum well intermixing (QWI) technology, comparing the relative performance of standard lasers and lasers incorporating QWI was more important than optimising wafer design, and therefore a rather standard wafer structure was used. Table 2.1 shows the typical wafer structure used, though each individual wafer varied slightly due to growth tolerances. The wafers were grown by metal-organic

vapour phase epitaxy (MOVPE) at the III-V growth facility at Sheffield University. The light is guided largely within the 530 nm thick core region, which contains two 10 nm GaAs QWs.

Material	**Thickness**	**Doping / cm^{-3}**	**Comment**
GaAs	100 nm	1×10^{19} Zn	cap layer
$Al_{0.4}Ga_{0.6}As$	1000 nm	7×10^{17} C	upper cladding
$Al_{0.2}Ga_{0.8}As$	250 nm		core/barrier
GaAs	10 nm		QW
$Al_{0.2}Ga_{0.8}As$	10 nm		barrier
GaAs	10 nm		QW
$Al_{0.2}Ga_{0.8}As$	250 nm		core/barrier
$Al_{0.4}Ga_{0.6}As$	1500 nm	1×10^{18} Si	lower cladding
GaAs	500 nm	1.5×10^{18} Si	growth interface
GaAs	~ 500 μm	2×10^{18} Si	substrate

Table 2.1: Wafer design of typical GaAs/AlGaAs DQW laser structure used in this research.

Material performance and quality were characterised by fabricating simple oxide stripe gain guided lasers and extracting the light-current-voltage (L-I-V) characteristics. Since the analysis is statistical, a number of devices of different lengths were used. As explained in section 2.2, and using Eq. 2.6, plotting the inverse of the external quantum efficiency as a function of length allows the internal quantum efficiency and the loss to be determined. The plots obtained typically showed significant scatter, making accurate determination of η_{int} and α difficult, but even so, values for η_{int} and α were normally around 0.9 and 3-4 cm^{-1} respectively. As shown in Eq. 2.10, plotting $\ln(J_{th})$ as a function of the inverse length allows J_∞ and G_0 to be determined. For the wafers used in this research, J_∞ was typically measured to be around 240-270 A/cm^2. The modal overlap per well (Γ_w) can be determined by modelling the waveguide structure (explained in section 2.5), and for this wafer design Γ_w was 0.023.

Assuming a value of 0.3 for the facet reflectivity, G_0 was determined to be in the region of 800 cm^{-1}.

2.5 Design of Single-Mode Index Guided Waveguides

As explained in section 2.2.2, the ridge laser structure is based around an index guided waveguide structure to guide the light. Etching is used to form the ridge. Waveguiding in the lateral direction is achieved as a consequence of the ridge; the effective index underneath the etched region is lower than that underneath the ridge, therefore providing the lateral index step required. Waveguiding in the vertical direction is achieved by the refractive index differences between the AlGaAs layers in the wafer structure. From an optical point of view, the waveguide can be modelled as shown in Figure 2.4. Since the modal overlap with the QW region is small, the QWs have little effect on the waveguiding, and therefore they were not included in the simulation of the waveguide. The refractive index values shown are for 860 nm, and were calculated using a program written by D. Yanson, which was based upon a paper by Deri and Emanuel (1995).

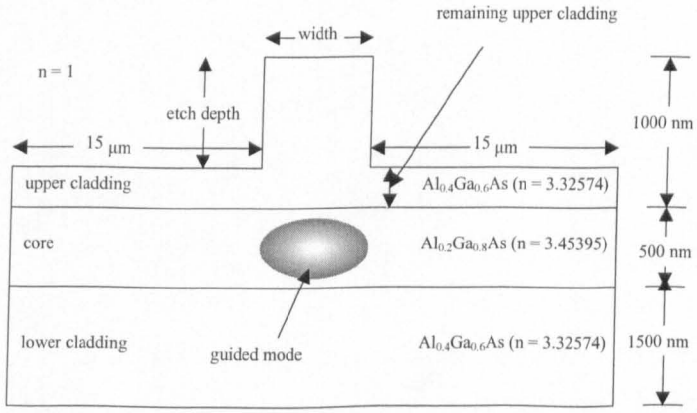

Figure 2.4: model of ridge waveguide structure which provides the index guiding mechanism for the ridge laser. The refractive index steps in the lateral and vertical directions are created as a consequence of the ridge and wafer structure respectively.

Achieving single-mode operation in the lateral and vertical directions requires appropriate waveguide parameters to be chosen to cut-off higher order modes.

Discussion of waveguiding and the conditions necessary to achieve single-mode propagation can be found in a good text book, for example Zappe (1995). As the wave equation cannot be solved analytically, it is often convenient to simulate it numerically on a computer. Simulation of the waveguide structure was performed using a program called FIMMWAVE, by Photon Design. Single-mode operation in the lateral direction requires appropriate values for the waveguide width and thickness of remaining upper cladding (hence etch depth) to be chosen. Figure 2.5 shows the results of simulations performed on the ridge waveguide structure shown in Figure 2.4. Simulations were performed for TE polarisation since this is the lasing polarisation. In the vertical direction the waveguide structure supports only the fundamental mode. The dashed line shows the cut-off condition for higher order lateral modes, hence the waveguide needs to be designed on the single-mode side of this line. The effective index step between the ridge and etched region is determined by the thickness of the remaining upper cladding, the thinner the remaining upper cladding the larger the index step. As the index step increases, the waveguide width must be made narrower to achieve single-mode operation. Therefore, the thinner the remaining upper cladding, the narrower the waveguide must be. As explained in section 2.2.2, it is desirable that there is a strong index guiding mechanism to guide the optical mode, however this means that the waveguide operates nearer the region where higher order lateral modes can be supported. Therefore, returning to Figure 2.5, it is desirable to operate close to the cut-off condition, but on the single-mode side of this condition. The fabrication tolerances must also be considered when deciding upon the waveguide width and thickness of remaining upper cladding. For these reasons, the ridge waveguides investigated in this research were typically 2.5 to 3.0 μm wide, with a corresponding thickness of remaining upper cladding to be close to the cut-off condition, but on the single-mode side of the condition.

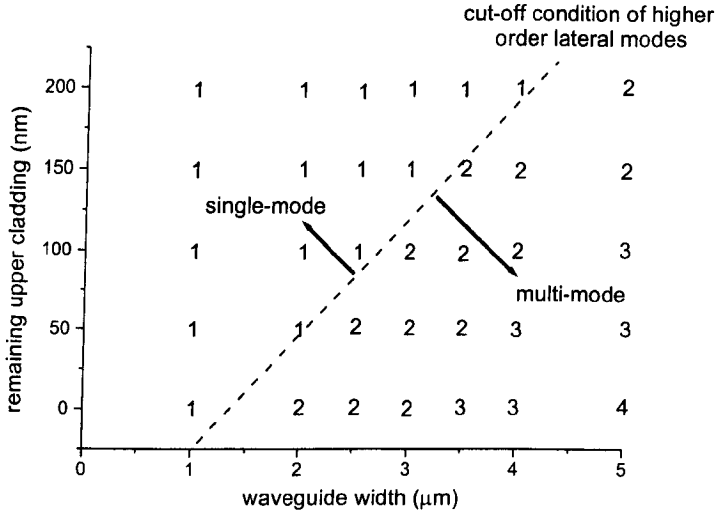

Figure 2.5: Simulation results showing how the waveguide width and thickness of the remaining upper cladding can be chosen to obtain single-mode operation in the lateral direction. The integers shown in the plot indicate the number of lateral modes supported, hence the region of single-mode operation is indicated by the region of 1s. The cut-off condition of higher order lateral modes is indicated by the dashed line.

Figure 2.6 shows the simulated intensity plot for a 2.5 μm wide waveguide with 100 nm of remaining upper cladding in the etched region. Single-mode operation in both the lateral and vertical directions is achieved. The actual ridge waveguides fabricated in this research have similar dimensions to this simulated ridge waveguide. The simulated far-field beam profile from this waveguide is shown in Figure 2.7. Single-mode operation is evident.

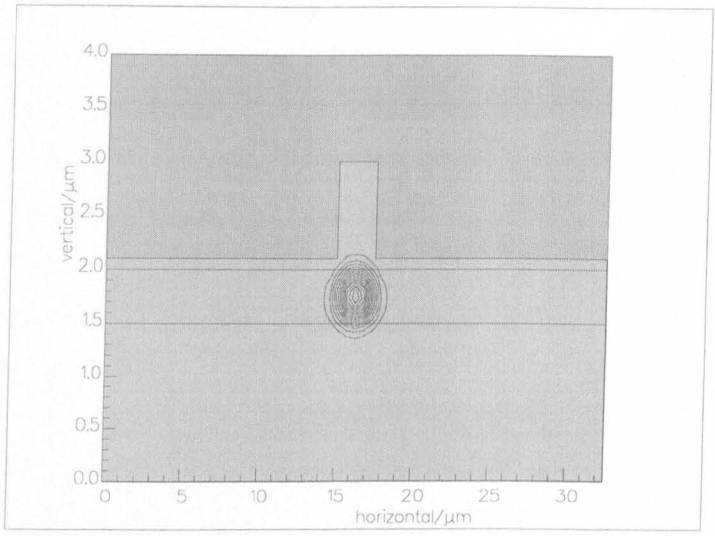

Figure 2.6: Simulated intensity plot of fundamental mode for a 2.5 μm wide waveguide with 100 nm of remaining upper cladding in the etched region. The waveguide gives single-mode operation in the lateral and vertical directions.

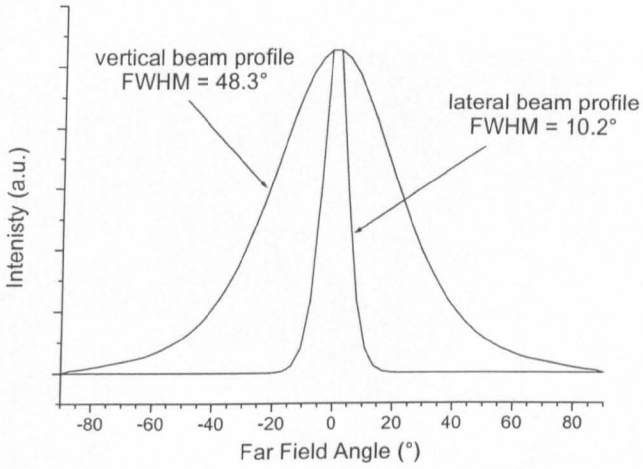

Figure 2.7: Simulated far-field beam profile of fundamental mode from the waveguide shown in Figure 2.6.

2.6 Laser Fabrication

Fabrication of good quality optoelectronic devices is far from trivial, requiring good fabrication processes and experienced personnel. There are many potential pitfalls in the process, which can prove disastrous for device

production. This section summarises the main steps involved in the fabrication of ridge waveguide lasers in the GaAs/AlGaAs system. These fabrication processes are the building blocks used by the more complicated lasers which incorporate QWI, though the details of how QWI is incorporated into the device fabrication sequence is covered later for each specific laser type.

Figure 2.8 shows the unprocessed wafer. The layer structure is a simplification of the actual material shown in Table 2.1, but shows the main elements needed to understand the process. The first step in the fabrication sequence is to cleave a suitably sized sample from the 2 inch wafer. The majority of lasers processed in this research used a sample size of around 12 by 12 mm. The sample is then cleaned in acetone (5 min, ultrasonic bath), methanol (5 min, ultrasonic bath), and finally reverse osmosis (R.O.) water (5 min, running water). After blow-drying the sample, it is then inspected optically under a microscope to ensure it is sufficiently clean, and ready for device processing.

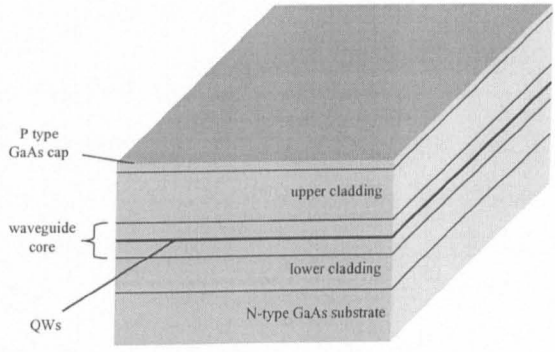

Figure 2.8: Unprocessed wafer showing the layers in the structure.

Since the ridge waveguide is fabricated using reactive ion etching (RIE) [Williams (1990)], it is necessary to form a suitable etch mask. Although photoresist etch masks can be used for this purpose, they can deteriorate during RIE, which results in undesirable ridge roughness. A more durable etch mask is therefore required, and as SiO_2 has proven effective at withstanding the ridge RIE process, this is used for the etch mask. As indicated by Figure 2.9, the etch mask is formed by plasma enhanced chemical vapour deposition

(PECVD) [Williams (1990)] of SiO_2 over the whole sample, followed by photolithographic definition of the stripe and subsequent pattern transfer using RIE. Typically, the thickness of SiO_2 used is around 200 nm or more. Photolithographic definition of the ridge stripe is performed using Shipley S1818 photoresist, having a thickness of 1.8 μm (spin speed of 4000 r.p.m., baked at 90 °C for 30 min). Exposure is performed using a Karl Süss mask aligner fitted with an ultra violet radiation source. The mask plates used for device production are manufactured at Glasgow University using the Electron Beam Lithography (EBL) facility. Following exposure of the sample, pattern development is then performed using Shipley developer. The photoresist stripe is then transferred into the SiO_2 layer using a standard CHF_3 RIE process, the details of which follow.

- Machine manufacturer: Oxford Instruments
- Flow rate of CHF_3: 20 sccm
- Pressure: approximately 18 mTorr
- RF Power: 100 W
- Bias: 390 V
- Etch rate of SiO_2: approximately 30 nm/min

This etch process is anisotropic, giving a near vertical etch profile. Since the etch selectivity of the process to GaAs (defined as the etch rate of SiO_2 divided by that of GaAs) is high (around 7.5), a slight over-etch is used to ensure that all the SiO_2 is removed, without significantly etching the GaAs. Following pattern transfer, the resist stripe is then removed using acetone, leaving just the SiO_2 stripe remaining.

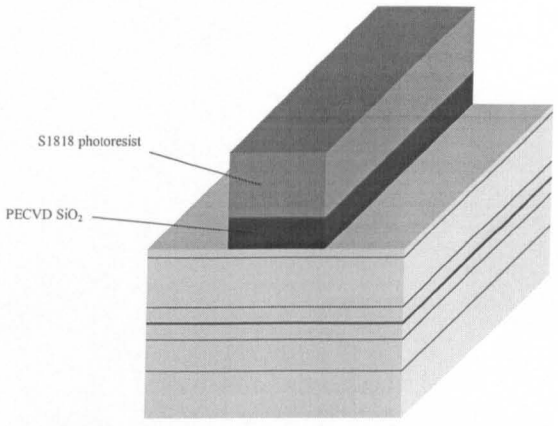

Figure 2.9: After deposition of SiO_2, photolithographic definition of the ridge stripe and subsequent pattern transfer with dry etch. The patterned SiO_2 is used as the etch mask for dry etching the ridge waveguide.

Pattern transfer using a standard $SiCl_4$ RIE process is then performed to etch the ridge, giving the structure shown in Figure 2.10. The etch parameters used in this process are as follows.

- Machine manufacturer: Oxford Instruments
- Flow rate of $SiCl_4$: 9 sccm
- Pressure: around 9 mTorr
- RF Power: 100 W
- Bias: 260 V
- Etch rate of GaAs/AlGaAs: approximately 200 nm/min

This process is highly anisotropic, giving almost vertical side-walls. As explained previously, the thickness of remaining upper cladding is critical to achieve single-mode operation in the lateral direction. In-situ laser interferometry [Hicks *et al* (1994)] is therefore used to achieve control of the etch depth, giving an accuracy of around 50 nm. Following RIE of the ridge, the SiO_2 etch mask is then removed using a HF acid wet etch.

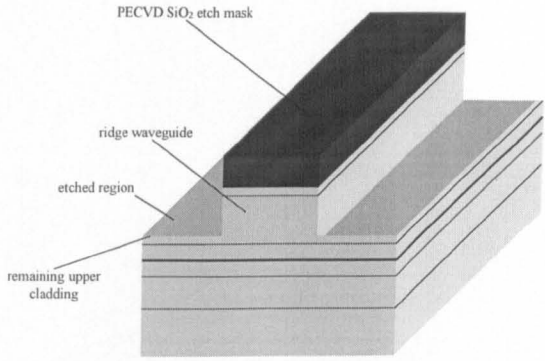

Figure 2.10: After $SiCl_4$ RIE of the ridge waveguide. The etch process gives near vertical side-walls. Accurate control of the etch depth is achieved by using in-situ laser interferometry.

Since current must be injected through the ridge, a current injection window is required. As illustrated by Figure 2.11, this is formed by deposition of a SiO_2 layer followed by photolithographic definition of the window using S1818 photoresist. To ensure sufficient isolation of the etched regions and ridge side-walls, a 300 nm thick layer of PECVD SiO_2 is typically used. The photoresist pattern is then transferred into the SiO_2 layer using standard CHF_3 RIE, followed by a HF acid wet etch. Removal of the photoresist using acetone is then performed, leaving the structure shown in Figure 2.12.

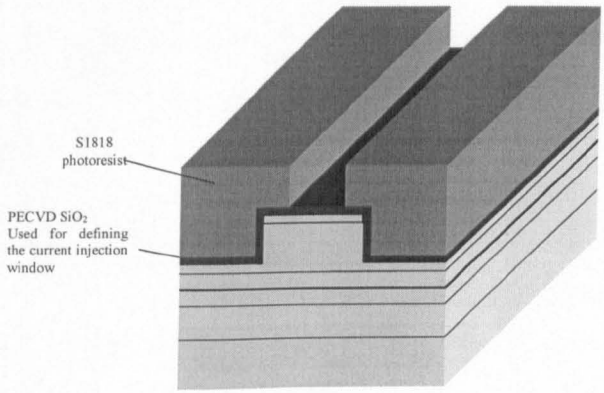

Figure 2.11: After deposition of the PECVD SiO_2 layer and photolithographic definition of the current injection window.

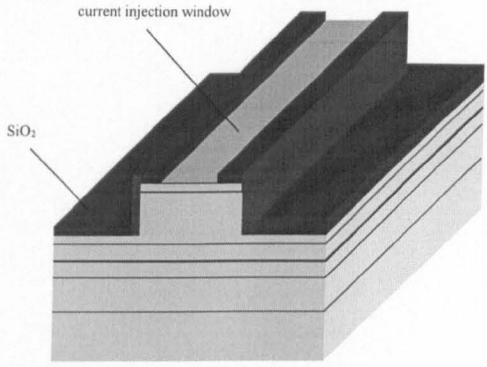

Figure 2.12: After etching of the SiO_2 and removal of the photoresist. Current can only be injected through the window.

Having opened the contact window, the next step is to deposit a p-type contact. However, before this deposition, a de-oxidation step is performed using HCl acid (4 parts water: 1 part HCl) for 30 s, thus ensuring that there are no native oxides on the GaAs surface which would prove detrimental for the contact. After de-oxidation, the sample is loaded into an e-beam evaporator and pumped down. The p-type contact having the following layer sequence is then evaporated: Ti(33 nm)/Pd(33 nm)/Au(240 nm). This metal evaporation is directional, which results in very poor coverage of the ridge side-walls, which can consequently make injection of current into the device difficult. This difficulty is solved by using an angled metal evaporation stage, where the deposition is performed at an angle of 45 ° to vertical, thus ensuring that the ridge side-walls are fully coated with metal. Although initially a Ti(15 nm)/Au(100 nm) deposition was used for this purpose, a NiCr(15 nm)/Au(100 nm) deposition was later found to be superior. Since a single angled deposition covers only one side of the ridge, a second angled deposition is performed to ensure that the other side wall is covered. Figure 2.13 shows the structure after all the p-contact deposition procedures.

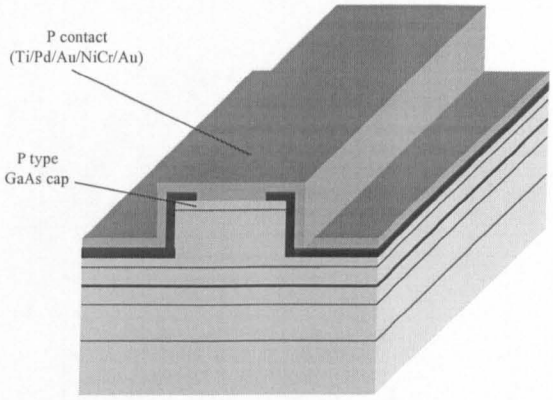

Figure 2.13: After deposition of the p-type contact.

The next fabrication procedure is to thin the sample substrate to make the devices easier to cleave and reduce the substrate resistance. The sample is mounted p-side down on a metal chuck using wax, leaving the n-side exposed, which is subsequently ground down. The thickness of the sample is measured throughout the process, and thinning is stopped once the sample is between 160 and 180 μm thick. After removing the thinned sample from the chuck, cleaning in opti-clear, followed by acetone, methanol and water is performed. The sample is then mounted p-side down on a glass-slide, ready for the n-contact procedure. Before the n-contact is deposited, the sample is de-oxidised as described previously for the p-contact. The n-type contact metallization is perfomed in an e-beam evaporator, and the sequence is as follows: Au(11 nm)/Ge(11 nm)/Au(11 nm)/Ni(14 nm)/Au(240 nm). Following this n-type metallization, the sample is removed from the glass slide. The sample is then annealed at 360 C for 60 s in a rapid thermal annealer to form the ohmic contacts. The final step in the fabrication procedure is to scribe and cleave the individual lasers. Care must be taken to ensure the cleaved facets are of good quality. Figure 2.14 shows the completed ridge waveguide laser. Refer to Figure 2.1 to see the main elements of the device summarised.

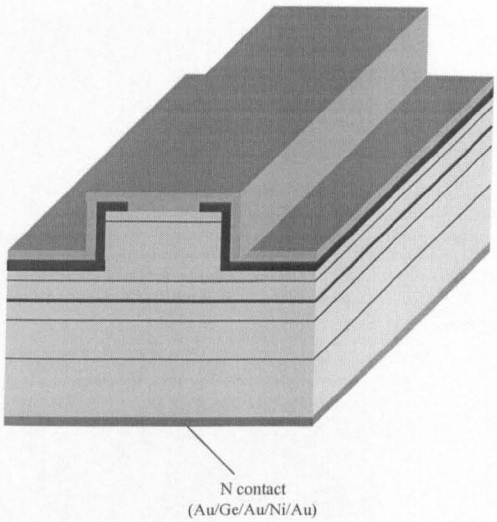

Figure 2.14: Completed device after wafer thinning, deposition of the n-type contact, annealing of the contacts, and device cleaving.

Figure 2.15 shows a scanning electron microscope (SEM) image of a fabricated ridge waveguide laser using the process just described. The ridge has a good etch profile, proving that the SiO_2 etch mask and $SiCl_4$ RIE work well. The ridge is approximately 2.5 μm wide. It is possible to see the waveguide core layer from a slight contrast in the SEM image. The thickness of remaining upper cladding is around 150 nm. Returning to Figure 2.5, it is apparent that these waveguide dimensions are exactly in the desired region of single-mode operation. The SiO_2 isolation layer can clearly be seen, and the current injection window is well aligned in the centre of the ridge. The p-contact metallization clearly covers the side-walls, proving that the angled deposition scheme works.

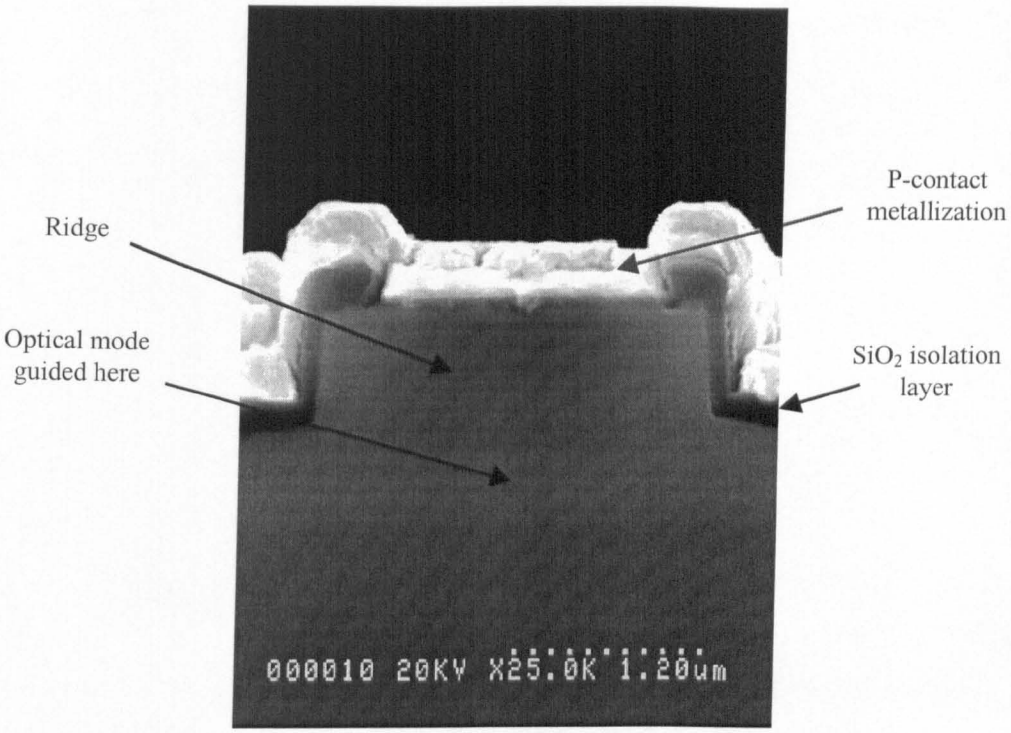

Figure 2.15: SEM image of ridge waveguide laser.

2.7 Laser Characteristics

Figure 2.16 shows the continuous wave (CW) light-current (L-I) characteristic of a 1000 μm long ridge waveguide laser shown in Figure 2.15. Inset shows the lasing spectrum above threshold. The L-I characteristic is linear, and the threshold current of 33 mA and external quantum efficiency of 55 % are reasonable for such a device. This L-I characteristic was obtained using a Newport laser driver and an Anritsu optical power meter.

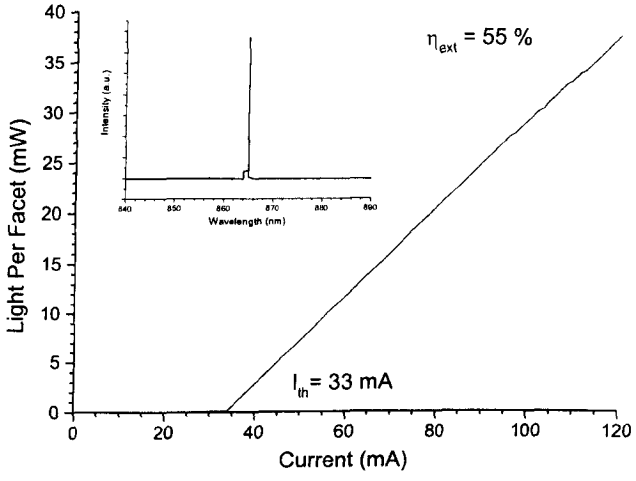

Figure 2.16: CW L-I characteristic of 1000 μm long ridge waveguide laser shown in Figure 2.15. Inset shows the lasing spectrum above threshold.

Figure 2.17 shows the measured far-field beam profile of the ridge waveguide laser. The beam profile was measured using a computer controlled rotational stage; the laser was mounted at the centre of rotation. Light was measured using a photodiode with a narrow slit immediately in front of it. This photodiode/slit was placed an appropriate distance away from the laser (typically 10 cm or more). The combination of fixed photodiode/slit and rotating laser allows the beam profile to be determined. Since this rotational stage is part of the pulsed laser test equipment, the beam profiles were determined under pulsed conditions. The pulsed test set-up uses a box-car system and an Avtech pulsed current source. Lasers are mounted in a simple clip. Typically a 400 ns pulse at 1 kHz repetition frequency is used. The beam profile shown in Figure 2.17 was measured at a drive current of 200 mA. Clearly the profile corresponds to single mode operation in both the lateral and vertical directions, and is in excellent agreement with the simulated result shown in Figure 2.7.

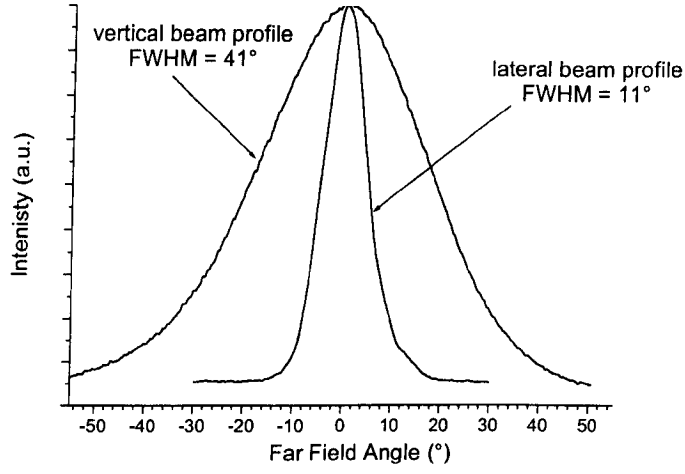

Figure 2.17: Measured far-field beam profile in the lateral and vertical directions. The laser drive current was 200 mA.

The laser characteristics along with the SEM image demonstrate that the laser fabrication procedure has worked well and that the laser operates as intended.

2.8 Conclusions

Edge-emitting lasers operating in a single spatial mode require careful design and fabrication. Gain-guided lasers suffer from poor spatial mode characteristics and stability making them unsuitable for many applications. Lasers based around an index-guided waveguide structure have superior single-mode characteristics and stability. Since the optical mode is defined by the index induced waveguide rather than the gain profile, index-guided lasers do not suffer as much from variations in the gain during operation. Index-guided lasers operating in a single lateral mode require careful design of the structure to ensure that the mode is well guided and that higher order lateral modes are not supported. Fabrication of good quality lasers can be a whole topic in itself, and a suitable process for the fabrication of ridge waveguide lasers in the GaAs/AlGaAs system has been summarised. An SEM image of the device demonstrates the effectiveness of the fabrication process. The light-current and beam profile characteristics from the ridge laser shows that the laser operates

as intended. Single-mode operation in both vertical and horizontal directions was successfully observed, with good agreement to the simulations.

2.9 References

Carlson N. W., "Monolithic Diode-Laser Arrays," published by Springer, Berlin, Germany, 1994.

Deri R. J., and Emanuel M. A., "Consistent formula for the refractive index of $Al_xGa_{1-x}As$ below the band edge," *J. Appl. Phys.*, vol. 77, p. 4667, May 1995.

Hicks S. E., Parkes W., Wilkinson J. A. H., and Wilkinson C. D. W., "Reflectance modeling for *in situ* dry etch monitoring of bulk SiO_2 and III-V multilayer structures," *J. Vac. Sci. Technol.*, B 12 (6), pp. 3306-3310, Nov./Dec. 1994.

Kobayashi K., "Transverse Mode Control in Semiconductor Laser," in "Optoelectronic and Lightwave Communication Systems," edited by Lin C., published by Van Nostrand Reinhold, New York, 1989.

Lang R. J., Mehuys D., Welch D. F., and Goldberg L., "Spontaneous Filamentation in Broad-Area Diode Laser Amplifiers," *IEEE J. of. Quantum Electron.*, vol. 30, pp. 685-693, March 1994.

McIlroy P. W. A., Kurobe A., and Uematsu Y., "Analysis and Application of Theoretical Gain Curves to the Design of Multi-Quantum-Well Laser," *IEEE J. Quantum Electron.*, vol. 21, pp. 1958-1963, Dec. 1985.

Williams R., "Modern GaAs Processing Methods," Artech House, Norwood, MA, USA, 1990.

Zappe H. P., "Introduction to Semiconductor Integrated Optics," Artech House, Norwood, MA, USA, 1995.

Chapter 3

Quantum Well Intermixing

3.1 Introduction

A key technology for monolithic optoelectronic integration of III-V semiconductors is the ability to selectively control the bandgap energy over an entire wafer. This allows lasers of differing wavelength, modulators, photodiodes and low loss passive waveguides to be integrated on the same chip. Given the importance of integration for commercially attractive device manufacture, developing suitable technologies is being researched extensively. This chapter gives a brief overview of monolithic integration methods, followed by more detailed explanation of quantum well intermixing (QWI) technologies, and finally experiments performed in this research using the sputtered SiO_2 approach.

3.1.1 Quantum Well Intermixing:- Principle

Quantum well intermixing is a post-growth integration technique, where the QW is intermixed with the barriers, resulting in a new QW profile, with associated changes in the bandgap energy and refractive index. Marsh (1993) gives a useful discussion of the various QWI techniques. Figure 3.1 shows the principle of QWI. Although the majority of QWI related work is associated with bandgap control, the change in refractive index can also be very useful for making buried waveguides, though MQW structures must generally be used to

achieve a sufficient refractive index step. Intermixing is relatively simple compared to the alternative optoelectronic integration schemes, making it extremely suitable for industrial exploitation. No complex growth or etching is required, meaning that standard QW wafers and planar processing can be used.

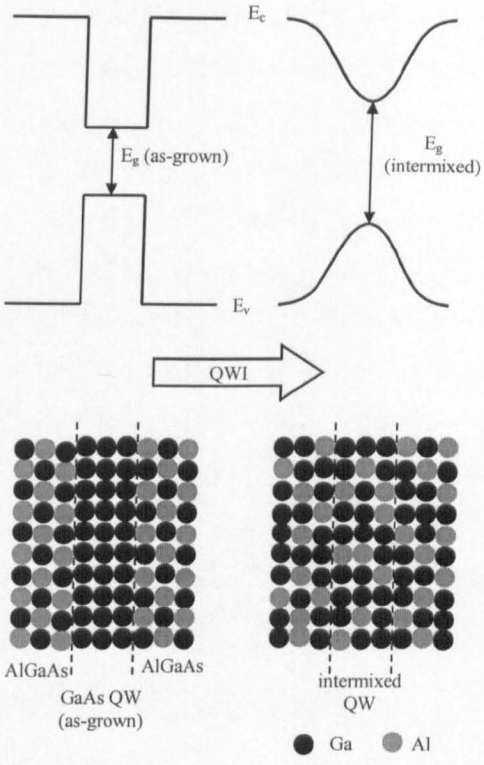

Figure 3.1: Principle of QWI for a single GaAs QW with $Al_{0.5}Ga_{0.5}As$ barriers. For clarity only the group III sublattice is shown. During intermixing, the interdiffusion of Ga from the QW with the Al containing barriers results in the QW becoming disordered, resulting in a non-square QW profile, and associated increase in the bandgap energy.

3.1.2 Requirements

Requirements placed upon the intermixing technology are dependent upon the application, but in general, techniques which offer low optical propagation losses, low free-carrier concentrations and retain high crystal quality are desirable [Marsh (1993)]. Not only does the QWI technique need to achieve these aims, but it should also be commercially attractive.

Since the main application of QWI in this research is concerned with the integration of active (as-grown) and passive (intermixed) waveguides, the prime concern is the propagation loss of the passive waveguides. Achieving low loss requires that there is minimal bandedge absorption in the passive waveguide. For this to occur, the bandgap energy of the passive section must be sufficiently increased with respect to the active (lasing) section. This increase in bandgap energy leads to a blue-shift in the corresponding wavelength. Wavelength dependent loss measurements on intermixed and as-grown waveguides were performed by Cusumano *et al* (1997) and Ooi *et al* (1997). Both these sets of measurements used very similar GaAs/AlGaAs DQW material to that used in this research (see section 2.4 for the material structure used). The laser structures were designed to emit light at around 860 nm. From wavelength dependent plots of the waveguide transmission (or loss), both sets of measurements indicate that a differential blue-shift of around 20 nm between active and passive regions is required to be free from significant bandedge absorption. Therefore, the intermixing technology must be capable of achieving differential blue-shifts of around 20 nm or more, without incurring detrimental side-effects.

3.1.3 Alternative Integration Technologies

3.1.3.1 Selective Area Growth

Selective area growth (SAG) works by controlling lateral variations in the crystal growth using a substrate patterned with a dielectric such as SiO_2 [Kim *et al* (1992), Kudo *et al* (1997)]. Quantum well thickness, and therefore bandgap energy can be laterally controlled. Growth cannot take place on top of the SiO_2, leading to a local increase in the number of growth species, and therefore an enhanced growth rate for regions in the vicinity without dielectric. Areas covered with large amounts of dielectric, leaving only small growth regions, experience a higher growth rate than regions with no, or very little, dielectric coverage. The technique has been applied to fabricate integrated devices such as communication lasers, modulators and passive sections on a

single chip, as well as multi-wavelength DBR laser for wavelength division multiplexing (WDM) [Sasaki *et al* (1994)].

Two different SAG approaches are used, depending on the device application. Opening a narrow slot of around 2 μm in the dielectric layer allows growth of narrow waveguides, removing the need to etch the waveguide structure. This leads to devices with very smooth side walls, but has limited use for integration as only straight waveguides can be grown. Alternatively, larger area growth can be used, allowing better integration of devices, but requiring etching to define the waveguides.

With SAG, only one growth step is required, hence avoiding undesirable regrowth. No high temperature post-growth annealing is necessary. The differences in growth species densities and hence growth rate can lead to non-uniform material composition and quality, for example, optimising a region of thick QW growth (high growth rate) may result in reduced material quality in the regions of thin QW growth (lower growth rate). Furthermore, the interface between thin and thick QW regions can be large (around 100 μm or so), limiting the compactness and potential device applications.

3.1.3.2 Regrowth

The removal of part of an epilayer, followed by a second growth step allows regions of different material to be monolithically integrated. The interface between the original and regrown material can be a severe limitation, with a material mismatch, and consequentially poor device performance. Although potentially very useful in theory, the high demands placed on etching and regrowth, combined with the low yield make this technique undesirable for industrial exploitation.

3.2 QWI Technology

The aim of this section is to outline the main points about the discovery, technology, mechanisms and applications of various intermixing techniques. Since the topic is expanding, and the mechanisms involved are complex, there

is still uncertainty about the detailed mechanisms, but the aim is to outline past thinking, and more recent thinking, thus bringing the reader up to date with the topic. Although this section focuses on the GaAs/AlGaAs system, many of the intermixing concepts introduced can be applied to other III-V systems.

3.2.1 Discovery

Due to the high thermal stability of GaAs/$Al_xGa_{1-x}As$ quantum well heterostructures (QWHs) and superlattices (SLs) against ordinary thermal annealing, selective intermixing was a surprise discovery by Holonyak's group at the University of Illinois in 1980. A detailed account of the discovery is given by Holonyak (1998). The discovery occurred as a consequence of experiments concerned with Zn diffusion into undoped AlAs/GaAs SLs. The SL structure was annealed in a closed ampoule at 575 °C for 4 h with a $ZnAs_2$ source to diffuse Zn through the SL. Following annealing, the substrate was removed, leaving a thin pale yellow sample unlike the thin red as-grown SL, clearly demonstrating a significant change in the material properties. A further diffusion experiment ($ZnAs_2$, 575 °C, 10 min) was performed using Si_3N_4 stripes to mask the Zn diffusion on a AlAs-GaAs SL. After annealing, a shallow angle cross section of the sample was taken to show the contrast between the masked and Zn diffused areas. In areas exposed to Zn diffusion, the SL was compositionally disordered. Masked areas were protected from Zn diffusion and were therefore protected from disordering; the temperature was insufficient to cause disordering of the undoped SL structure. This contrast between the disordered and suppressed (masked) regions clearly demonstrated the ability to selectively intermix QWHs and SLs, a very important discovery for optoelectronics, with many practical uses (the researchers patented the discovery in 1981). Since this intermixing method uses an impurity source for disordering, they named the technique impurity induced layer disordering (IILD), though other groups use the term impurity induced disordering (IID) to mean the same thing.

3.2.2 Native Defect Disordering in AlGaAs

Disordering of heterostructures requires native point defects to facilitate the interdiffusion at elevated temperatures; without these defects the atoms have nowhere to move. This section describes the native defects and their role in heterostructure disordering.

3.2.2.1 Point Defects in AlGaAs

Native point defects in AlGaAs are the column III and V vacancies, interstitials, and antisites as shown in Table 3.1. Understanding the nature of these defects is essential in explaining the mechanisms involved in intermixing, and is also of interest when considering their effect on device characteristics, especially when reducing the device dimensions. Too many point defects may coalesce to form extended defects which are immobile and therefore quench interdiffusion [Venkatesan *et al* (1986)]. A detailed review of point defects and their diffusion in the AlGaAs system is given by Cohen (1997).

	Column III	**Column V**
Vacancy	V_{III} (V_{Ga} or V_{Al})	V_{As}
Interstitial	I_{III} (I_{Ga} or I_{Al})	I_{As}
Antisite	III_{As} (Ga_{As} or Al_{As})	As_{III}

Table 3.1: Native point defects in AlGaAs. Since the column III material can be either Ga or Al, both possibilities are included as well as the generic terms.

3.2.2.2 Disordering Mechanisms

Deppe and Holonyak (1988) proposed a model for the disordering of AlGaAs via column III vacancies and interstitials. They proposed that the interdiffusion rate is dependent on the diffusion rates of the native defects responsible for interdiffusion, and their concentrations. Column III interdiffusion was attributed to both column III vacancies and interstitials, as indicated by Eq. (3.1) and Eq. (3.2), illustrating possible interdiffusion mechanisms.

Column III vacany interdiffusion mechanism:

$$V_{Ga} \Leftrightarrow V_{Ga} + (I_{Al} + V_{Al}) \Leftrightarrow (V_{Ga} + I_{Al}) + V_{Al} \Leftrightarrow V_{Al} \qquad \textit{Eq.}\ (3.1)$$

Column III interstitial interdiffusion mechanism:

$$I_{Ga} \Leftrightarrow I_{Ga} + (V_{Al} + I_{Al}) \Leftrightarrow (I_{Ga} + V_{Al}) + I_{Al} \Leftrightarrow I_{Al} \qquad Eq.\ (3.2)$$

Assuming both mechanisms may be in operation, they proposed Eq. (3.3), where D_{III} is the column III interdiffusion rate, $D_{III(vacancy)}$ and $D_{III(interstitial)}$ are the column III vacancy and interstitial diffusion rates respectively, $[V_{III}]$ and $[I_{III}]$ are the concentrations of the column III vacancies and interstitials respectively, f_1 and f_2 are constants.

$$D_{III} = f_1 D_{III(vacancy)} [V_{III}] + f_2 D_{III(interstitial)} [I_{III}] \qquad Eq.\ (3.3)$$

By assuming that an interstitial Ga atom can move into a vacancy, leaving no defect, and applying the law of mass action, Eq (3.4) can be formed, where k_1 is a temperature dependent constant.

$$0\ (Ga_{Ga}) \Leftrightarrow I_{Ga} + V_{Ga} \quad \text{thus} \quad [I_{Ga}][V_{Ga}] = k_1 \qquad Eq.\ (3.4)$$

Similarly, assuming I_{Ga} can diffuse to the surface and react with excess As_4 supplied by an overpressure to form GaAs, and applying the law of mass action, Eq. (3.5) can be formed, where P_{As4} is the As_4 vapour pressure, and k_2 a temperature dependent constant.

$$0\ (GaAs) \Leftrightarrow \tfrac{1}{4}As_4\ (vapour) + I_{Ga} \quad \text{thus} \quad [I_{Ga}] = k_2 P_{As4}^{-1/4} \qquad Eq.\ (3.5)$$

Substituting Eq. (3.4) and Eq. (3.5) into Eq. (3.3) gives Eq. (3.6).

$$D_{III} = f'_1 D_{III(vacancy)} P_{As4}^{1/4} + f'_2 D_{III(interstitial)} P_{As4}^{-1/4} \qquad Eq.\ (3.6)$$

3.2.2.3 Crystal Stoichiometry:- Effect of As_4 Overpressure on Interdiffusion Rate

Crystal stoichiometry determines the concentration of native defects. Since the stoichiometry is sensitive to the As_4 overpressure during annealing,

characterising the intermixing as a function of As_4 overpressure and anneal temperature can shed some light on the interdiffusion mechanism [Deppe *et al* (1988)]. Annealing under As rich conditions favours the generation of the following point defects near the surface: As_{III}, I_{As}, and V_{III}. Annealing under As poor conditions favours the formation of III_{As}, I_{III}, and V_{As}. Since interdiffusion takes place via the column III atoms, the two defects of prime interest are V_{III} and I_{III}, hence the influence of the As_4 vapour pressure on the interdiffusion rate can be used to infer the disordering mechanism.

Early experiments on the effect of As_4 vapour pressure on the column III interdiffusion rate were conducted by Guido *et al* (1987). They performed sealed ampoule annealing on GaAs/AlGaAs QW material. Control of the As_4 pressure was obtained by adding controlled amounts of As to the ampoules before sealing. The capless samples were annealed under a fixed schedule of 825 °C for 25 h. Photoluminescence (PL) was used to measure the shift in peak wavelength of the radiative recombination, and this was used to infer the column III interdiffusion rate. The experimental results provided evidence for both the vacancy and interstitial disordering mechanisms, though the results were far from conclusive.

To further investigate the effect of stoichiometry on column III interdiffusion rate, similar experiments to those of Guido *et al* (1987) were performed by Olmsted and Houde-Walter (1993), on nominally undoped AlGaAs/GaAs superlattices in sealed ampoules. Excess Ga and As were used to control the deviation from an ideal crystal. Annealing temperatures ranged from 700 to 1050 °C. The extent of the column III interdiffusion was inferred from the PL shift in the peak signal. The As rich annealing conditions showed a much greater Al-Ga interdiffusion coefficient than the Ga rich conditions, giving strong evidence that the column III vacancy interdiffusion mechanism dominates over that of the column III interstitial. Cohen (1997) re-analysed the experimental data from Olmsted and Houde-Walter (1993), showing the dependence on interdiffusion rate with As_4 overpressure. Reducing the As_4

overpressure gives a clear reduction in the interdiffusion rate, with a qualitative fit of D_{III} proportional to $P_{As4}^{1/4}$, which from Eq. (3.6) provides very strong evidence that in nominally undoped AlGaAs/GaAs material column III interdiffusion proceeds via the column III vacancy mechanism. Additionally, on the plot of the column III diffusion coefficient against As_4 overpressure, Cohen (1997) incorporates experimental data from other groups. The data included suffers from significant measurement noise, even within experimental groups, demonstrating uncertainty in the results. Summarising these experiments, the results of Olmsted and Houde-Walter (1993) and Cohen (1997) provide strong evidence that column III interdiffusion is dominated by the column III vacancy disordering mechanism, however there is evidence that the interstitial disordering mechanism may also have an influence, albeit a smaller one.

3.2.2.4 Low Temperature Grown GaAs

The crystal stoichiometry of molecular beam epitaxy (MBE) grown GaAs is dependent on the growth temperature, allowing control of native point defects. Wafers grown at much lower temperatures than standard growth conditions have a large As excess, resulting in an increased concentration of Ga vacancies [Gebauer *et al* (1997)]. Gebauer *et al* (1997) investigated the concentration of V_{Ga} for crystals grown between 200 and 350 °C. Defect concentrations were measured by positron annihilation. Wafers grown at 350 °C showed $[V_{Ga}]$ to be below the sensitivity limit of roughly $10^{16}/cm^3$, whereas growth at the lowest temperature of 200 °C resulted in $[V_{Ga}]$ reaching a maximum of 1-2 x $10^{18}/cm^3$. Growth of low-temperature (LT) GaAs layers within a wafer can therefore be used to enhance the interdiffusion rate of the column III atoms. Tsang *et al* (1995) have shown how a single LT-GaAs cap layer on the top of an AlGaAs/GaAs superlattice can be used to enhance the compositional disordering. In their experiment the superlattice was grown at normal temperature (580 °C), and capped with 100 nm of LT-GaAs grown at 200 °C. A second superlattice with a normal temperature GaAs cap layer was also grown for comparison. Samples from each wafer were then furnace annealed between two semi-insulating GaAs wafers to avoid arsenic desorption.

Column III interdiffusion coefficients were then determined from photoluminescence (PL) spectra taken at 77 K. The activation energy for the LT-GaAs was 4.1 eV, which is smaller than that of normal temperature grown GaAs heterostructures (around 6 eV). The smaller activation energy for the LT-GaAs is a consequence of the enhanced interdiffusion due to the increased concentration of Ga vacancies. Growth of a LT-GaAs cap layer, followed by patterning and selective removal over the wafer, and finally annealing, allows the possibility of monolithically integrating regions of differing bandgap over the wafer.

3.2.3 Impurity Induced Layer Disordering (Electrically Active Impurities)

Following the unexpected discovery of IILD, as explained in section 3.2.1, the mechanisms, control and applications of the intermixing technology have been researched by various groups. Many electrically active impurities such as the donors Si, Ge, S, Sn, and Se, in addition to the acceptors Zn, Be, and Mg have proven capable of IILD in the GaAs/AlGaAs system [Deppe and Holonyak (1988)]. To explain IILD with electrically active impurities, Tan and Gösele (1987) proposed the *Fermi-level* effect, where the concentration of charged point defects depends on the position of the Fermi-level, and hence the concentration and type of dopant impurity. They comment that "Furthermore, it is the presence of the dopant that is important, and not its motion, i.e., its diffusion." Effectively, the electrically active impurities generate free carriers, which consequentially increase the point defect concentrations, enhancing heterostructure intermixing during annealing. Further research by Tan and Gösele (1988) provided more information on the Fermi-level effect, and this was incorporated by Deppe and Holonyak (1988) into a more complete understanding of the mechanism by including the influence of the As overpressure.

Although the IILD technique has proven capable of disordering heterostructures, the need for high concentrations of electrically active

impurities severely impacts on device characteristics and suitable applications. In particular, the need for impurity concentrations in the order of $10^{18}/cm^3$, leads to large free carrier absorption losses, typically greater than 43 dB/cm ($10\ cm^{-1}$) [Marsh (1993)]. Consequentially, the high free-carrier loss severely limits the lengths of any passive intermixed sections, and means that IILD using electrically active impurities is better suited to active devices (where the losses can be offset by gain), rather than passive devices. Secondly, the electrically active impurities change the material resistivity, which can be detrimental for devices requiring good electrical isolation. Even so, IILD has been successfully applied to various devices including non absorbing mirrors (NAMs) for high power lasers [Suzuki *et al* (1984)], and buried heterostructures for improved current confinement [Deppe *et al* (1985)].

3.2.4 Implantation Induced Disordering (Electrically Neutral Impurities)

Large free carrier losses and changes in the material resistivity associated with IILD using electrically active impurities make IILD far from ideal for many applications. One possible solution to this problem is to create damage, hence point defects in the material, and then subsequently diffuse them through the wafer, causing disordering. Although material damage can be created by irradiation using particles such as electrons, ions and photons, the majority of research has focussed on ion induced damage, and hence will be the focus of this section. For example, Gavrilovic *et al* (1985) showed how ion implantation induced damage is capable of disordering during annealing. In the experiment, AlAs/GaAs SLs grown by metal-organic chemical vapour deposition (MOCVD) were implanted with various ions, followed by annealing and cross-section inspection. The first test used implantation of Al^+ ($10^{15}/cm^2$, 390 keV), followed by annealing at 850 °C for 8.33 h. A masked region of the sample showed no signs of disordering, indicating that the SL is thermally stable when there is no implantation. However, the region exposed to the Al implantation was partially disordered, which they ascribed to the diffusion of implantation induced damage. To further verify this interpretation,

implantation using inert Kr^+ ($10^{15}/cm^2$, 390 keV) followed by annealing at 850 °C for 8.33 h was performed. Again the masked part was not disordered, but the implanted area of SL was completely disordered. The effect of implantation of an electrically active donor was then investigated using S^+ ($10^{14}/cm^2$, 390 keV) followed by annealing at 850 °C for 3 h. The implanted region was completely disordered, the masked region was not disordered. Since the fluence and annealing time for this sample were less than for the Al implanted sample, but the level of disordering greater, it is apparent that the electrically active S contributed to the disordering mechanism via the Fermi-level effect. Summarising the experiment, diffusion of implantation induced damage during annealing is capable of disordering SL structures. The Fermi-level effect also contributes to disordering when electrically active impurities are used.

Both fluorine and boron, which are electrically neutral at room temperature in the GaAs/AlGaAs system have been successfully used as implantation species for disordering of GaAs/AlGaAs heterostructures. O'Neill *et al* (1989) demonstrated large blue-shifts in GaAs/AlGaAs MQW material by implanting with either boron of fluorine ions, followed by subsequent annealing. Implantation doses ranged from 10^{14} to 3×10^{15} cm^{-2}, with energies between 100 and 300 keV. Annealing was performed in a conventional diffusion furnace at temperatures ranging from 750 to 890 °C for between ½ and 6 h. Large blue-shifts in the PL spectra of up to approximately 100 meV were measured, together with substantial shifts in the position of the absorption edge, demonstrating the effectiveness of the disordering. Further experiments by O'Neill *et al* (1990) demonstrated a propagation loss of 4.7 dB/cm in fluorine disordered GaAs/AlGaAs MQW waveguide structures. However, since scattering losses also contribute to the loss, this figure does not represent the ultimate lower limit. Even so, this loss figure is much lower than the free-carrier absorption loss of approximately 43 dB/cm associated with electrically active IILD, typically requiring dopant concentrations above $10^{18}cm^{-3}$ [Marsh (1993)].

Heterostructure disordering by implantation of native or electrically neutral species, followed by subsequent annealing is not only an interesting phenomenon in itself, but has been applied to a variety of material systems and device applications. For example, Hashimoto *et al* (2000) used N implantation induced disordering in GaInAs/GaInP to form passive non-absorbing mirror sections for high power 980 nm lasers. Similarly, in an attempt to reduce facet heating in 980 nm lasers, Piva *et al* (1998) applied As implantation induced disordering to the InGaAs/AlGaAs system to make passive extended cavities. Charbonneau *et al* (1998) applied P implantation induced disordering to InP based 1.5 μm lasers for shifting the bandgap energy, hence the lasing wavelength, thus forming monolithically integrated lasers of different wavelengths, suitable for WDM systems. Suppression of implantation induced disordering was achieved using a patterned SiO_2 masking layer, which protects the semiconductor surface from implanted species. Perhaps one of the most interesting implantation induced disordering techniques uses a focussed ion beam (FIB) for the implantation, offering excellent spatial resolution necessary for some device applications. Reithmaier and Forchel (1998) give an excellent description of the FIB implantation induced disordering technique, and its applications. Using Ga as the implantation impurity they demonstrated disordering of both InGaAs/GaAs and InGaAsP/InP QW structures. They applied the technology to devices including bandgap shifted ridge waveguides, lateral waveguiding and carrier confinement, and gain-coupled DFB lasers. Even so, implantation induced disordering is not ideal, and can suffer from traps associated with the implantation species, and residual damage [Marsh (1993)]. Furthermore, the technique requires expensive and complicated ion implantation apparatus.

3.2.5 Laser Induced Disordering

Laser induced disordering (LID) of III-V heterostructures can be achieved using laser irradiation to either melt the material, or create defects which can then be diffused by subsequent annealing. Epler *et al* (1986) demonstrated disordering of a GaAs/AlGaAs SL using a tightly focussed CW Ar^+ laser

(λ=488 nm), where the power density of the laser beam was sufficient to melt the material, subsequent recrystallisation of which resulted in nearly homogenous AlGaAs material, albeit with poor crystal quality. In this technique the energy of the incident photons was sufficiently high to be absorbed by all the layers in the wafer. A more advanced form of LID, known as photoabsorption-induced disordering (PAID), uses an incident wavelength of light which is only absorbed in the QW region, and which is below the bandedge of the cladding layers. McLean *et al* (1992) applied PAID to the InGaAsP/InP system, using CW irradiation from a Nd:YAG laser (λ=1064 nm). PL measurements at 77 K demonstrated a shift of 123 meV with respect to the as-grown wafer, clearly showing the potential for monolithic optoelectronic integration. PAID has been successfully applied to a number of applications including bandgap tuned lasers, electroabsorption modulators, low loss waveguides, and extended cavity lasers [McKee *et al* (1997)]. One limitation of the LID and PAID techniques is the poor spatial resolution, which is limited by the thermal conduction. An alternative form of PAID, known as pulsed PAID (P-PAID) uses high energy laser pulses to create damage, and hence point defects in the QW region, subsequent diffusion of which by annealing results in the disordering of the QW [McKee *et al* (1997)]. The P-PAID technique shows improved spatial resolution, better than 25 μm. One of the great strengths of the LID variants is the lack of impurities required, meaning that free-carrier losses and damage can be kept to a minimum. Another advantage is the ability to trim laser bandgap energies to precisely control the lasing wavelength. Furthermore, the technique has a direct write capability. Although having good potential for optoelectronic integration, the technique requires further improvement to be commercially attractive.

3.2.6 Impurity Free Vacancy Disordering

Impurity free vacancy disordering (IFVD) uses selective diffusion of native semiconductor atoms into dielectric cap layers to create vacancies at the semiconductor surface, diffusion of which at elevated temperatures results in heterostructure disordering. Deppe *et al* (1986) demonstrated the IFVD

process for GaAs/AlGaAs heterostructure disordering, and showed a blue-shift in the radiative recombination spectrum for a disordered laser with respect to an undisordered laser. Chemical vapour deposited (CVD) SiO_2 and Si_3N_4 layers were used to promote and suppress disordering respectively. Diffusion of Ga into the SiO_2 layer during annealing (at around 850 °C for a time of 6 h or more) creates column III vacancies at the dielectric-semiconductor interface, subsequent diffusion of which results in hetersotructure disordering under this cap. Evidence for Ga diffusion into SiO_2 cap layers on GaAs was given by Vaidyanathan *et al* (1977). The Si_3N_4 layer inhibits Ga in-diffusion, and thus prevents vacancy formation, consequently suppressing disordering under this cap. High temperature annealing of uncapped samples can lead to desorption and surface degradation. Selective patterning of the wafer with SiO_2 and Si_3N_4 layers, followed by annealing, allows monolithic integration of different bandgap energies. However, as explained by Marsh (1993), pure silicon nitride films are difficult to obtain, and typically suffer from significant SiO_2 incorporation, which can lead to inadequate suppression of disordering and poor reproducibility. Beauvais *et al* (1992) demonstrated suppression of GaAs/AlGaAs heterostructure disordering using a SrF_2 cap, though this is still far from ideal since the caps appear damaged after annealing, and can be very difficult to remove. Rao *et al* (1995) demonstrated another IFVD technique for III-V semiconductors, based on using phosphorous doped SiO_2 layers to control in-diffusion of atomic species.

Since electrically active impurities and ion implantation induced damage are avoided, IFVD has the potential for forming very low loss waveguides, and avoids problems associated with residual implantation damage, and significant changes to the material resistivity. Furthermore, the technique is planar, relatively simple, and is suitable for large scale commercial exploitation.

IFVD in its various forms has been utilized to fabricate a number of devices benefiting from bandgap modification, as explained in the remainder of this section. Gontijo *et al* (1994) used the SiO_2/SrF_2 approach to integrate a

disordered extended cavity section (passive) with an undisordered active section in the GaAs/AlGaAs system. Dry etching was used define the ridge waveguide. Losses as low as 3.6 dB/cm were inferred for the disordered region, clearly demonstrating the ability for low loss waveguide fabrication. Ooi *et al* (1997) used the SiO_2/SrF_2 variant of IFVD in the GaAs/AlGaAs system for various device applications. Propagation losses of singlemode as-grown and disordered ridge waveguides were compared, where the disordered waveguides were bandgap shifted by 28 nm (55 meV). From a plot of the propagation loss as a function of wavelength it was clearly apparent that the disordered waveguides were free from significant bandedge absorption at the as-grown lasing wavelength of the material (around 860 nm). It was also evident that the minimum shift required to be free of significant bandedge absorption was in the order of 20 nm, though a larger shift would be desirable to ensure minimal absorption. Furthermore, at wavelengths well above bandedge absorption, it was clear that the losses of both as-grown and disordered waveguides were the same at around 9 dB/cm, proving that additional losses are not incurred when IFVD is used for disordering. They also applied their IFVD technology to wavelength shifted lasers, and a four channel demultiplexing waveguide photodetector, both of which are future components for WDM systems. Suzuki *et al* (1990) demonstrated TE/TM mode selective channel waveguides in a GaAs/AlAs superlattice fabricated by SiO_2 cap disordering. Propagation losses of 4-5 dB/cm were measured for the disordered regions. Jiang *et al* (1998) used IFVD for lateral mode control and current confinement in a GaAs/AlGaAs MQW laser to improve the lateral mode stability. Hofstetter *et al* (1998) applied the SiO_2/SrF_2 IFVD technique to a number of device applications in the GaAs/AlGaAs system including: multi-wavelength Fabry-Perot laser arrays, wavelength shifted modulators, DBR lasers, interferometers, and a photonic integrated circuit consisting of a laser, passive waveguide and photodetector.

3.3 Intermixing Process and Experiments

3.3.1 History of QWI Research at Glasgow University

Research into intermixing at the Department of Electronics and Electrical Engineering, University of Glasgow, was initiated by John Marsh in around 1987. Initial research focussed on electrically neutral implantation induced disordering, using fluorine and boron as the implantation species to disorder GaAs/AlGaAs, GaInAs/AlGaInAs and GaInAs/GaInAsP. In the early 1990s a number of intermixing techniques were investigated including photoabsorption induced disordering (PAID), and dielectric cap annealing with either SiO_2/Si_3N_4 or SiO_2/SrF_2 cap layer combinations. Research into Pulsed PAID (P-PAID) began in around 1995. Following the findings by Rao *et al* (1995), the SiO_2/SiO_2:P dielectric cap annealing technique was investigated. Problems associated with the PECVD SiO_2 led the researchers to use sputtered SiO_2 as an alternative, which resulted in the surprise discovery of the sputtered SiO_2 intermixing process.

3.3.2 Sputtered SiO_2 Intermixing Process

McDougall *et al* (1998) describe the sputtered SiO_2 intermixing process. The process is based on sputtering a thin SiO_2 layer directly onto the semiconductor surface, followed by high temperature annealing to intermix the QWs under the sputtered SiO_2 cap. Sputtering of the SiO_2 film is performed in a Nordiko RF machine, using an Ar:O_2 gas mixture at a pressure of 5×10^{-3} mbar, with an RF power of 100 W, and DC self bias of 1 kV. Suppression of intermixing with respect to the sputtered SiO_2 area can be achieved using a PECVD SiO_2 cap. Therefore, patterning the surface with sputtered SiO_2 and PEVCD SiO_2, followed by subsequent annealing allows selective control of where intermixing occurs.

3.3.2.1 Initial Understanding of Process (Damage Mechanism)

The initial understanding of the mechanism was based upon the deposition process damaging the semiconductor surface, thus creating vacancies and interstitials near the surface, which diffuse through the structure during

annealing, resulting in intermixing of the wells and barriers. Investigation of the sputtered SiO_2 intermixing process was performed using a special InGaAsP MQW damage probe wafer structure, consisting of five QWs of different widths [McDougall *et al* (1998)]. Following sputter deposition of 200 nm of SiO_2, the PL intensity of the QWs nearest the surface degraded with respect to the deeper QWs. After high temperature annealing to intermix the QWs, the PL intensity of the shallow QWs recovered. As explained by McDougall *et al* (1998), "These observations are consistent with the sputtering process leading to an increase in the near-surface point defect density, which reduces the PL from the QWs closest to the surface. During the anneal however, point defects will tend to diffuse both towards the sample surface and deeper into the sample, leading to a reduced defect density in the QW region and the initiation of the intermixing process through the enhanced interdiffusion of well and barrier species." Generation of the point defects near the surface was ascribed to the energetic bombardment of the surface during deposition of the SiO_2. The deposition process was believed to break atomic bonds, thus creating vacancies and interstitials, which diffuse through the structure during annealing, consequently intermixing the wells and barriers.

3.3.2.2 Current Understanding of Mechanism (Cu Impurity)

Following the spin-off of Intense Photonics, the sputtered SiO_2 intermixing process became commercially important, which led to increased research into the mechanism. Although the process was initially believed to be impurity free, during this period of increased research it was discovered that the sputtered SiO_2 film contained a quantity of Cu impurity, which helps to promote intermixing. However, the impurity concentrations are believed to be much smaller than in IILD, and hence the free-carrier loss is not so high. Additionally, the IFVD mechanism is believed to be involved, where the sputtered SiO_2 film allows enhanced in-diffusion of atomic species to promote intermixing with respect to PECVD SiO_2. The discovery of intermixing using the sputtered SiO_2:Cu film was subsequently patented by Intense Photonics and the University of Glasgow (United Kingdom Patent Application 01 22 128.9).

The sputtered SiO_2 QWI technology has been applied to fabricate a number of devices including wavelength tuned lasers, extended cavity lasers and novel array lasers [McDougall *et al* (1998)]. The intermixing process is capable of very low losses, for example, recent results from Bubke *et al* (2002) demonstrated waveguide losses as low as 6 dB/cm for intermixed waveguides in the InGaAs/AlGaInAs system, demonstrating the effectiveness of the technique. Qiu *et al* (2000) demonstrated a monolithically integrated 2 × 2 crosspoint switch in the InGaAs/InGaAsP system using the sputtered SiO_2 intermixing technique, illustrating the potential for optoelectronic integration.

3.3.3 Experiments and Results

3.3.3.1 Process Development

Research focussed on the application of the QWI process rather than the investigation and development of the actual intermixing technology. For the intermixing process to be useful it is necessary to be able define which areas of a sample undergo intermixing, and in which areas intermixing is suppressed. As explained by McDougall *et al* (1998), a 200 nm thick layer of PECVD SiO_2 is insufficient to protect the semiconductor surface during sputter deposition of the intermixing SiO_2; during annealing undesirable intermixing takes place underneath this layer. However, a 1.8 μm thick layer of S1818 photoresist was proven to be very successful at protecting the semiconductor surface from the SiO_2 sputter deposition. Although there are alternative schemes for the spatial control of the intermixing process, the most common approach, and the one used in the early part of this research, is based upon a photolithographic lift-off process as illustrated in Figure 3.2, where the photoresist protects the semiconductor surface during the SiO_2 sputtering. Photolithography is used to define which areas of the sample are to be intermixed (no photoresist), and suppressed (photoresist). The sample is then sputtered with SiO_2, where the photoresist protects the semiconductor surface. Following sputtering, the sample is soaked in acetone, which dissolves the photoresist region, and hence lifts-off the sputtered SiO_2 on top of the photoresist. A layer of e-beam evaporated SiO_2 is then deposited over the whole sample. The sample is then

annealed in a rapid thermal annealer (RTA) to intermix the QWs underneath the sputtered SiO_2 layer; intermixing is suppressed underneath the evaporated SiO_2 layer. High temperature annealing of uncapped samples can lead to desorption and surface degradation, therefore it is essential to use a cap layer for suppression of intermixing and to maintain material quality. Following intermixing, all of the SiO_2 cap layer is then removed by HF acid wet etch. Although this process is capable of device production it has a number of limitations:

(1) The interface between the intermixed and suppressed regions can be rather poor, due to contamination from the photoresist lift-off edge profile.

(2) The e-beam evaporated SiO_2 layer can have poor adhesion.

(3) Chlorobenzene is required for the lift-off process, however this substance is hazardous and harmful to the reproductive system.

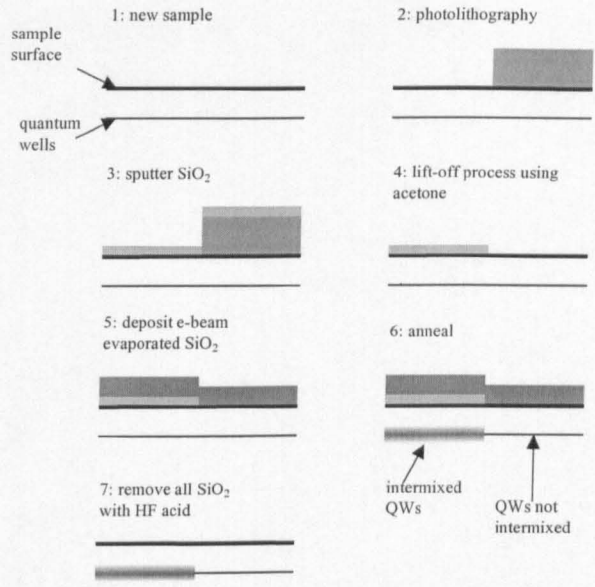

Figure 3.2: Lift-off process for spatial control of intermixing process. Intermixing takes place under the sputtered SiO_2 cap, whereas the evaporated SiO_2 cap suppresses intermixing. During sputtering of the SiO_2, the photoresist region protects the semiconductor surface, therefore helping to inhibit intermixing.

To alleviate the problems associated with the aforementioned lift-off process, an alternative scheme was developed based upon using a thick layer of PECVD

SiO_2 to protect the semiconductor surface, and therefore inhibit intermixing underneath this cap. Liu *et al* (2000) demonstrated multiple bandgap shifts in the InGaAs-AlInGaAs system, using different thicknesses of PECVD SiO_2 for protection from a single sputtered SiO_2 deposition. Therefore, choosing a suitably thick layer of PECVD SiO_2 allows the suppression of the intermixing process. Following the findings of Liu *et al* (2000), a 500 nm thick PECVD layer was implemented for suppression of intermixing in the GaAs-AlGaAs system; this layer was found to be sufficiently thick to protect the semiconductor and hence inhibit intermixing. The PECVD SiO_2 protection layer process is illustrated in Figure 3.3. The first step is to deposit a 500 nm layer of PECVD SiO_2. Photolithography and wet etch using HF acid are then used to remove the PECVD SiO_2 in regions to be intermixed. Acetone is then used to remove the photoresist. Sputtering of a thin layer of SiO_2 is then performed over the whole sample, which is subsequently annealed to intermix the QWs in the desired areas. The PECVD SiO_2 is sufficiently thick to inhibit intermixing underneath this cap. Removal of all the SiO_2 is then performed using HF acid.

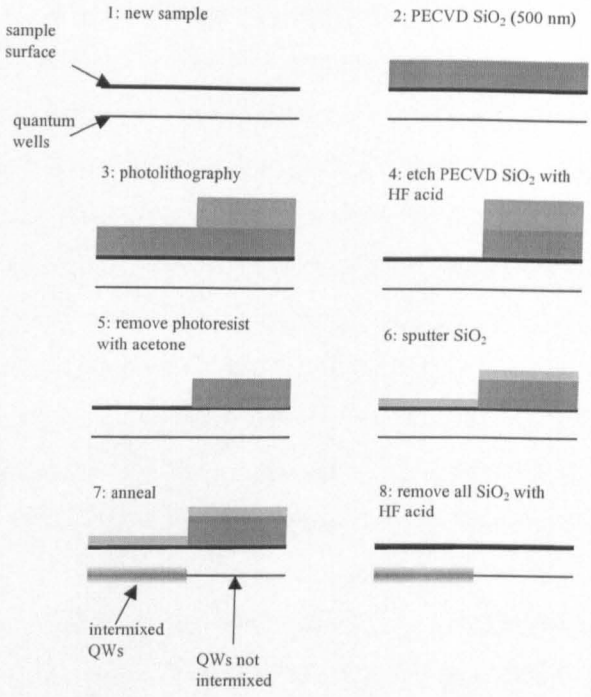

Figure 3.3: PECVD SiO_2 protection process for spatial control of the intermixing process. The 500 nm PECVD SiO_2 layer is sufficiently thick to protect the semiconductor surface from the sputtering process, and hence inhibits intermixing under this cap. Intermixing takes place underneath the sputtered SiO_2 cap.

3.3.3.2 Intermixing of GaAs/AlGaAs QW Laser Structure

During the initial period of this research, various thicknesses of sputtered SiO_2 were investigated, though it was found that the influence on intermixing did not vary greatly. Since 50 nm thick layers of sputtered SiO_2 were found to produce reliable bandgap shifts, it was decided to use this thickness for the majority of the research. The sputtering process itself was kept constant. Since intermixing is essentially a diffusion process, the two important control parameters are the anneal temperature and time. Samples were annealed in a Jipelec Jet First rapid thermal annealer (RTA). Operating the RTA at high temperature for more than a few minutes tends to shorten the lamp lifetime, and hence it was decided to fix the anneal time at 60 s, and vary the temperature to control the extent of intermixing. Samples were typically annealed p-side down on the RTA's Si susceptor, with a piece of Si wafer on top to limit desorption and prevent the sample from moving during annealing.

Annealing was performed under a nitrogen atmosphere. Typically, when performing intermixing, a number of small test samples were annealed at different temperatures for a fixed time of 60 s. The PL spectrum of each test sample was then measured, and the blueshift plotted as a function of anneal temperature. The PL measurement was taken by attaching the sample to an optical fibre using acetone soluble glue, and then immersing in liquid nitrogen to cool the sample to 77 K (this reduces phonon scattering, leading to an improved signal). Optical excitation of the sample was then performed using an Ar^+ laser, and the emitted spectrum was measured using a monochromator and Ge detector (cooled to 77 K). After the PL spectrum was taken, the sample could be removed from the fibre using acetone to dissolve the glue.

Figure 3.4 shows typical PL spectra of as-grown, suppressed and intermixed samples using the method just described. The material used was the standard GaAs/AlGaAs DQW laser structure, described previously in section 2.4. Annealing the suppressing and intermixing samples at 875 °C for 60 s gives a differential shift of around 40 nm (79 meV), which should be sufficient for producing low loss passive intermixed waveguides.

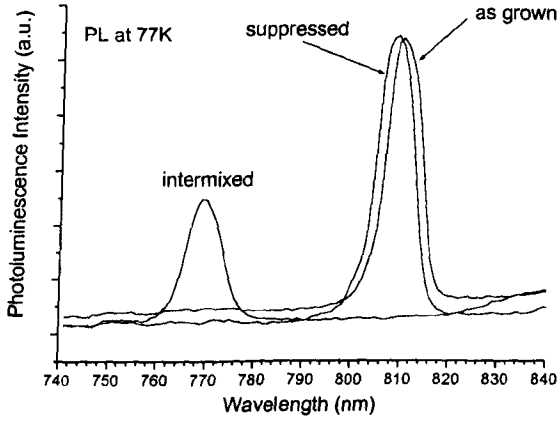

Figure 3.4: Photoluminescence spectra of as-grown, suppressed and intermixed GaAs/AlGaAs DQW laser structure samples. The as-grown sample was not annealed. The suppressed sample has a cap of 500 nm PECVD SiO_2 for protection, with 50 nm sputtered SiO_2 on top, and was annealed at 875 °C for 60 s. The intermixed sample has a cap of 50 nm sputtered SiO_2 and was also annealed at 875 °C for 60 s. Clearly a large differential shift of around 40 nm between the suppressed and intermixed samples was obtained, demonstrating the effectiveness of this intermixing process.

Figure 3.5 shows the PL peak blue-shift as function of anneal temperature for intermixing and suppressing test samples. Clearly the samples covered with just the 50 nm of sputtered SiO_2 start intermixing at a much lower temperature than the samples with the 500 nm thick PECVD SiO_2 protection layer, demonstrating the effectiveness of the PECVD SiO_2 layer in suppressing intermixing. Even so, at sufficiently high temperatures the suppressing samples start to intermix, probably due to the IFVD mechanism. The temperatures required to achieve intermixing are consistent with previous work at the department. The difference in temperature dependence of the intermixing and suppressing samples allows a suitable temperature to be chosen which gives the required blue-shift. Since the majority of research in this project is concerned with integrating low loss passive waveguides with active laser sections, it is desirable to obtain a large differential blue-shift without significantly intermixing the active (suppressed) section, therefore actual laser device samples were typically annealed in the region of 850 to 875 °C. During the fabrication process, test samples were annealed to determine the intermixing performance and the optimum anneal temperature.

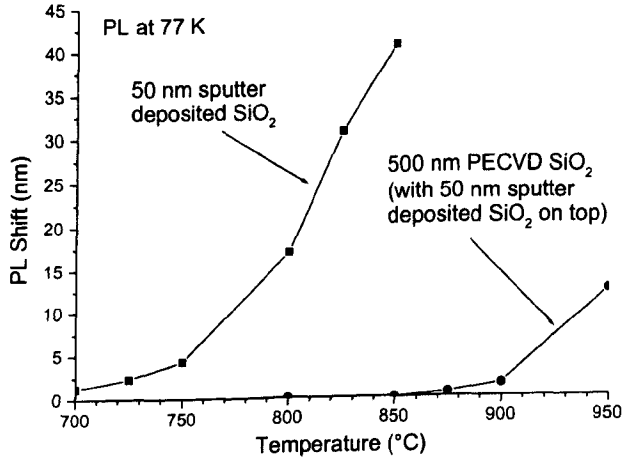

Figure 3.5: Photoluminescence (PL) blue-shift as a function of anneal temperature for intermixed and suppressed samples. The anneal time was fixed at 60 s for each sample. Since the sputtered SiO_2 covered samples start intermixing at a lower temperature than the PECVD SiO_2 covered samples, a reasonable differential shift between intermixed and suppressed areas can be achieved by appropriate choice of anneal temperature.

3.3.3.3 Alternative Intermixing Cap Processes

Following the discovery of the impurity in the sputtered SiO_2 intermixing process, Intense Photonics developed true impurity free SiO_2 caps for intermixing other III-V material systems, and hence these were studied for the GaAs/AlGaAs system. Figure 3.6 shows the PL peak blue-shift of a GaAs/AlGaAs DQW laser structure with various SiO_2 cap layers as a function of anneal temperature. The "Glasgow" and "IP" cap layers use essentially the same process, and display very similar intermixing characteristics, demonstrating the transferability of this technology to other sputtering machines. Both the "Diode" and "Magnetron" sputtered SiO_2 cap layers were developed for intermixing other III-V material systems, however for the GaAs/AlGaAs system they require much higher temperatures than the "Glasgow" and "IP" processes, and as they have similar intermixing characteristics to the PECVD SiO_2 cap, they are unsuitable for promoting intermixing (though they could be used for suppressing intermixing).

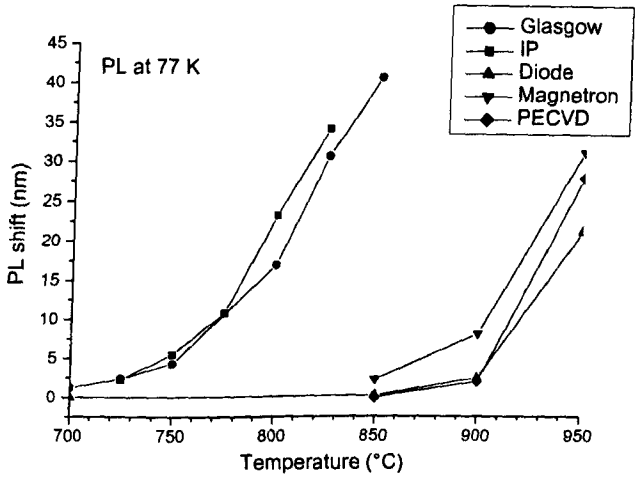

Figure 3.6: Intermixing performance of various types of SiO_2 cap layers on standard GaAs/AlGaAs DQW laser structure. All samples were annealed for 60 s. The "Glasgow" cap was 50 nm of SiO_2 sputtered at Glasgow University. The "IP" cap was sputtered by Intense Photonics under similar conditions to the "Glasgow" cap. Both the "Diode" and "Magnetron" caps were true impurity free caps sputtered by Intense Photonics and were developed for intermixing other III-V material systems. The "PECVD" cap was a 200 nm thick layer of PECVD SiO_2 deposited at Glasgow University.

3.4 Conclusions

This chapter has introduced the topic of QWI, and given an overview of the alternative III-V intermixing techniques and their relative merits. The sputtered SiO_2 intermixing technique developed at Glasgow University has been described, including its attributes and applications. Since this research was concerned with the application of this intermixing process, a selective process suitable for device manufacture is described. Intermixing results from GaAs/AlGaAs DQW laser structures demonstrate the technology for producing large differential blue-shifts suitable for integrating passive intermixed sections with active as-grown sections.

3.5 References

Beauvais J., Marsh J. H., Kean A. H., Bryce A.C., and Button C., "SUPPRESSION OF BANDGAP SHIFTS IN GaAs/AlGaAs QUANTUM WELLS USING STRONTIUM FLUORIDE CAPS," *Electronics Letters*, vol. 28, no. 17, pp. 1670-1672, August 1992.

Bubke K., Sorel M., Robert R., Bryce A. C., Arnold J. M., and Marsh J. H., "Loss measurements in intermixed InGaAs/AlGaInAs Multiple-Quantum-Well Ridge Waveguides," IEEE WFOPC conference, Glasgow, 2002.

Charbonneau S., Koteles E. S., Poole P. J., He J. J., Aers G. C., Hayson J., Buchanan M., Feng Y., Delage A., Yang F., Davies M., Goldberg R. D., Piva P. G., and Mitchell I. V., "Photonic Integrated Circuits Fabricated Using Ion Implantation," *IEEE J. Sel. Top. Quant. Electron.*, pp. 772-793, vol. 4, no. 4, July/Aug. 1998.

Cohen R. M., "Point defects and diffusion in thin films of GaAs," *Material. Science and Engineering*, R20, pp. 167-280, 1997.

Cusumano P., Marsh J. H., Rose M. J., and Roberts J. S., "High-Quality Extended Cavity Ridge Lasers Fabricated by Impurity-Free Vacancy Diffusion

with a novel Masking Technique," *IEEE Photon. Technol. Lett.*, vol. 9, no. 3, pp. 282-284, March 1997.

Deppe D. G., Hsieh K. C., Holonyak N., Burnham R. D., and Thornton R. L., "Low-threshold disorder defined buried-heterostructure $Al_xGa_{1-x}As$-GaAs quantum well lasers," *J. Appl. Phys.*, vol. 58, no. 12, Dec. 1985.

Deppe D. G., Guido L. J., Holonyak N., Hsieh K. C., Burnham R. D., Thornton R. L., and Paoli T. L., "Stripe-geometry quantum well heterostructure $Al_xGa_{1-x}As$-GaAs lasers defined by defect diffusion," Appl. Phys. Lett., vol. 49, no. 9, pp. 510-512, Sept. 1986.

Deppe D. G., and Holonyak N., "Atom diffusion and impurity-induced layer disordering in quantum well III-V semiconducotr heterostructures," *J. Appl. Phys.*, vol. 64, no. 12, R93-R113, Dec. 1988.

Epler J. E., Burnham R. D., Thornton R. L., Paoli T. L., and Bashaw M. C., "Laser induced disordering of GaAs-AlGaAs superlattice and incorporation of Si impurity," *Appl. Phys. Lett.*, vol. 49, no. 21, pp. 1447-1449, Nov. 1986.

Gavrilovic P., Deppe D. G., Meehan N., Holonyak N., Coleman J. J., "Implantation disordering of $Al_xGa_{1-x}As$ superlattices," *Appl. Phys. Lett.*, vol. 47, no. 2, July 1985.

Gebauer J., Krause-Rehberg R., Eichler S., Luysberg M., Sohn H., and Weber E. R., "Ga cacancies in low-temperature-grown GaAs identified by slow positrons," *Appl. Phys. Lett.*, Vol. 71, no. 5, August 1997.

Gontijo I., Krauss T., De La Rue R. M., Roberts J. S., and Marsh J. H., "Very low loss extended cavity GaAs/AlGaAs lasers made by impurity-free vacancy diffusion," *Electronics Letters*, vol. 30, no. 2, pp. 145-146, Jan. 1994.

Guido L. J., Holonyak N., Hsieh K. C., Kaliski R. W., Plano W. E., Burnham R. D., Thornton R. L., Epler J. E., and Paoli T. L., "Effects of dielectric encapsulation and As overpressure on Al-Ga interdiffusion in $Al_xGa_{1-x}As$-GaAs quantum-well heterostructures," *J. Appl. Phys.*, vol. 61, no. 4, pp. 1372-1379, Feb. 1987.

Hashimoto J., Ikoma N., Murata M., and Katsuyama T., "A Highly Reliable GaInAs-GaInP 0.98-μm Window Laser," *IEEE J. Quantum Electron.*, vol. 36, no. 8, pp 971-977, Aug. 2000.

Hofstetter D., Maisenhölder B., and Zappe H. P., "Quantum-Well Intermixing for Fabrication of Lasers and Photonic Integrated Circuits," *IEEE J. Sel. Top. Quant. Electron.*, pp. 794-802, vol. 4, no. 4, July/Aug. 1998.

Holonyak N., "Impurity-Induced Layer Disordering of Quantum-Well Heterostructures: Discovery and Prospects," *IEEE J. Sel. Top. Quantum. Electron.*, vol. 4, no. 4, pp. 584-594, July/Aug. 1998.

Jiang A. Q., Sun C. Z., Hao Z. B., Luo Y., and Wang J. H., "Novel Laser Structures Based on MQW Interdiffusion Using Rapid Thermal Annealing," *IEEE J. Sel. Top. Quant. Electron.*, pp. 736-740, vol. 4, no. 4, July/Aug. 1998.

Kim M. S., Caneau C., Colas E., and Bhat R., "Selective area growth of InGaAsP by OMVPE," *J. of Crystal Growth*, vol. 123, pp. 69-74, 1992.

Kudo K., Sasaki T., and Yamaguchi M., "Migration-controlled narrow-stripe selective MOVPE for high quality InGaAsP/InP MQWs," *J. of Crystal Growth*, vol. 170, pp. 634-638, 1997.

Liu X. F., Qiu B. C., Ke M. L., Bryce A. C, and Marsh J, H., "Control of Multiple Bandgap Shifts in InGaAs-AlInGaAs Multiple-Quantum-Well

Material Using Different Thickness of PEVCD SiO_2 Protection Layers," *IEEE Photon. Technol. Lett.*, vol. 12, no. 9, pp. 1141-1143, Sep 2000.

Marsh J. H., "Quantum well intermixing," *Semicond. Sci. Technol.*, pp. 1136-1155, 1993.

McDougall S. D., Kowalski O. P., Hamilton C. J., Camacho F., Qiu B., Ke M., De La Rue R. M., Bryce A. C., and Marsh J. H., "Monolithic Integration via a Universal Damage Enhanced Quantum-Well Intermixing Technique," *IEEE J. Sel. Top. Quantum. Electron.*, vol. 4, no. 4, pp. 636-646, July/Aug. 1998.

McKee A., McLean C. J., Lullo G., Bryce A. C., De La Rue R. M., Marsh J. H., and Button C. C., "Monolithic Integration in InGaAs-InGaAsP Multiple-Quantum-Well Structures Using Laser Intermixing," *IEEE J. of Quant. Electron.*, vol. 33, no. 1, pp. 45-55, Jan. 1997.

McLean C. J., Marsh J. H., De La Rue R. M., Bryce A. C., Garrett B., and Glew R. W., "LAYER SELECTIVE DISORDERING BY PHOTOABSORPTION-INDUCED THERMAL DIFFUSION IN InGaAs/InP BASED MULTIQUANTUM WELL STRUCTURES," *Electronics Letters*, vol. 28, no. 12, pp. 1117-1119, June 1992.

Olmsted B. L., and Houde-Walter S. N., "Al-Ga interdiffusion through group III-vacancy second nearest-neighbor hopping," *Appl. Phys. Lett.*, vol. 63, no. 4, pp. 530-532, July 1993.

O'Neill M., Bryce A. C., Marsh J. H., De La Rue R. M., Roberts J. S., and Jeynes C., "Multiple quantum well optical waveguides with large absorption edge blue shift produced by boron and fluorine impurity-induced disordering," Appl. Phys. Lett., vol. 55, no. 12, pp. 1373-1375, Oct. 1989.

O'Neill M., Marsh J. H., De La Rue R. M., Roberts J. S., Button C., and Gwilliam R., "REDUCTION OF THE PROPAGATION LOSSES IN IMPURITY DISORDERED QUANTUM WELL WAVEGUIDES," *Electronics Letters*, vol. 26, no. 19, pp. 1613-1615, Sept. 1990.

Ooi B. S., McIlvaney K., Street M. W., Helmy A. S., Ayling S. G., Bryce A. C., Marsh J. H., and Roberts J. S., "Selective Quantum-Well Intermixing in GaAs-AlGaAs Structures Using Impurity-Free Vacancy Disordering," *IEEE J. Quantum Electron.*, vol. 33, no. 10, pp. 1784-1793, Oct. 1997.

Piva P. G., Goldberg R. D., Mitchell I. V., Fafard S., Dion M., Buchanan M., and Charbonneau S., "Reduced 980 nm laser facet heating by band gap shifted extended cavities", J. Vac. Sci. Technol. B.,pp. 1790-1793, Jul./Aug., 1998.

Qiu B. C., Qian Y. H., Kowalski O. P., Bryce A. C., Aitchison J. S., De La Rue R. M., Marsh J. H., Owen M., White I. H., Penty R. V., Franzen A., Hunter D. K., and Andronovic I., "Fabrication of 2 × 2Crosspoint Switches Using a Sputtered SiO_2 Intermixing Technique," *IEEE Transactions on Photon. Technol. Lett.*, vol. 12, pp. 287-289, March 2000.

Rao E. V. K., Hamoudi A., Krauz Ph., Juhel M., and Thibierge H., "New encapsulant source for III-V quantum well disordering," *Appl. Phys. Lett.*, vol. 66, no. 4, pp. 472-474, Jan. 1995.

Reithmaier J. P., and Forchel A., "Focussed Ion-Beam Implantation Induced Thermal Quantum-Well Intermixing for Monolithic Optoelectronic Device Integration," *IEEE J. Selected Topics in Quantum Electronics*, vol. 4, no. 4, pp. 595-605, July/August 1998.

Sasaki T., Yamaguchi M., and Kitamura M., "Monolithically integrated multi-wavelength MQW-DBR laser diodes fabricated by selective metalorganic vapor phase epitaxy," *J. of Crystal Growth*, vol. 145, pp. 846-851, 1994.

Suzuki Y., Horikoshi Y., Kobayashi M., and Okamoto H., "FABRICATION OF GaAlAs 'WINDOW-STRIPE' MULTI-QUANTUM-WELL HETEROSTRUCTURE LASERS UTILISING Zn DIFFUSION-INDUCED ALLOYING," *Electronics Letters*, vol. 20, no. 9, pp. 383-384, April 1984.

Suzuki Y., Hidetoshi I., and Mikami O., "TE/TM mode selective channel waveguides in GaAs/AlAs superlattice fabricated by SiO_2 cap disordering," *Appl. Phys. Lett.*, vol. 56, no. 1, pp. 19-20, Jan. 1990.

Tan T. Y., and Gösele U., "Destruction mechanism of III-V compound quantum well structures due to impurity diffusion," *J. Appl. Phys.*, vol. 61, no. 5, pp. 1841-1845, March 1987.

Tan T. Y., and Gösele U., "Mechanism of doping-enhanced superlattice disordering and of gallium self-diffusion in GaAs," *J. Appl. Phys.*, vol. 52, no. 11, pp. 1240-1242, April 1988.

Tsang J. S., Lee C. P., Fan J. C., Tsai K. L., and Chen H. R., "Compositional disordering of AlGaAs/GaAs superlattices by using the low-temperature grown GaAs," *J. Vac. Sci. Technol. B*, "vol. 13, no. 4, pp. 1536-1538, Jul./Aug. 1995.

Vaidyanathan K. V., Helix M. J., Wolford D. J., Streetman B. G., Blattner R. J., and Evans C. A., "Study of Encapsulants for Annealing ," *J. Electrochem. Soc.*, vol. 124, no. 11, pp. 1781-1784, Nov. 1977.

Venkatesan T., Schwarz S. A., Hwang D. M., Bhat R., Koza M., Yoon H. W., Mei P., Arakawa Y., and Yariv A., "Dose-dependent mixing of AlAs-GaAs superlattices by Si ion implantation," *Appl. Phys. Lett.*, vo. 49, no. 12, pp. 701-703, Sept. 1986.

Chapter 4

Non Absorbing Mirror Ridge Laser

4.1 Introduction

As explained in chapter 1, mirror degradation can severely limit the performance of high power semiconductor lasers. In order to increase the mirror durability, various experiments have been conducted to investigate and suppress the degradation mechanisms. This chapter describes the development of a non absorbing mirror (NAM) ridge laser, where the NAM helps to suppress mirror degradation. Figure 4.1 shows a schematic of the device investigated. The NAM was fabricated using the sputtered SiO_2 QWI technique described previously in chapter 3, and was combined with the ridge laser technology described in chapter 2, to produce a high power ridge laser. This intermixing process has demonstrated very low passive losses, and since the process is free from large concentrations of impurities, it should offer excellent performance for NAM lasers. Suppressing mirror degradation requires an understanding of the mechanisms involved, therefore section 4.2 summarises the main findings of mirror degradation experiments. Section 4.3 describes technologies which can be applied to suppress mirror degradation, focussing on the NAM technique. The design and fabrication of a ridge laser with NAMs is explained in section 4.4. Section 4.5 shows and compares the

results from standard and NAM lasers fabricated in the same batch. Conclusions are drawn in section 4.6.

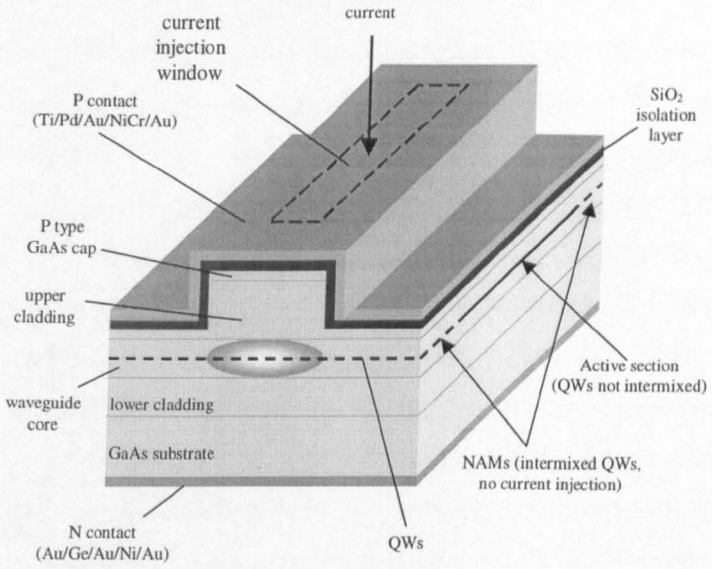

Figure 4.1: Schematic of the ridge waveguide NAM laser. The intermixed NAM regions are designed to suppress mirror degradation and COD.

4.2 Mirror Degradation

Experiments have been conducted by various research groups to determine the mechanisms involved in mirror degradation. These experiments have provided vital information for increasing the power capability and reliability of high power semiconductor lasers. Facet heating due to non-radiative recombination of surface states was found to be the driving force behind mirror degradation [Tang *et al* (1991a, 1991b), Puchert *et al* (1996), Welch (2000)]. Catastrophic optical damage (COD) is caused when the heating is sufficient to melt the end of the facet, and is particularly problematic in lasers containing AlGaAs [Welch (2000)]. Operating the laser below the COD level results in gradual degradation of the facet, and eventual COD. The degradation process has two stages; initially the facet degrades slowly, causing an increased facet temperature, until a critical facet temperature is achieved, once at this critical

temperature the facet begins degrading rapidly and thermal runaway occurs, terminating with COD.

Tang *et al* (1991a) used time evolution Raman microprobe measurements of facet temperatures to investigate facet degradation mechanisms; Table 4.1 summarises the findings. The Raman microprobe technique uses an Ar^+ laser probe to determine the facet temperature. Nominally identical uncoated AlGaAs single QW 5μm wide ridge lasers with typical threshold currents of around 20 - 25 mA were operated under constant drive currents in air. Both the output power and facet temperature were monitored as a function of time. Facet temperature was shown to gradually increase linearly with time, the rate of increase being a function of the operating current and hence the output power; the greater the operating current the greater the rate of increase (see Table 4.1). Accompanying this gradual increase in temperature was a gradual decrease in output power of a few milli-Watts before COD occurs. During this initial slow degradation regime, the facet temperature increased gradually until a critical temperature (typically ~120 – 140 °C above room temperature) was achieved whereupon a rapid rise in facet temperature commenced, accompanied by rapid reduction in output power and COD. As shown in Table 4.1, the time to this second regime is determined by the operating current, the harder the laser is driven the faster it degrades. The operating atmosphere was shown to play a crucial rule in the degradation process. Lasers operating under helium or nitrogen were shown to have much slower rates of degradation than lasers operated in air, indicating the detrimental effects of water vapour and oxidising agents on the facet. For example, as shown in Table 4.1, comparison of nominally identical lasers operated at 46 mW output power in air and either helium or nitrogen shows the detrimental effect of the air atmosphere; lasers operated in a helium or nitrogen atmosphere did not suffer COD for at least 2 h whereas the lasers operated in air typically suffered COD in 10 – 20 min. The effect of facet oxidation on AlGaAs/GaAs lasers was also investigated by Tu *et al* (1996). They showed improved COD levels when the facets were cleaved in

a vacuum before deposition of facet coatings. Reducing facet oxidation therefore helps inhibit the degradation process.

Laser operating current (mA)	Initial output power (mW)	Operating atmosphere	Time to COD (minutes)	Rate of initial (linear) temperature increase (°C/min)
115	46	Air	10 – 20	~10
106	40	Air	60 – 90	~0.7
95	34	Air	>180 (no COD observed)	~0.15
~115	46	Helium or nitrogen	>120	—

Table: 4.1: Summary of findings from Tang *et al* (1991a). The results show how the rate of facet degradation is influenced by the laser injection current (hence output power) and operating atmosphere. The relative humidity of the air atmosphere was measured to be 45 %.

Tang *et al* (1991a) also investigated the rapid non-linear increase in facet temperature, and subsequent COD using the Ar^+ probe laser as an external heat source. The facet temperature of an unbiased laser was monitored as a function of Ar^+ probe power. Facet temperature was found to increase linearly with probe power to greater temperatures than the critical temperature for the rapid non-linear degradation regime. This proves that the rapid non-linear temperature rise is not solely due to facet temperature. A laser biased to give an initial power of 35 mW was then probed using increasing Ar^+ beam powers to act as an external heat source. The effect of this external heat source was to increase the degradation rate of the device, when compared to a nominally identical device biased at the same level. The critical temperature at which the rapid temperature rise occurs was similar for devices with and without significant heating from the Ar^+ probe, and was around 120 – 140 °C above room temperature. The reason for the rapid non-linear temperature rise appears to be due to increased absorption at the facet as the temperature increases, leading to more absorption and eventual thermal run-away. During the initial

slow degradation regime, the facet temperature increases slowly, resulting in a band-gap shrinkage, and increased absorption. Eventually a critical temperature is reached, and a positive feedback cycle is established; the increasing temperature leads to increased absorption at the facet, increasing the number of photo-generated carriers in the facet region, which may recombine non-radiatively at surface states, subsequently heating the facet. Eventually the cycle ends with COD.

Experiments on facet heating by Puchert *et al* (1996) highlighted the crucial role of photo-absorption induced carrier heating. Micro Raman temperature experiments were conducted on AlGaAs laser arrays operating at around 810 nm. Below threshold, the facet temperature of individual emitters in the array was found to increase linearly with drive current, consistent with the findings of Tang et al (1991b). This confirms the role of the injected current supplying carriers for non-radiative surface recombination, hence facet heating. Above threshold the facet temperatures were found to increase linearly with the output power. Furthermore, the near-field pattern of the array showed excellent correlation to the individual temperatures of the emitters. These results indicate the role of photo-absorbed carriers in the facet region recombining non-radiatively, increasing the facet temperature.

Epperlein (1993) demonstrated an alternative technique for investigating facet heating. The technique, based on spatially resolved measurement of changes in the facet reflectivity, has an advantage over micro Raman spectroscopy in that it has a much faster response time, and hence is better suited when investigating in real-time the rapid increase in facet temperature at COD. Measurements on uncoated GaAs/AlGaAs lasers (single GaAs QW) below threshold showed a linear increase in the facet reflectance change, and hence temperature, as a function of drive current. Above threshold the facet temperature increased sharply in a linear fashion. These results are entirely consistent with facet heating due to non-radiative surface recombination, with carriers supplied by both the injected current, and photo-absorption at the facet.

Using this thermo-reflectance technique, the rapid increase in facet temperature at COD was investigated. The laser was operated with increasing drive current, and both the facet temperature and output power were measured. A large temperature spike was observed at the moment of COD, consistent with the positive feedback thermal runaway degradation mechanism explained previously.

Facet degradation mechanisms and associated feedback loops were discussed by Fukuda *et al* (1994); Figure 4.2 shows a simplified version of the degradation mechanisms outlined. Electron-hole pairs are created by photon absorption at the facet. Nonradiative surface recombination of these pairs results in facet heating, and eventual COD. The heating also causes a band-gap energy reduction at the facet, which increases the facet absorption, and results in current concentration. Photogenerated electron-hole pairs lead to facet oxidation via increased bond breaking. Furthermore, heating at the facet thermally drives the oxidation process, which in turn increases the defect concentration. Clearly the mechanisms lead to positive feedback, and eventually thermal run-away, terminating with COD.

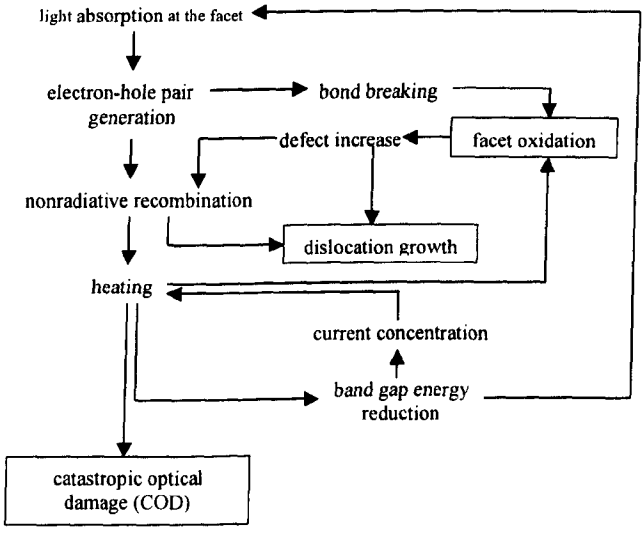

Figure 4.2: Facet degradation mechanisms and feedback loops. Clearly the loops give positive feedback which can result in thermal runaway and eventual COD.

Facet degradation behaviour and its impact on device reliability/lifetime can be understood by considering the stress-strength model [Fukuda *et al* (1994), Hashimoto *et al* (1997)]. The model, shown in Figure 4.3, illustrates how the facet degradation affects the COD level and device lifetime. The stress is the level at which the laser is driven (i.e. output power). Facet strength is an indication of the power capability before COD. The instantaneous COD level is the facet strength when the laser is immediately driven to the point of facet destruction, i.e. no device ageing takes place. Tiny differences between nominally identical devices lead to a distribution of strengths. During laser operation the strength gradually decreases, eventually reaching the stress level, at which point the stress overcomes the strength, and COD takes place. Under high output power operation the strength degrades rapidly and, as the stress is high, COD takes place quickly, resulting in a short lifetime. Degradation under a low power regime is much slower and, as the stress level is low, the lifetime is much longer. Instantaneous COD power levels are very useful as they are rapidly obtained and allow lifetime estimation.

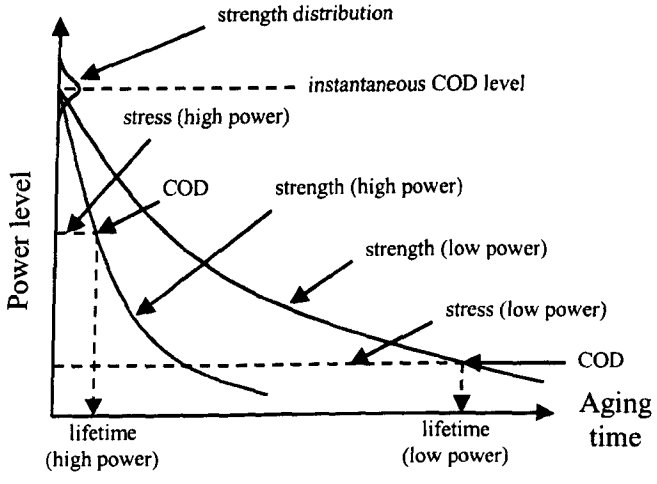

Figure 4.3: Stress-strength model of facet degradation and lifetime under high and low output power regimes.

Laser design and packaging influences the facet heating and hence plays a crucial role in the degradation process. Epperlein (1993) explains how each QW in the laser acts as a possible heat source, therefore the greater the number

of QWs the greater the facet heating. Furthermore, the type of bonding used determines the heat dissipation capability.

4.3 Degradation Reduction Technologies

Facet degradation can be suppressed by limiting the mechanisms shown in Figure 4.2. Since the two principal causes of degradation are light absorption at the facet and nonradiative recombination via surface states, the two most common approaches to facet protection involve either reducing the absorption coefficient in the facet region, or treating the facet surface in such a manner as to reduce the influence of nonradiative recombination centres [Hashimoto (2000)].

4.3.1 Non Absorbing Mirrors

Light absorption at the facet was found to be one of the driving mechanisms of facet degradation (see Figure 4.2), hence one approach to reducing degradation is to reduce the absorption coefficient at the facet. NAM lasers (also known as window lasers) were developed using this concept to increase the power capability and reliability of high power lasers. Although conceptually simple, developing a high performance technique is far from trivial, and has been actively pursued by various groups as the demand for high power devices increases. Figures 4.4 to 4.6 illustrate the concept of the NAM. A standard laser, where the whole of the cavity length is pumped, is shown in Figure 4.4. The high carrier density in the facet region leads to significant heating and degradation.

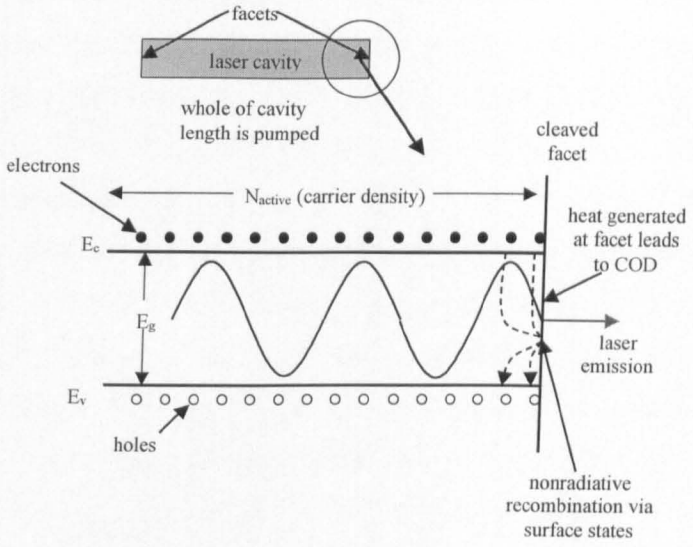

Figure 4.4: Simplistic band-gap diagram of facet region for standard laser (all of cavity length is pumped). Nonradiative recombination of electron-hole pairs via surface states leads to facet heating and eventual COD. Since the whole length of the cavity is injected with current, the carrier density near the facet is high, and consequently a large number electron-hole pairs recombine nonradiatively, severely heating the facet.

Since facet heating is due to the carrier density in the facet region, the first step to suppress heating is to reduce the facet region carrier density. This can easily be achieved by ensuring that current is not injected near the facet. Non-injection regions can be created easily by suitable patterning of a dielectric layer before contact deposition. Figure 4.5 shows how the non-injection region leads to a lower carrier density in the facet region, and reduced heating. However, photogenerated electron-hole pairs, and current diffusion into the facet region from the active region both contribute to the carrier density in the facet region, and hence the facet will still heat up, albeit less than if the whole of the cavity length was injected. Simplicity is one of the main advantages of this approach to reducing facet degradation. Horie *et al* (2000) used a patterned SiN_x dielectric layer to suppress current injection near the facets in 980-nm buried heterostructure InGaAs/AlGaAs lasers. Current injection was defined by a 125 nm thick SiN_x layer, and the length of the non-injection region was chosen to be 35 μm. Comparison of lasers with and without the current injection window was performed under CW testing at various

temperatures. The current injection window lasers showed thermal roll-over characteristics for all the temperatures tested (25 to 150 °C), however, the lasers without the current injection window suffered from COD when the temperature was 90 °C or more (at temperatures lower than this the devices showed thermal roll-over). This increased resilience to facet degradation using the current injection window can be attributed to a lower carrier density in the facet region. The HR/LR coated lasers were capable of around 500 mW output power at 25 °C (from the LR coated end). An alternative approach to reducing the carrier density in the facet region is to use a longer laser cavity (the longer cavity has a lower carrier density at threshold), however this is far from ideal and generally leads to an increase in threshold current, a reduction in external quantum efficiency, and fewer devices per wafer.

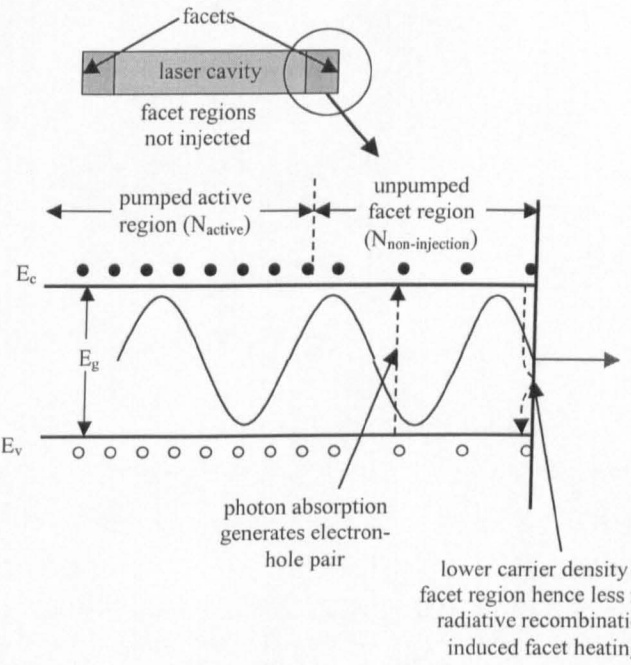

Figure 4.5: Laser cavity with non-injection facet regions. Since no current is injected near the facet, the carrier density in the facet region is lower than the standard laser, hence heating due to non-radiative recombination is reduced.

As explained earlier in section 4.2, the main contribution to facet heating above threshold is from nonradiative surface recombination of electron-hole pairs generated by photon absorption in the facet region. Reducing the absorption

coefficient in this region is therefore highly important when suppressing facet degradation. This can be achieved by increasing the band-gap energy in the facet region such that the incident photons have insufficient energy to undergo absorption. Figure 4.6 shows a simplistic diagram of how a NAM works. Although the concept of the NAM may be quite simple, the difficulty is to develop a suitable process to create this band-gap shift without introducing detrimental effects. Referring to the stress-strength model of Figure 4.3, the aim of the NAM is to increase the strength and reduce the rate of degradation.

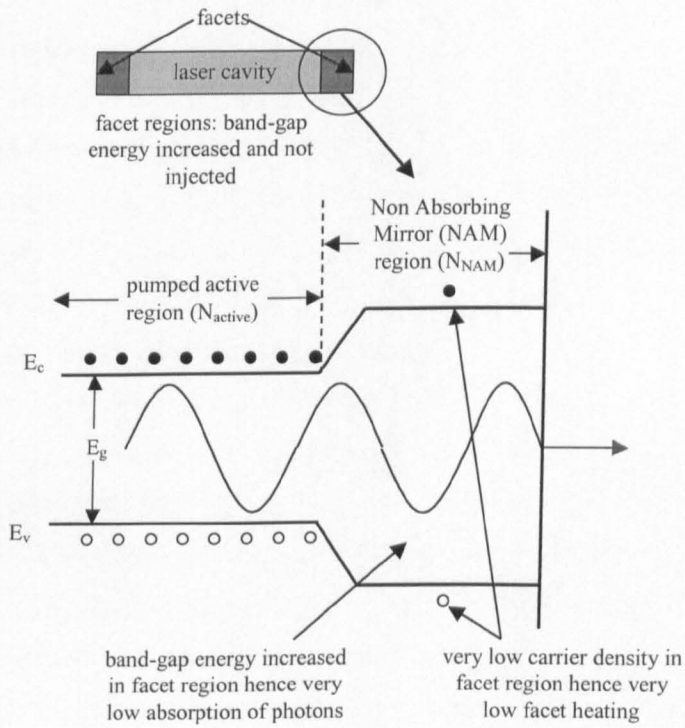

Figure 4.6: Non absorbing mirror (NAM) facet region. The band-gap energy in the facet region is increased to make this region transparent, hence there are very few photo-generated electron-hole pairs.

Quantum well intermixing (QWI) is by far the most common technique for creating NAMs. The technological attributes of QWI make it ideal for NAM fabrication; in particular, the ability to modify the band-gap of the facet region without the problems associated with etch/regrowth (interface defects etc) is advantageous. Since impurity induced disordering (IID) using Si or Zn as the

impurity is the most common approach for QWI, it is not surprising that the first reported NAM [Suzuki *et al* (1984)] and more recently reported NAMs use this technique. Suzuki *et al* (1984) used Zn IID to form the NAM regions on their GaAs/AlGaAs MQW lasers. Without the NAM regions, the lasers suffered COD at 40 mW/facet, however, the lasers with the NAMs suffered COD at the increased level of 120 mW/facet. This increase in the COD level by a factor of three clearly demonstrated a successful NAM, therefore providing motivation for other research groups to develop NAM technology.

Lee *et al* (1998) used Si implantation IID to create NAM regions on 0.98 μm GaInAsP-GaInP-GaAs ridge waveguide laser diodes. Post implantation annealing at 900 °C for 10 minutes was used to diffuse the active impurity through the QW region and consequently intermix the QWs with their barriers. Photoluminescence measurements of intermixed and as-grown samples showed a differential blue shift of around 50 nm, sufficient for forming the necessary transparent window. Three types of laser were fabricated: 1) standard ridge laser, 2) ridge laser with 30 μm NAM regions at each end, 3) ridge laser with 30 μm non-injection regions at each end (not intermixed, and no current injection). All the lasers had a total cavity length of 800 μm, and a width of 3.5 μm. No facet coatings were used. Lasers were tested under CW conditions. Average characteristics from the three different types of laser are shown in Table 4.2. Although the non-injection region laser had a higher threshold current, and lower slope efficiency than the standard laser, the mean COD level was 1.45 times greater, which can be attributed to the lower carrier concentration in the facet region. NAM lasers suffered from higher threshold currents and lower slope efficiencies, however the peak output power was limited by roll-over, not COD, therefore demonstrating improved facet durability. The increase in threshold current, and reduction in slope efficiency is consistent with additional losses in the NAM regions, one reason being increased free carrier absorption due to the electrically active impurity used for the intermixing. Even so, the peak capability of the NAM lasers is 1.64 times that of the standard laser, and would be even greater if the roll-over problem

could be reduced. Since it appears that the NAM lasers were limited by device heating, it could have been interesting to compare the three types of devices under pulsed testing conditions capable of facet destruction; NAM lasers would not be limited by thermal roll-over and hence could be driven to higher output power levels and to reach COD, hence it would be possible to compare relative COD levels.

	Threshold current (mA)	Slope efficiency per facet (W/A)	COD level per facet (mW)
Standard laser	22.6	0.41	142
Non-injection region laser	25.3	0.39	206
NAM laser	31.2	0.32	233 (roll over, not COD)

Table 4.2: Average characteristics of standard, non-injection region, and NAM lasers (from Lee *et al* (1998)).

Hiramoto *et al* (1999) also used Si ion implantation QWI for the fabrication of single-mode InGaAs-InGaAsP 980 nm NAM lasers. The cavity length and NAM regions were 900 μm and 30 μm respectively. High power ageing tests of lasers with and without the NAM regions were performed at a constant output power of 200 mW at 50 °C, and the drive current required to achieve this output power was monitored as a function of time (from 200 to 1000 h). To maintain an output power of 200 mW, the increase in the required drive current of the standard laser was over five times greater than the increase in the required drive current of the NAM lasers, thus demonstrating the lower degradation rate of the NAM lasers.

Kawazu *et al* (2001) demonstrated successful NAMs on single-mode 780 nm AlGaAs-GaAs lasers. Intermixing was performed by Si ion implantation followed by annealing at 800 °C. The LR/HR coated lasers had a total length of 800 μm, and stripe width of 2.5 μm. Under CW testing conditions, lasers without NAMs suffered COD at 180 mW, whereas the NAM lasers showed no COD even at 300 mW.

Shima *et al* (1997) incorporated NAM structures into their 680 nm visible GaInP based laser diodes. The lasers were developed for optical disk storage. Diffusion of Zn was used to intermix the QWs. Etch and re-growth were used for the lateral refractive index step and current aperture. Although direct comparison of standard lasers (no NAMs) to the NAM lasers was not performed, the NAM lasers showed, for the first time, reliable CW operation in excess of 5000 h under the conditions of 40 - 70 °C and 50 - 100 mW.

As explained in the earlier chapter on QWI, electrically active impurities such as Si and Zn can lead to increased free carrier absorption losses, and a possible increase in leakage current, both of which are undesirable for high performance NAMs. To alleviate the problems associated with electrically active impurities, Hashimoto *et al* (2000) used electrically neutral N for fabricating NAM regions on GaInAs-GaInP 0.98 μm lasers. Intermixing was performed by selective N implantation and subsequent rapid thermal annealing, giving a differential blue-shift of around 45 nm. The LR/HR coated 4 μm wide lasers with NAM regions were capable of over 220 mW CW power from the LR coated end, and were limited by thermal saturation, not COD. Lasers with the NAM window region showed vastly superior reliability and lifetime compared to standard lasers without the NAM regions. Under conditions of 50 °C and a constant output power of 150 mW, the mean time to failure (MTTF) of the standard lasers was 230 h (they failed by COD), whereas under similar test conditions, the NAM lasers operated stably and showed no signs of COD for durations up to 14 000 h, with a median lifetime of 280 000 h predicted for the NAM lasers.

Temperature measurements were performed by Piva *et al* (1998) on lasers with NAM regions to show the reduced facet heating. Ridge waveguide 980 nm InGaAs/GaAs/AlGaAs lasers were used for the experiments. Intermixing was performed by As ion implantation and subsequent annealing at 850 °C for 60 s, giving a differential blue shift of around 19 nm. NAM regions of length 0 to 200 μm were integrated on to each end of a 400 μm long active section, giving

total device lengths between 400 and 800 μm. Lasers were operated at 30 mW. A reflectance modulation technique was used to determine the temperature at the peak of the optical mode (centre of the waveguide), and this was normalised by the output power to give a heating coefficient in °C/mW. Lasers without the NAM regions had heating coefficients of slightly above 1 °C/mW, whereas lasers with the NAM regions had coefficients of 0.3 °C/mW (100 μm NAMs), and 0.15 °C/mW (200 μm NAMs). Although part of the reduction in facet heating was due to the distancing of the mirror from the heat generating active section, clearly the reduction in heating coefficients demonstrates the effectiveness of the NAMs in suppressing heating from photogenerated electron-hole pairs recombining nonradiatively via surface states.

What is very interesting and revealing to note is that Hiramoto *et al* (1999), Hashimoto *et al* (2000), Kawazu *et al* (2001), and Shima et al (1997) used etch/re-growth for the lateral index step and current aperture, but QWI to fabricate the NAM regions. This provides very strong evidence that the etch/re-growth process is not well suited to NAM fabrication; if the re-growth process was capable of producing high quality NAMs, then the groups would most likely have used this technology for NAM fabrication, and thus have avoided the additional QWI process. Furthermore, Ko *et al* (1999) comment that etch/re-grown NAM regions suffer from interface defects caused by oxidation of the etched surface. This drove them to develop a novel melt-back growth technique for NAM fabrication on buried heterostructure lasers (fabricated by etch/re-growth) which avoids the oxidation problem, but requires additional processing. This approach allowed them to increase the COD level of their uncoated 780 nm AlGaAs/GaAs lasers from 65 mW to 185 mW (tested under pulsed conditions to avoid thermal roll-over), albeit with an increase in threshold current and reduction in differential quantum efficiency.

Selective area growth can be used as an alternative to QWI for producing NAM lasers, though this requires specialized wafer growth. Lammert *et al*

(1995) demonstrated InGaAs-GaAs-AlGaAs buried heterostructure NAM lasers fabricated using selective area growth. Devices were tested under pulsed conditions to avoid thermal roll-over. The NAM laser showed a COD level of 326 mW/facet, compared to 228 mW/facet for the laser without the NAM, thus demonstrating an increase in COD level of over 40 %.

4.3.2 Facet Coating and Treatment

Since facet degradation is determined by the optical intensity in the facet region, back reflected light from the mirror also contributes to the degradation process [Ueno (1998)]. Deposition of facet coatings can be used to modify the facet reflectivity. Using such a coating to reduce the reflectivity can therefore reduce the degradation contribution from back reflected light, and consequently increase the power capability before the onset of COD. However, reducing the reflectivity increases the threshold current, and hence there exists a trade-off between the threshold current and COD level. A high reflectivity coating would typically be applied to the other facet to maximise the output power from one facet.

Surface states in AlGaAs are not an intrinsic property of the material, but may be caused by oxidation [Tu *et al* (1996), Horie *et al* (1999)]. Avoiding oxidation of the facet is therefore beneficial for suppressing facet degradation and COD, thus improving the device lifetime and reliability. A process for in-vacuum cleaving and coating of laser facets was developed by IBM (Zurich), which is now part of Bookham Technology. This process was subsequently patented (reference EP0457998), and is believed to have been licensed to other manufacturers including Corning-Lasertron and Agilent. This process is the main competitor to the NAM technology for producing reliable, high power laser facets. After cleaving, facet coatings are deposited without exposing the devices to the atmosphere; the cleaving and coating is performed in a single high vacuum machine, hence the facets are only exposed to the atmosphere once the coatings have been deposited. Since the AR/HR facet coatings normally contain oxygen (for example Al_2O_3 or SiO_2), a thin Si layer is

deposited on the facet before deposition of the AR/HR coating; the Si layer passivates the facet, and thus prevents the AR/HR coating oxidising the facet, which would cause the formation of surface states.

Further research on in-vacuum cleaving and coating of laser facets was described by Tu *et al* (1996), and they demonstrated improved COD levels. The approach was applied to single-mode 860 nm AlGaAs/GaAs ridge waveguide lasers. Uncleaved laser samples were mounted in a special mechanical fixture, which allows in-vacuum cleaving of laser bars. This fixture was then mounted in a high vacuum chamber and evacuated to a low pressure. The multi-chamber vacuum system was fitted with a Knudsen cell for Si deposition, and an electron-beam system for evaporation of Al_2O_3. Laser bars were cleaved in the vacuum chamber under a Si flux, thus reducing the exposure of the facets to residual gases in the vacuum system. Evaporation of Al_2O_3 was then performed whilst still in the vacuum system to give a low reflectivity facet coating. The purpose of the thin Si layer was to separate the Al_2O_3 coating from the facet, thus preventing the possibility of the Al_2O_3 layer oxidizing the facet and causing formation of surface states. Standard Si/SiO_2 layers were evaporated onto the other facet of the laser to form a high reflectivity mirror. Since the peak optical power is emitted by the low reflectivity mirror, it is unnecessary to use the in-vacuum cleaving and deposition on the high reflectivity facet (the HR mirror emits much lower power than the LR mirror). Standard lasers (cleaved in air then LR/HR coated) were compared to the novel in-vacuum cleaved LR/HR coated lasers under CW conditions. Standard lasers suffered COD at around 220 mW (from the LR coated end), whereas the in-vacuum cleaved lasers did not display COD up to output powers of 270 mW. This shows the improvement gained by cleaving and coating the facets in-vacuum. In addition to suppressing facet oxidation and hence surface state formation, the process also reduces contamination, which may contribute to facet degradation.

An alternative approach to in-vacuum cleaving and coating of the lasers is to cleave the facets in air, then treat the facets to suppress the extrinsic surface states caused by oxidation. Horie *et al* (1999) describe such a process using ion irradiation of the facets to reduce non-radiative surface recombination. They applied the technology to buried-stripe type InGaAs/GaAs/AlGaAs 980 nm lasers. The facet treatment process is summarised as follows. Firstly, the laser bars are cleaved in air using standard cleaving. Laser bars are then mounted in a vacuum chamber, which is used for both facet treatment (ion irradiation) and deposition of Si and AR/HR coatings. Facets were then exposed to a flux of Ar^+ ions whose average energy was kept below 35 eV to avoid facet damage; the purpose of the ion irradiation was to eliminate the Ga-O and As-O bonds which were caused by oxidation and act as possible non-radiative recombination surface sites. A thin Si interface layer was then deposited to separate the facets from oxides in the LR/HR mirror stacks (the interface layer prevents facet oxidation). AlO_x/Si dielectric layers were then deposited to form LR/HR mirrors. Standard lasers, without the ion irradiation and Si interface layer, were also fabricated for comparison. The ion irradiated lasers were capable of around 500 mW CW from the 2 μm wide LR coated facet (lasers were limited by thermal roll-over). Reliability comparisons of the conventional and ion irradiated lasers were performed under CW conditions. Conventional lasers operated at 150 and 200 mW showed rapid degradation and failure; the 150 mW lasers survived less than 250 h operation. Ion irradiated lasers operated at 150, 200, and 250 mW showed no signs of failure even for operation over 3000 h. This vast improvement in laser durability can be attributed to suppressed facet degradation as a result of the facet ion irradiation and Si deposition process. Surface analysis using X-ray photoelectron spectroscopy (XPS) was used to investigate the ion irradiation process on air exposed GaAs samples. The spectrum of an untreated GaAs surface showed peaks corresponding to Ga-O and As-O bonding. Another GaAs sample was coated with a 2 nm AlO_x electron beam evaporated layer; the XPS spectrum shows a peak corresponding to the Ga-O bond, but no peak corresponding to the As-O bond. Finally a GaAs sample was processed using

the ion irradiation technique, followed by deposition of 2 nm Si, then 2 nm AlO_x; the spectral peaks corresponding to Ga-O and As-O were not present, providing strong evidence for the elimination of GaO_x and AsO_x. In conclusion, this novel ion irradiation process appears capable of eliminating extrinsic surface states caused by oxidation, without the ion irradiation damaging the facet. Since LR/HR facet coatings would typically be used on high power lasers, the process is technologically attractive as the ion irradiation and depositions could be performed sequentially in a single machine.

4.4 Design and Fabrication of Ridge Laser with Non Absorbing Mirrors

The sputtered SiO_2 intermixing process described in chapter 3 has demonstrated very low passive losses and, since the process is free from large concentrations of impurities, it should offer excellent performance for NAM lasers. Therefore, the aim of the experiments performed was to integrate NAMs with the ridge laser technology described in chapter 2, and compare the relative performance of ridge lasers with and without NAMs. Refer to Figure 4.1 to see a schematic of the ridge laser with NAM sections at each end of the cavity. Since Al-containing lasers are particularly prone to COD [Hiramoto *et al* (1999), Lammmert *et al* (1995)], the GaAs/AlGaAs system provides an excellent way of assessing the validity of this NAM process. Also, since this QWI process is "universal" in that it can be applied to other III-V material systems [McDougall *et al* (1998)], the NAM technology can be transferred to further material systems suffering from facet degradation and COD.

One of the key advantages of this QWI process over other monolithic integration techniques is the simplicity with which intermixed passive sections can be integrated with active sections (not intermixed). Applying this QWI process to the ridge laser technology is therefore relatively straightforward. The first step was to etch alignment markers into the sample; this was performed using photolithography and $SiCl_4$ RIE, the photoresist was then removed using acetone. Although these alignment markers are not essential to

the process, and play no part in the actual device performance, they make processing much easier; without the markers it is difficult to tell where the sample has been intermixed, and therefore alignment of subsequent photolithographic steps becomes extremely difficult. The sample was then intermixed using the process described in section 3.3.3; a 50 nm thick layer of sputtered SiO_2 was used to promote intermixing, and a 500 nm thick layer of PECVD SiO_2 to suppress intermixing. Ridge lasers were then fabricated on the sample using the fabrication process described in section 2.6. To achieve single-mode operation, the ridge width was around 2.5 μm, with an appropriate etch depth required to cut-off higher order lateral modes (see chapter 2 for more details). The epitaxial material used is described in section 2.4. The NAM regions of the ridge lasers were aligned to intermixed regions of the sample, the active sections of the ridge lasers were not intermixed. The dielectric current injection window ensures that no current is injected into the intermixed NAM regions; this combined with the low loss passive NAM section should ensure that the carrier density in the facet region has been reduced and consequentially the mirror degradation suppressed. To ensure that the ridge lasers are capable of sufficient power to destroy the facets, the total device length for standard and NAM lasers was chosen to be 1000 μm. Facet coatings were not used since this would confuse the issue of the NAM performance.

Figure 4.7 shows the PL spectra from the processed sample. Successful intermixing is demonstrated by the 40 nm differential blue-shift between the intermixed and suppressed peaks. This energy blue-shift should be sufficient to give the low absorption needed for a high performance NAM.

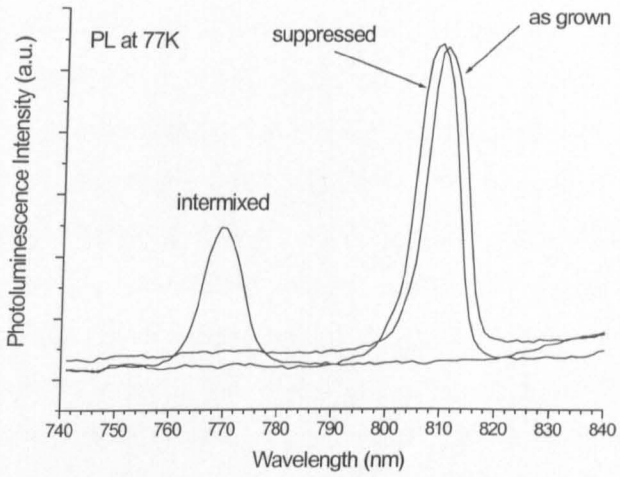

Figure 4.7: Photoluminescence spectra showing differential blue-shift of around 40 nm achieved by intermixing. The intermixed and suppressed samples were annealed at 875 °C for 60 s, the as-grown sample was not annealed.

Figure 4.8 shows an SEM image of a completed standard ridge laser (no NAMs). Clearly the fabrication process has worked well.

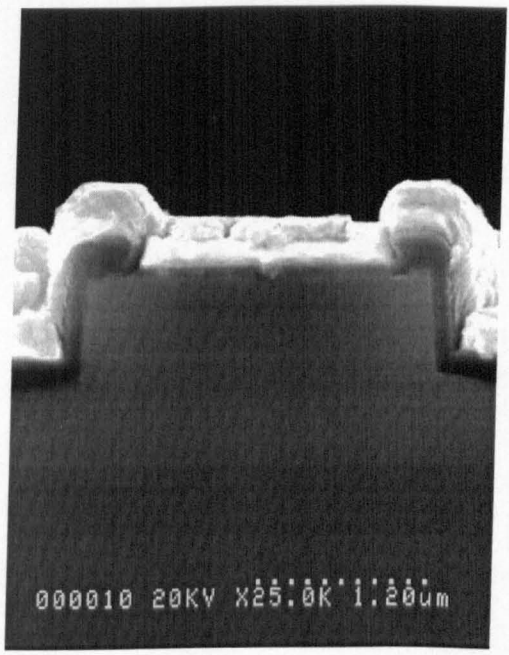

Figure 4.8: SEM of standard ridge laser. The ridge is well defined, and etched to the correct depth. Both the isolation and contact layers can easily be identified.

4.5 Results and Discussion

Figure 4.9 shows the L-I-V characteristic of the standard ridge lasers under pulsed (400 ns pulse/1kHz repetition) and CW test conditions. Threshold currents and differential quantum efficiencies are reasonable for such uncoated lasers, indicating successful device fabrication. The results are from two different devices fabricated within the same batch; the slight difference in threshold currents is most likely due to microscopic differences between individual devices. To avoid possible facet contamination problems, devices were not bonded/heat-sunk, and were thus tested in a simple device clip. Under pulsed testing, the device showed catastrophic failure, however under CW testing, thermal limitations meant that a COD power level could not be established. Since the CW and pulsed measurements were taken on completely different test set-ups, the close match between the measurements instils confidence in the results. The lateral beam profile of the laser is shown in Figure 4.10; single mode operation is apparent.

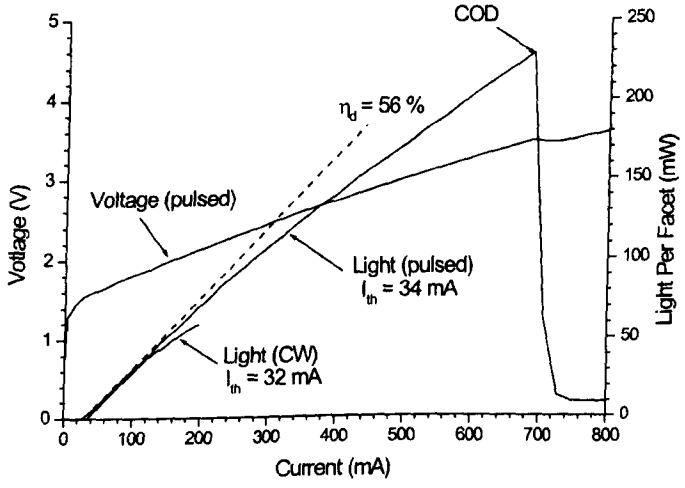

Figure 4.9: L-I-V characteristic of standard ridge laser without NAMs. Catastrophic failure occurs at around 230 mW per facet (pulsed). The CW measurement was taken from a nominally identical device, mounted in a clip (not bonded); device heating limited the output power.

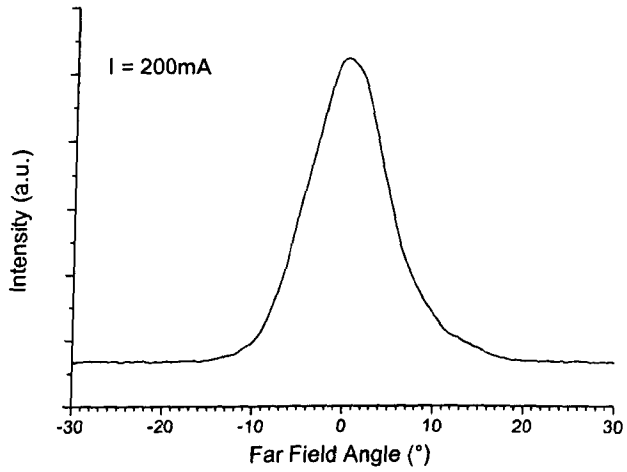

Figure 4.10: lateral far-field beam profile of ridge laser showing single mode operation.

Since the output power of the lasers was limited by heating under CW test conditions, it was not possible to evaluate COD power levels. Pulsed testing is not restricted by such limitations, and thus provides a useful technique for analysing relative facet performance. Ko *et al* (1999), Hashimoto *et al* (2000) and Lammert *et al* (1995) used pulsed testing to induce COD on their lasers, which were thermally limited under CW conditions. Although the COD levels for pulsed and CW conditions are unlikely to be identical, the pulsed conditions give a very useful idea of the facet capability, and moreover an excellent way of comparing the relative COD performance of standard and NAM lasers. Devices were tested using 400 ns pulses at a repetition rate of 1 kHz; these are the standard conditions used on the pulsed test set-up in the department. Since these conditions were capable of inducing COD on the standard ridge laser, they appear to be a valid tool for COD assessment.

Figure 4.11 shows a comparison of a standard laser and a laser with 60 μm long NAM sections at each end of the cavity. Differential quantum efficiencies for both devices were approximately the same, but the NAM laser had a slightly higher threshold current due to the additional NAM sections; therefore

the inclusion of the NAM sections does not significantly degrade the laser performance. A striking increase in the COD level by a factor of 2.6 is evident. This impressive increase in the COD level can be directly attributed to the inclusion of the NAM sections.

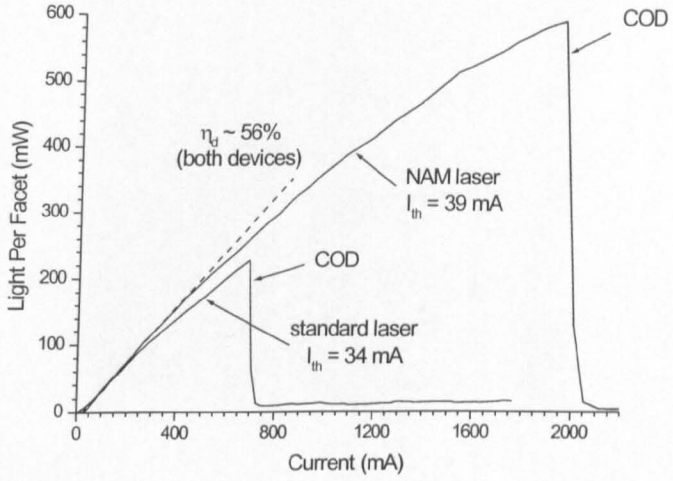

Figure 4.11: Pulsed L-I characteristics of standard and NAM ridge lasers. NAMs of length 60 μm were used at both ends of the NAM laser. Clearly the NAM laser can be driven to a much higher output than the standard laser, demonstrating the effectiveness of the NAM in suppressing COD.

Investigation of the catastrophic failure mechanism was performed by inspecting the facets of lasers destroyed under testing. Figure 4.12 shows a SEM image of a NAM laser which underwent catastrophic failure. The waveguide core region can be identified below the ridge. An anomalous region corresponding to the facet damage can be seen in the centre of the waveguide as consequence of the peak modal intensity.

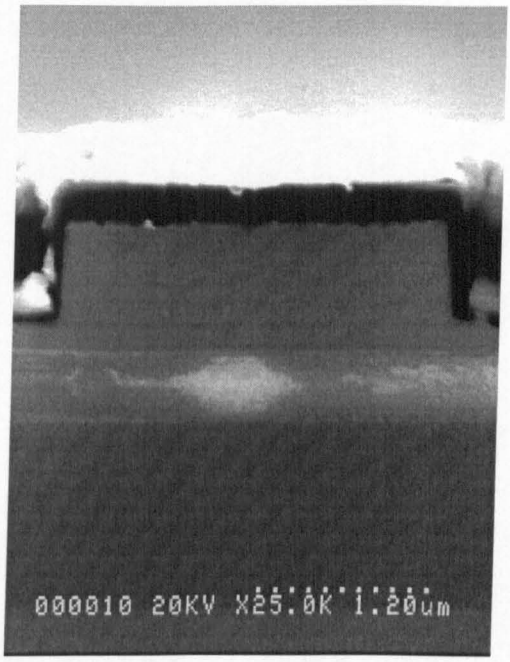

Figure 4.12: SEM of NAM laser facet after catastrophic failure, showing damage caused by COD.

Further investigation of the failure mechanism was performed by cleaving off both ends of a laser which had undergone catastrophic failure, thus forming a shorter laser from the internal region of the original laser. Figure 4.13 shows the L-I characters of a 400 μm long laser which was cleaved from a 1000 μm long destroyed laser. As a general rule of thumb, it becomes difficult cleaving off regions much shorter than twice the thickness of the sample, and as the lasers were around 150 μm thick, regions 300 μm long were cleaved off both ends of the original laser. Since the L-I characteristic showed lasing at a low threshold current, it appears that the damage in the 1000 μm laser had been confined to the facet regions, providing strong evidence that COD is the failure mechanism.

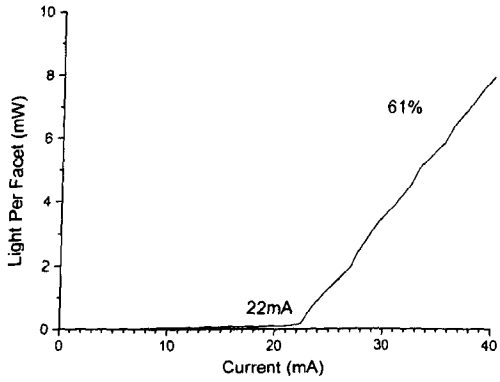

Figure 4.13: L-I characteristic of 400 μm long ridge laser cleaved from a laser which suffered catastrophic failure (300 μm was cleaved off each end of the 1000 μm long laser). Since the device operates with a low threshold current it confirms that the failure mechanism is COD.

4.6 Conclusions

This chapter successfully demonstrated a NAM laser technology capable of significantly improving the power capability of high power lasers prone to mirror degradation and COD. Under pulsed test conditions designed to induce COD, the NAM laser demonstrated a greater COD level than the standard laser by a factor of 2.6. This clearly demonstrates the advantage gained by using the NAM section in suppressing the facet region carrier density, which in turn leads to facet degradation via non-radiative surface recombination. Furthermore, it demonstrates the viability of this QWI process in creating high performance NAMs, without detrimental side effects. This QWI process is particularly attractive for producing NAMs, since the technique gives low optical loss and has a very low impurity concentration. The process is also relatively simple, providing a commercially attractive way to create high performance NAM lasers. Confirmation of the COD failure mechanism was achieved by facet inspection, and removal of the damaged facets. Facet coatings were not used in this experiment; inclusion of good quality LR/HR coatings in the process should lead to even higher COD levels. Transferring this technology to other material systems prone to facet degradation should yield significant improvements. It would be interesting to perform life-time

testing on a large batch of devices to investigate the long term degradation and reliability, however this research is of a more industrial nature and requires additional equipment and a large number of devices to test.

4.7 References

Botez, "Design considerations and analytical approximations for high contiuous-wave power, broad-waveguide diode laser," *Appl. Phys. Lett.*, vol. 74, no. 21, pp. 3102-3140, May 1999.

Epperlein P. W., "Micro-Temperature Measurements on Semiconductor Laser Mirrors by Reflectance Modulation: A Newly Developed Technique for Laser Characterization," *Jap. J. Appl. Phys.*, vol. 32, pp. 5514-5522, Dec. 1993.

Fukuda M., Okayasu M., Temmyo J., Nakano, J., "Degradation Behaviour of 0.98μm Strained Quantum Well InGaAs/AlGaAs Lasers Under High-Power Operation," *IEEE J. Quantum Electron.*, vol. 30, no. 2, pp 471-476, February 1994.

Garbuzov D. Z., Antonishkis N. J., Zhigulin S. N., Il'inskaya N. D., Kochergin A. V., Lifshitz D. A., Rafailov E. U., and Fuksman M. V., "High-power buried InGAAsP/GaAs (λ=0.8 μm) laser diodes," Appl. Phys. Lett., 62 (10), pp. 1062-1064, March 1993

Hashimoto J., Yoshida I., Murata M., Katsuyama T., "Aging Time Dependence of Catastrophic Optical Damage (COD) Failure of a 0.98-μm GaInAs-GaInP Strained Quantum-Well Laser," *IEEE J. Quantum Electron.*, vol. 33, no. 1, pp 66-69, Jan. 1997.

Hashimoto J., Ikoma N., Murata M., and Katsuyama T., "A Highly Reliable GaInAs-GaInP 0.98-μm Window Laser," *IEEE J. Quantum Electron.*, vol. 36, no. 8, pp 971-977, Aug. 2000.

Hiramoto K., Sagawa M., Kikawa T., and Tsuji S., "High-Power and Highly Reliable Operation of Al-Free InGAs-InGaAsP 0.98-μm Lasers with a Window Structure Fabricated by Si Ion Implanation," *IEEE J. Sel. Top. Quantum. Electron.*, vol. 5 no. 3 pp. 817-821, May/June, 1999.

Horie H., Ohta H., and Fujimori T., "Reliability Improvement of 980-nm Laser Diodes with a New Facet Passivation Process," *IEEE J. Sel. Top. Quantum. Electron.*, vol. 5 no. 3 pp. 832-838, May/June, 1999.

Horie H., Yamamoto Y., Arai N., and Ohta H., "Thermal Rollover Characteristics Up to 150 °C of Buried-Stripe Type 980-nm Laser Diodes with a Current Injection Window Delineated by a SiN_x Layer," *IEEE Photonics Technology Letters*, vol. 12, no. 1, pp. 13-15, Jan. 2000.

Kawazu Z., Tashiro Y., Shima A., Suzuki D., Nishiguci H., Yagi T., and Omura E., "Over 200-mW Operation of Single-Lateral Mode 780-nm Laser Diodes With Window-Mirror Structure," *IEEE J. Sel. Top. Quantum. Electron.*, vol. 7, no. 2, pp. 184-187, March/April, 2001.

Ko. H. C., Cho M. W., Chang J. H., and Yang M., "A new structure of 780 nm AlGaAs/GaAs high power laser diode with non-absorbing mirror," *Appl. Phys. A.*, pp. 467-470, 1999.

Lammert R. M., Smith G. M., Forbes D. V., Osowski M. L., and Coleman J. J., "Strained-layer InGaAs-GaAs-AlGaAs buried heterostructure lasers with nonabsorbing mirrors by selective area MOCVD," *Electron. Lett.*, vol. 31, pp. 1070-1072, 1995.

Lee J. K., Park K. H., Jang H. S., Cho H. S., Park C. S., Pyun K. E., Jeong J., "Improvement of Catastrophic Optical Damage (COD) Level for High-Power 0.98-μm GaInAs-GaInP Laser Diodes Using Impurity Induced Layer," *IEEE Photonics Technology Letters*, vol. 10, no. 9, pp. 1226-1228, Sept. 1998.

Piva P. G., Goldberg R. D., Mitchell I. V., Fafard S., Dion M., Buchanan M., and Charbonneau S., "Reduced 980 nm laser facet heating by band gap shifted extended cavities", J. Vac. Sci. Technol. B.,pp. 1790-1793, Jul./Aug., 1998.

Puchert R., Bärwolff A., Menzel U., Lau A., and Elsaesser T., "Facet and bulk heating of GaAs/AlGaAs high-power laser arryas studied in spatially resolved emission and micro-Raman experiments," *J. Appl. Phys.*, vol. 80, pp. 5559-5563, Nov. 1996.

Shima A., Tada H., Motoda T., Tsugami M., Utakouji T., and Higuchi H., "Reliability Study of 680-nm Visible Laser Diodes with a Window-Mirror Structure," *IEEE J. Sel. Top. Quantum. Electron.*, vol. 3, no. 2, pp. 443-477, Nov./Dec. 2000.

Suzuki Y., Horikoshi Y., Kobayashi M., and Okamato H., "Fabrication of GaAlAs 'Window-Stripe' Multi-Quantum-Well Heterostructure Lasers Utilising Zn Diffusion-Induced Alloying," *Electron. Lett.*, vol. 20, pp. 383-384, 1984.

Tang (1991a):
Tang W. C., Rosen H. J., Vettiger P., and Webb D. J., "Raman microprobe study of the time development of AlGaAs single quantum well laser facet temperature on route to catastrophic breakdown," *Appl. Phys. Lett.*, vol. 58, no. 6, pp. 556-559, Feb. 1991.

Tang (1991b):
Tang W. C., Rosen H. J., Vettiger P., and Webb D. J., "Evidence for current-density-induced heating of AlGaAs single-quantum well laser facets," *Appl. Phys. Lett.*, vol. 59, no. 9, pp. 1005-1007, Aug. 1991.

Tu L. W., Schubert E. F., Hong M., and Zydik G. J., "In-vacuum cleaving and coating of semiconductor laser facets using thin silicon and a dielectric," *J. Appl. Phys.*, vol. 80, pp. 6448-6451, Nov. 1996.

Ueno Y., "Increased Catastrophic-Optical-Damage Output Power for High-Power Semiconductor Lasers Coated with High-Refractive-Index Films," *Jpn., J., Appl., Phys.*, vol. 37, pp. L 646-L648, June 1998.

Welch D. F., "A Brief History of High-Power Semiconductor Lasers," *IEEE J. Sel. Top. Quantum. Electron.*, vol. 6, no. 6, pp. 1470-1477, Nov./Dec. 2000.

Chapter 5

Buried Heterostructure Ridge Laser

5.1 Introduction

As explained in chapter 1, lasers operating in a stable single spatial mode are highly desirable devices. For edge-emitting devices, the main difficulty is obtaining single mode operation in the lateral direction; chapter 2 summarises the difficulties involved. Stabilization of the lateral mode is typically achieved using a narrow laser waveguide of a few micron width, which does not support higher order lateral modes. Confining the optical mode using such a waveguide has the limitation that the output aperture is small, and consequently the optical intensity is high, resulting in mirror degradation leading to catastrophic optical damage (COD). Ridge waveguide and buried heterostructure lasers are typically limited in that the optical and electrical confinement are interdependent; the optical waveguide width is approximately the same as the current aperture. The device requirements to give stable fundamental mode operation and avoid COD are disparate, limiting the power capability of such devices.

This chapter describes the development of a novel ridge laser with a self-aligned buried heterostructure created using quantum well intermixing. The buried heterostructure helps suppress higher order lateral modes and allows wider ridges to operate in the fundamental mode, increasing the power

capability before COD. Optical confinement of the mode is defined by the ridge waveguide, and the electrical confinement by the buried heterostructure. Independent control of the optical and electrical confinement allows modification of the lateral gain profile, reducing the gain of higher order lateral modes relative to the fundamental, thus enhancing laser stability. Furthermore, the buried heterostructure should reduce carrier leakage, leading to reduced threshold currents and increased differential efficiencies. The concept of decoupled optical and electrical confinement has also recently been applied to reduce the threshold currents of an edge-emitting laser [Swint *et al* (2002)].

The buried heterostructure ridge laser design and relevant background information are explained in section 5.2. Analysis of the lateral mode discrimination and hence predicted laser stability are covered in section 5.3. A novel fabrication procedure was developed for these devices as explained in section 5.4. Results from fabricated devices are covered in section 5.5, with particular attention to the lateral far-field characteristics. Conclusions are drawn in section 5.6.

5.2 Device Design and Background

5.2.1 Device Design

Narrow fundamental lateral mode lasers typically suffer from leakage current due to insufficient lateral carrier confinement [Reithmaier *et al* (1998)], the results of which are increased threshold currents and reduced differential efficiencies. As shown in Figure 5.1, the lateral diffusion of the carriers also widens the pumped region of the laser, and hence the gain profile widens. As the mode order increases, the mode overlaps increasingly with the regions adjacent to the waveguide, hence increasing the width of the gain profile reduces the gain of the fundamental mode relative to higher order modes.

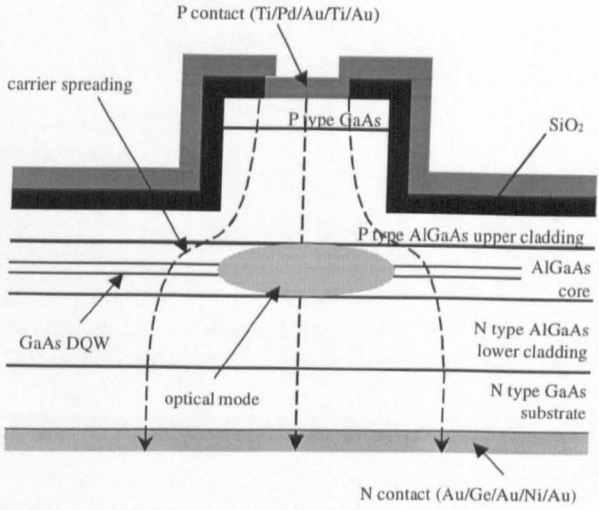

Figure 5.1: Narrow ridge laser suitable for fundamental mode operation.

Research is focussed on the device shown in Figure 5.2. This laser uses a standard ridge structure to provide optical confinement of the mode, and a novel self-aligned buried heterostructure to provide current confinement. The sputtered SiO_2 QWI technique (described in chapter 3) is used to form the buried heterostructure, which is narrower than the ridge, leaving the active central region un-intermixed. The QWI increases the band-gap energy in the regions adjacent to the active central region, providing a means to confine the current. This current confinement should reduce the lateral current spreading, and give a narrower gain width, reducing carrier leakage and increasing the lateral mode discrimination between the fundamental and higher order modes, thus enhancing stability.

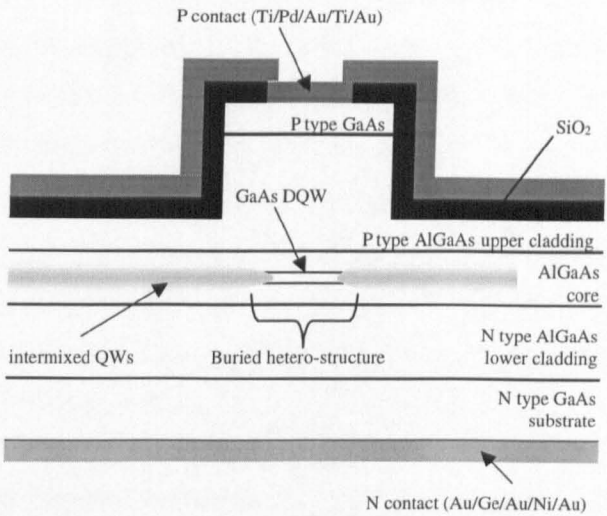

Figure 5.2: Ridge laser with buried heterostructure. Optical confinement of the mode is given by the ridge. The buried heterostructure provides current confinement, thus narrowing the width of the gain region, which is beneficial for lateral mode discrimination, and reduced carrier leakage.

5.2.2 Buried Heterostructures

Lateral current confinement can be obtained using buried heterostructures. This lateral material engineering can also provide the refractive index step necessary for optical confinement of the mode. Buried heterostructure devices can be fabricated by either etch/re-growth or QWI. The independent control of the band-gap energy (by QWI) and refractive index step (by a ridge waveguide) provides the flexibility suitable for complex opto-electronic integrated devices.

5.1.1.1 Buried Heterostructure Lasers Fabricated by Etch/Re-Growth

Buried heterostructure lasers can be fabricated by etching and subsequent epitaxial re-growth. A current blocking layer on either side of the active stripe provides the lateral electrical confinement necessary for reducing the leakage current. Additionally, this current blocking layer can also provide the refractive index step necessary for waveguiding, providing a very elegant solution to index guided semiconductor lasers. Horie *et al* (2000) demonstrated a 980 nm single lateral mode laser using this etch and re-growth

approach. The laser showed fundamental mode operation up to 500 mW CW, demonstrating the capability of the technique for high performance laser diodes suitable for pumping erbium doped fibre amplifiers (EDFAs). Imafuji *et al* (1999) used a similar approach to fabricate 650 nm AlGaInP high power laser diodes suitable for high density optical data storage. Although capable of fabricating high performance laser diodes, the re-growth approach to fabricating opto-electronic devices is far from ideal, especially as devices become more complex, requiring greater functionality and chip area. Re-growth is particularly problematic in Al containing alloys.

5.1.1.2 Buried Heterostructures Fabricated by Quantum Well Intermixing

Quantum well intermixing's ability to laterally control the alloying of a QW with its barriers is ideally suited to forming buried heterostructures. Electrical confinement is provided by the step in band-gap energy from non-intermixed to intermixed material. Various approaches to forming a buried heterostructure using QWI have been successfully demonstrated, and these are summarised in the paragraphs below.

Thornton *et al* (1985) used silicon impurity induced disordering (IID) to form a buried heterostructure double QW (DQW) GaAs-AlGaAs laser. Lateral regions adjacent to a narrow stripe were intermixed using a silicon film for IID. No etching of a ridge, or complicated epitaxial re-growth was required. Threshold currents for these devices ranged from ~10 mA to ~3 mA for stripe widths of 8 μm to 1 μm respectively. Devices without this buried heterostructure electrical confinement displayed threshold currents that were relatively independent of stripe width for widths below 8 μm, due to lateral current diffusion. This reduction in threshold currents clearly demonstrated the effectiveness of the Si IID for forming the buried heterostructure required for current confinement. Since the Si is an n-type dopant, the diffusion of the Si into the p-doped layers forms an electrical current blocking effect as well.

Welch *et al* (1987) used silicon implanted IID to form a buried heterostructure multiple QW (MQW) GaAs-AlGaAs laser. To limit the effect of implantation induced damage, the Si diffusion source was implanted near the crystal surface, and then diffused through the wafer at 850 °C for 3 hours. The lateral heterostructure was formed by IID on either side of an un-intermixed active stripe. A 4 μm wide laser fabricated using this process displayed a threshold current of 17 mA, and operation in the lowest order lateral mode for powers up to 20 mW. Evanescently coupled multiple stripe lasers were also fabricated using this Si implantation IID process.

Reithmaier *et al* (1998) have shown how focussed ion beam (FIB) implantation of GaAs-AlGaAs and GaInAsP-InP, followed by annealing can be used for QWI defined buried heterostructures. The implantation species was Ga, the implantation of which creates defects, which enhance the interdiffusion rate during annealing. They applied their FIB QWI technology for lateral band-gap engineering for a) waveguiding, and b) current confinement. Lateral waveguiding can be achieved in MQW structures where intermixing of the QWs can be used to create a refractive index step sufficient for waveguiding. By implanting species on either side of an un-implanted region, followed by annealing, they managed to fabricate passive GaInAsP waveguides. This process appears very elegant for waveguide fabrication, though one limitation is the need for many QWs to obtain a sufficient index step for waveguiding. They also applied their FIB QWI technique to laterally confine the current in a GaInAsP QW 2 μm wide ridge laser. The lateral current confinement devices showed reduced threshold currents and increased differential efficiencies when compared to devices without lateral current confinement.

Hu *et al* (1995) demonstrated sub-milliampere threshold InGaAs-GaAs QW ridge lasers using silicon IID to provide lateral current confinement. The approach used was to first dry etch the ridge waveguide, followed by deposition of a Si film, and then ampoule annealing at 850 °C with an arsenic overpressure. Intermixing after forming the ridge has the advantages of self-

aligning the buried heterostructure to the ridge, reducing the required diffusion depth, and consequently increasing the spatial resolution of the QWI, however care must be taken to ensure that residual dry-etch damage does not cause problems during the annealing.

Jiang *et al* (1998) demonstrated how SiO_2 IFVD can be used in a MQW AlGaAs-GaAs laser structure to achieve lateral mode control. Intermixing of the MQW structure on either side of a 4 μm wide stripe creates a sufficient refractive index step to form a waveguide (and will give lateral current confinement). The laser using intermixing on either side of the stripe displayed superior light-current characteristic (linear to higher power) and single-mode operation (far-fields) to 4 I_{th}, which was superior to the standard device.

5.2.3 Alternative Lateral Stabilization Techniques

Higher order lateral modes are less well confined in the waveguide; as the order increases the mode overlaps less with the central region of the waveguide. One approach to lateral mode stabilization is to increase the loss in the regions adjacent to the waveguide; higher order modes overlap more with these regions and hence their modal loss relative to the fundamental mode is increased, reducing the possibility of them oscillating. This approach to modal stabilization was demonstrated in 980 nm GaInAs-GaInP ridge lasers using Si as the implant source to increase the losses adjacent to an un-implanted active region [Lee *et al* (2000)].

Oxidation of buried AlGaAs layers can provide both current and optical confinement in semiconductor lasers, enhancing performance [Cheng *et al* (1996)]. This is usually performed by etching through the layer to be oxidised, followed by lateral oxidation from the sides of the device. The native oxide is an insulator, thus providing the current aperture. Furthermore, the oxide has a much lower refractive index than the non-oxidised material, and therefore can provide the lateral index step required for index-guided waveguides. Cheng *et*

al (1996) demonstrated reduced threshold currents and good beam profiles using native oxidation of AlAs layers in edge-emitting lasers.

Control of the lateral current profile has proven successful for improved lateral mode stability in broad area semiconductor lasers suitable for high power operation. O'Brien *et al* (1998) demonstrated how a thick (10 μm) p-GaAs cap layer on an epitaxial wafer can be used to smooth the lateral current injection profile by diffusion. They called the device the enhanced current spreading (ECS) laser. Lasers with a 5 μm current injection stripe were made using this design. The measured near-field width of the laser was on the order of 30 μm, clearly demonstrating the diffusive property of the thick p-GaAs layer. Lasers from an identical wafer design, but without the thick p-GaAs current spreading layer were compared to this novel laser. As the near-field width of the ECS laser was around 30 μm, a standard laser of width 30 μm was compared to the ECS laser. The standard laser showed poor far-field characteristics, typical of lateral mode instability. The ECS laser showed much better far-field characteristics; single lobed operation up to 300 mW per facet was observed. Clearly the thick current spreading layer smoothes the lateral current profile, giving a smoothed lateral gain profile, which helps stabilise the lateral mode. Simplicity and inexpensive fabrication are advantages of this ECS laser. Patterning of the contact pad has also been proven effective in smoothing the lateral current, and hence gain profile. Skovgaard *et al* (1998) demonstrated a novel digitated contact pad designed to smooth the edges of the lateral distribution of injected carriers. Lasers made with this type of current profiling displayed improved near-field stability compared to standard broad area lasers. Again, the smoothing of the current and gain profiles helps stabilise the lateral mode. This approach to stabilisation has the advantages of simple fabrication, and use of standard wafer structures.

5.3 Lateral Mode Discrimination

Higher order lateral modes are less well confined in the waveguide; as the order increases the mode overlaps less with the central region of the waveguide. Assuming that gain is confined to the un-intermixed region (defined by the buried heterostructure), then narrowing the gain width in the central region of the waveguide can reduce the gain of the higher order modes relative to the fundamental, enhancing stability. To illustrate this concept a simulation of a ridge waveguide is performed, followed by calculation of the relative modal gains and analysis of the lateral mode discrimination, which is useful for assessing the likely modal stability. Carlson (1994) gives a useful discussion of modal discrimination in laser arrays, the basic concept of which is applied in this section, but for the case of lateral mode discrimination in a single laser.

Figure 5.3 shows the model of a ridge waveguide structure simulated using the FIMMWAVE software (see section 2.5). A ridge width of 5 μm, and a remaining thickness of 50 nm of upper cladding were chosen such that the fundamental, first order and second order modes were supported. The typical ridge width for fundamental mode operation would be in the region of around 2.5 to 3 μm (see section 2.5 for more details), however higher order modes are required to illustrate the concept of improved lateral mode discrimination, hence a wider and deeper waveguide was chosen. No QWs were included in the simulation as the QWs are narrow enough not to influence the effective index significantly. The region above the structure has a refractive index of 1.

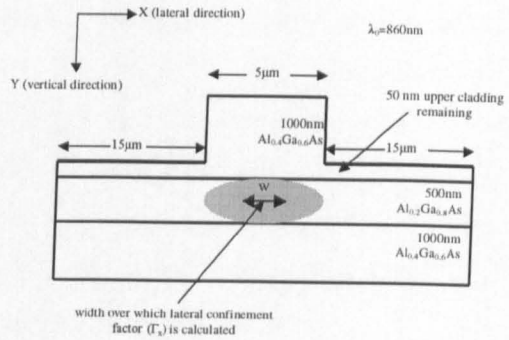

Figure 5.3: Model of ridge waveguide simulated using FIMMWAVE software.

Figure 5.4 shows the intensity profiles of the lateral modes supported by the waveguide in Figure 5.3. The waveguide supports the fundamental, first order, and second order lateral modes; higher order modes than these are not supported. As the mode order increases, the mode is less well confined in the waveguide, thus the overlap with the central region of the waveguide is reduced.

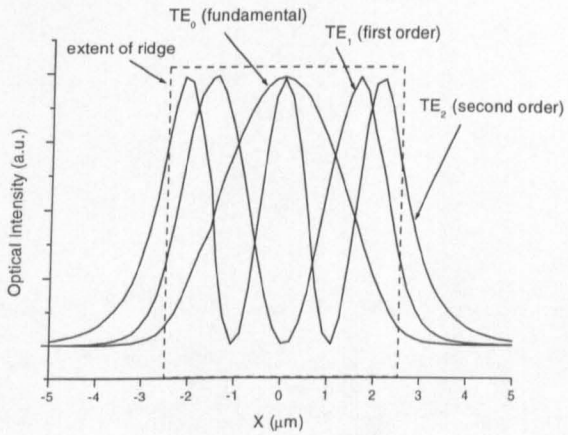

Figure 5.4: Lateral mode intensity profiles of the ridge waveguide shown in Figure 5.3.

Only a portion of the optical mode intensity overlaps with the active gain section and experiences gain. Calculation of the modal gain therefore requires analysis of the mode overlap with the gain section in the x (lateral) and y

(vertical) directions. Assuming that the lateral and vertical mode profiles are independent of each other (lateral profile defined by the ridge, vertical profile by the epitaxial wafer structure), the modal intensity overlaps in the lateral and vertical directions are given by the confinement factors $\Gamma_{x:L}$ and $\Gamma_{y:V}$ respectively, where L and V are the mode orders in the lateral and vertical directions respectively. The lateral confinement factor ($\Gamma_{x:L}$) is determined by Eq. (5.1), where $\Phi_L(x)$ is the intensity profile of the L^{th} order lateral mode in the x direction, and w is the lateral width of the active gain section, defined by the width of the buried heterostructure.

$$\Gamma_{x:L} = \frac{\int_{-w/2}^{w/2} \Phi_L(x)\,dx}{\int_{-\infty}^{\infty} \Phi_L(x)\,dx} \qquad Eq.(5.1)$$

The vertical confinement factor ($\Gamma_{y:V}$) is given by Eq. (5.2), where $\Phi_V(y)$ is the intensity profile of the V^{th} order vertical mode in the y direction, and d is the width of the active section (QW) assuming only a single QW is present in the waveguide.

$$\Gamma_{y:V} = \frac{\int_{-d/2}^{d/2} \Phi_V(y)\,dy}{\int_{-\infty}^{\infty} \Phi_V(y)\,dy} \qquad Eq.(5.2)$$

The modal gain of the L^{th} order lateral, V^{th} order vertical mode is determined by multiplying the total intensity overlap with the gain of the QW, as shown in Eq. (5.3), where $g_{L,V}$ is the modal gain, and G is the gain of the QW (assuming only a single QW is used).

$$g_{L,V} = \Gamma_{x:L}\,\Gamma_{y:V}\,G \qquad Eq.(5.3)$$

When multiple QWs are used, then the intensity profile overlap with each QW must be calculated, and the gain contribution from each QW summed.

Assuming the confinement factor to be identical for each of n QWs, then the modal gain is given by Eq. (5.4).

$$g_{L,V} = n\ \Gamma_{x:L}\Gamma_{y:V}\ G \qquad Eq.(5.4)$$

When assessing the lateral mode stability of lasers, it is of interest to perform a simple calculation of the discrimination of the fundamental mode against higher order lateral modes. This modal discrimination, defined as the gain of the fundamental mode divided by the gain of the higher order mode, gives an insight into the likely modal stability of the device; the higher the modal discrimination, the more likely the laser will operate in a stable fundamental lateral mode. Typically, due to current spreading, the gain profile of a laser is wider, or similar to the optical mode profile, hence $\Gamma_{x:L}$ is close to unity. However, in the case where the gain can be confined to a narrower width than the optical mode, using a buried heterostructure for example, the lateral mode discrimination is dependent on the gain width. Since both $\Gamma_{y:V}$ and G would be expected to be independent of the lateral mode, the lateral mode discrimination can be assessed by dividing the lateral confinement factor of the fundamental mode by the confinement factor of the higher order mode. Figure 5.5 shows the fundamental lateral mode discrimination of the ridge waveguide shown in Figure 5.3, where w is the width of the gain section (assumed to be in the exact centre of the waveguide). As the first order mode has an intensity minimum at the centre of the waveguide, clearly a very narrow gain section in the centre of the laser offers excellent discrimination against the first order mode. However, the second order mode has a maximum at the centre, and therefore experiences a significant overlap with the narrow gain section; there is a maximum discrimination when the gain width is just below 3 μm. As the gain width is increased beyond the ridge width, the modal overlaps with the gain tends toward unity, and hence the discrimination becomes poor. For demonstration purposes, the waveguide was designed to support the fundamental, first order, and second order modes; however, by designing the waveguide such that it cannot support the second order mode (use a narrower waveguide, or shallower etch depth), then by using a very narrow gain region it should be possible to

achieve excellent modal stability since the discrimination against the first order mode is very high.

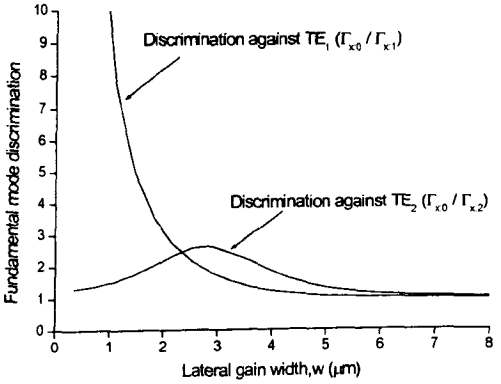

Figure 5.5: Fundamental mode discrimination against first and second order lateral modes for the ridge waveguide shown in Figure 5.3. The modal discrimination is defined as the gain of the fundamental divided by the gain of a higher order mode, which is the ratio of the lateral confinement factor of the fundamental mode divided by the confinement factor of the higher order mode.

This analysis of the modal discrimination is rather simplistic, ignoring the effects of modal loss, carrier depletion and gain saturation, and is therefore only valid near threshold, however good discrimination at threshold is often a good indication of modal stability at high power levels [Carlson (1994)], hence assessing the discrimination gives a useful insight into the likely characteristics of the laser. From this simple analysis it is clear that narrowing the gain width has the potential to improve lateral mode stability.

The concept of stabilisation using a narrow gain section in the centre of the waveguide is also used in the vertical mode direction. Assuming the gain (QW) is narrow and in the centre of the waveguide, the overlap of the first order vertical mode with the gain is much smaller than the fundamental mode, and hence is unlikely to have sufficient gain to oscillate. By designing the epitaxial waveguide to be near the second order mode cut-off, the vertical spot size at the facet can be expanded, which is beneficial for high power devices [Botez (1999)].

5.4 Device Fabrication

5.4.1 Fabrication Process

Since very accurate alignment of the ridge to the buried heterostructure is required for this device, the standard fabrication procedure for ridge waveguide lasers with intermixed sections was unsuitable, hence a novel fabrication process was developed. Standard processing could not be used since the typical photolithography alignment accuracy achieved in the clean room is on the order of 0.5 μm, plus a small angular error. Furthermore, since the ridge requires alignment to the intermixed buried heterostructure, which is invisible, it would have to be aligned to markers, making high accuracy alignment very difficult. Given the fact that the buried heterostructure must be in the exact centre below the ridge, an elegant solution was developed, removing the alignment inaccuracies, and simplifying processing. The solution is based on using a thick PECVD SiO_2 layer for both suppressing the intermixing, and as an etch mask for the ridge, hence the ridge waveguide is self-aligned to the buried heterostructure. During intermixing, lateral diffusion of the point defects means that the un-intermixed active region is narrower than the ridge, which is a requirement for increased lateral mode discrimination, although exact control of the buried heterostructure width is difficult to achieve. Standard and buried heterostructure ridge lasers were fabricated on the same chip for comparison, and the fabrication sequence is shown in Figure 5.6 to Figure 5.11.

The first processing step was to form the thick PECVD SiO_2 ridge used for both the intermixing suppressant, and the etch mask for the ridge waveguide. Deposition of the 500 nm PECVD SiO_2 was performed, followed by photolithographic definition of the ridge using S1818 photoresist. The photoresist pattern was then transferred into the SiO_2 layer using CHF_3 RIE (see section 2.6 for more details on the fabrication processes used). The remaining photoresist was then removed in acetone, leaving a SiO_2 ridge (see Figure 5.6), the width of which defines the buried heterostructure and ridge

waveguide. The SiO_2 depth was chosen to be 500 nm to provide sufficient protection against the sputtering process, and therefore suppress intermixing (see section 3.3 for more details).

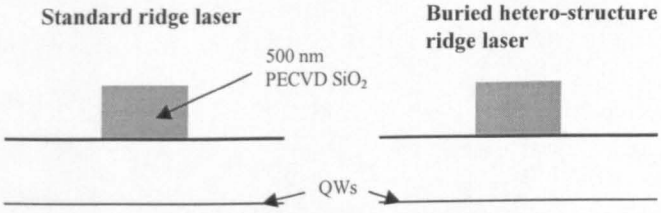

Figure 5.6: Thick PECVD SiO_2 layer on semiconductor surface, used for suppressing the intermixing, and as etch mask when dry etching the ridge waveguide. Photolithography and dry etching using CHF_3 were used to define the ridge.

The next processing step was to deposit the dielectrics required for intermixing the buried heterostructure laser, and suppressing intermixing in the standard ridge laser, as illustrated in Figure 5.7. Photolithography using chlorobenzene soaked S1818 photoresist (the chlorobenzene soak makes subsequent lift-off easier) was used to cover the area containing the standard devices, leaving no resist in the areas containing the buried heterostructure laser. Sputtering of 50 nm of intermixing SiO_2 was then performed, followed by lift-off in acetone. The S1818 resist is sufficiently thick to protect the standard devices from the sputtering process. Evaporation of 50 nm SiO_2 was then performed, to cover the sample surface.

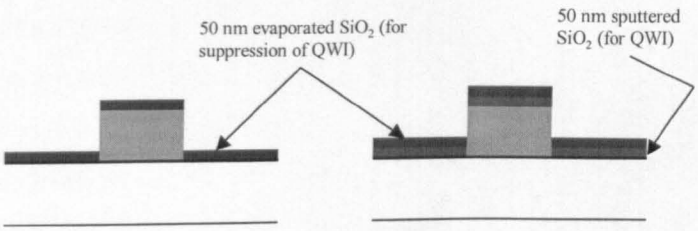

Figure 5.7: After deposition of dielectrics required for suppressing intermixing (standard ridge laser), and intermixing (buried heterostructure laser). Photolithography and lift-off processing are used to define which areas of the chip are covered with the 50 nm of sputtered SiO_2 used for intermixing.

Annealing of the sample was then performed to diffuse the point defects through the wafer, causing intermixing under the sputtered SiO_2 regions, as

shown in Figure 5.8. Lateral diffusion of the point defects under the thick PECVD SiO_2 layer causes the width of the un-intermixed active section to be narrower than the ridge, thus providing the narrowed gain width required for improved lateral mode discrimination. From previous experiments within the department [Helmy *et al* (1999)], the buried heterostructure is believed to be around 3 μm narrower than the ridge width. Since standard ridge lasers of widths 4 μm and 5 μm would typically yield lasers with unstable lateral modes, these widths are ideal for investigating the possibility of improved lateral mode discrimination and hence stability of these novel buried heterostructure ridge lasers.

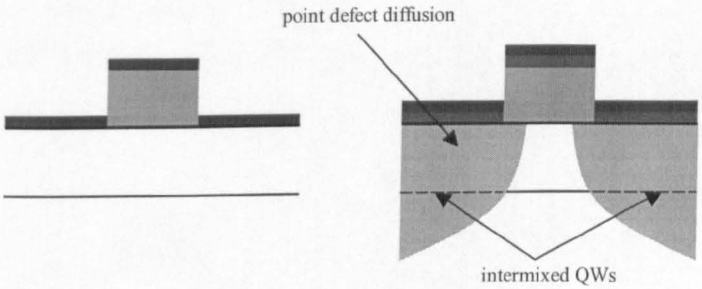

Figure 5.8: Devices after annealing, showing extent of intermixing. The QWs in the standard device are not intermixed. Diffusion of the point defects in the buried heterostructure device causes intermixing, forming the buried heterostructure. Lateral diffusion of the point defects causes the un-intermixed active section to be narrower than the ridge width. Photoluminescence on annealed test samples is used to investigate the QWI process.

Removal of the sputtered and evaporated SiO_2 was then performed using CHF_3 RIE. Since the etch selectivity of the SiO_2 to the GaAs is high, an over-etch is used to ensure removal of all the sputtered and evaporated SiO_2, without significant etching of the GaAs surface. A ridge of PECVD SiO_2 remains (as shown in Figure 5.9) and this is used as the dry-etch mask when etching the ridge waveguide.

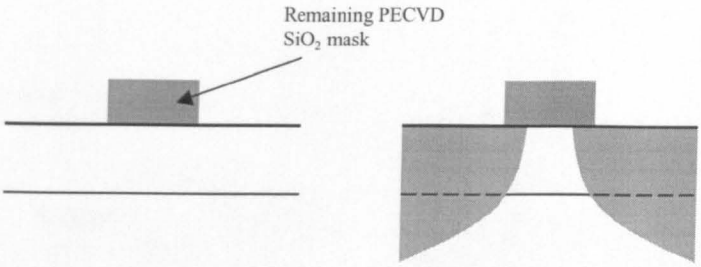

Figure 5.9: After dry etching of a thin layer of SiO_2 using CHF_3 RIE. All the sputtered and evaporated SiO_2 is removed by the etch, leaving a ridge of PECVD SiO_2, sufficient to form a good etch mask when dry etching the ridge waveguide.

RIE using $SiCl_4$ is then performed to etch the ridge waveguide, leaving the ridge waveguide as shown in Figure 5.10. Laser interferometry is used, ensuring the precise control of the etch depth required for good ridge waveguides.

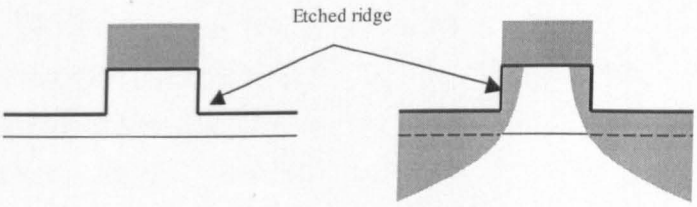

Figure 5.10: After dry etching the ridge waveguide.

A PECVD SiO_2 isolation layer is then deposited, followed by photolithography and etching to open up the contact window on top of the ridge. Deposition of the p-type contact is then performed, followed by angular evaporation of Ti(15 nm)/Au(100 nm) at approximately 45° to ensure that both side-walls are covered, giving the devices shown in Figure 5.11. The sample is then thinned to around 150 μm, and the n-type contact is deposited. Contact annealing at 360 °C for 60 s is then performed, and finally cleaving the devices completes the fabrication sequence.

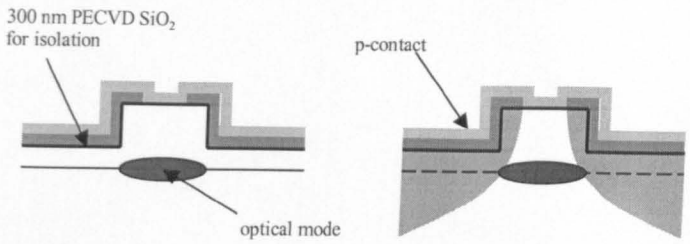

Figure 5.11: After deposition of a 300nm thick PECVD SiO_2 isolation layer, followed by opening of the contact widow using photolithography and etching, and finally deposition of the p-type contact.

5.4.2 Photoluminescence and QWI Analysis

Figure 5.12 shows the photoluminescence spectra from intermixed and suppressed test samples annealed alongside the actual laser sample at 875 °C for 60 s. The as-grown sample was not annealed, and has a peak at 809 nm. Both the evaporated SiO_2 and PECVD SiO_2 covered samples showed a 1 nm blue-shift (from as-grown) after annealing, demonstrating the effectiveness of these caps at suppressing intermixing, as desired. The sputtered SiO_2 sample showed a blue-shift of 48 nm from as-grown, giving a differential shift of 47 nm between the intermixed and suppressed regions. This differential blue-shift is typical for such annealing conditions. Although a larger blue-shift could be obtained by using a higher anneal temperature (or longer time), significant undesired intermixing will take place under the suppressing SiO_2.

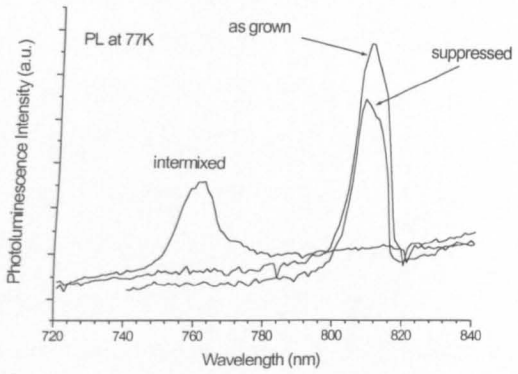

Figure 5.12: PL spectra from as-grown, intermixed and suppressed test samples.

5.4.3 Fabricated Devices

Figure 5.13 shows a SEM image of a 5 μm wide standard ridge laser fabricated using the process detailed in section 5.4.1. Fabrication appears to have been successful. The ridge was etched to around 50 nm above the waveguide core region. The dark SiO_2 isolation layer is clearly visible. Although the contact window is not exactly in the centre of the waveguide, current spreading in the heavily p-doped cap layer should ensure uniform injection.

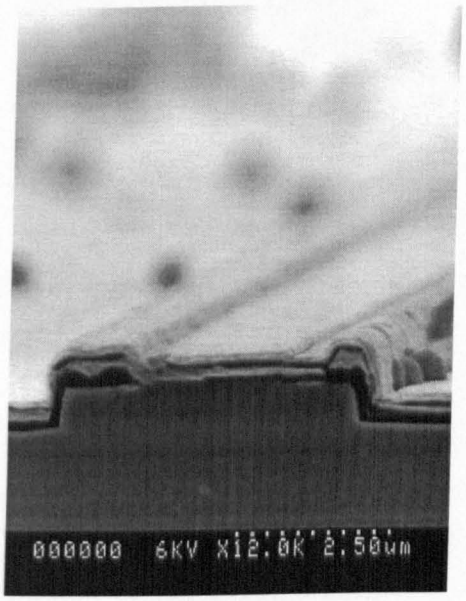

Figure 5.13: SEM image of a standard 5 μm wide ridge laser device fabricated using this process.

Figure 5.14 shows a SEM image of a 4 μm wide buried heterostructure laser. Comparison with the standard ridge laser shows that the buried heterostructure ridge laser looks relatively poor, the apparent reason being "grass" on the intermixed regions adjacent to the ridge. This "grass" appears to be due to micro-masking, i.e. contamination on the surface of the intermixed regions acts as an etch mask during etching of the ridge. Even so, the etched ridge looks good, and the contact to the cap layer is clearly visible. Although not perfect, it is clear that this fabrication process is capable of producing devices.

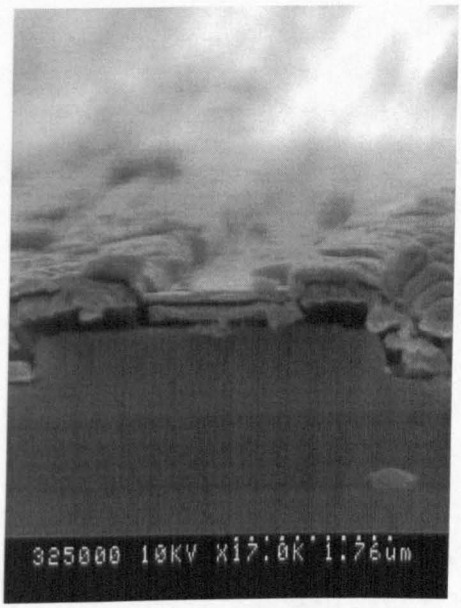

Figure 5.14: SEM image of a buried heterostructure 4 μm wide ridge laser fabricated using this process.

Fabrication of these devices was complicated by two major difficulties, and numerous attempts were made before production of reasonable devices. Firstly, when annealing at high temperatures, the thick SiO_2 layer used for suppressing intermixing and etching the ridge can degrade, resulting in a poor etch mask for dry etching the ridge. Secondly, the intermixed regions tended to suffer from "grass" when etching the ridge; the reason for this is not understood as the un-intermixed regions were relatively "grass" free, hence it is

not just a simple case of pre-etch contamination on the sample surface. The combined effect of both of these fabrication difficulties was a low device yield.

5.5 Results and Discussion

Experimental results from successfully fabricated devices are described in this section, with particular attention paid to the lateral mode stability of both standard and buried heterostructure ridge lasers. The purpose of this experiment was to compare device performance of the buried heterostructure and standard ridge lasers, hence the relative performance is more important than the exact operating figures. Devices were tested under the pulsed conditions described previously in section 4.5.

5.5.1 Standard Ridge Laser

Figure 5.15 shows the light-current and lateral far-field characteristics of a 600 μm long, 4 μm wide standard ridge waveguide laser fabricated using this novel process. The threshold current of 45 mA and external quantum efficiency of 45% are slightly poor for such a device, but even so it demonstrates that the fabrication process is capable of producing reasonable devices. At low drive currents, the far-field shows a single dominant lobe, indicating fundamental mode operation. As the drive current is increased above 200 mA, the beam profile deteriorates, indicating instability of the spatial mode. No obvious kinks are present in the light-current characteristic in the transition region from fundamental mode operation to spatial mode instability. Therefore, a lack of kink in the light-current characteristic does not necessarily signify spatial mode stability; beam characteristics must be investigated.

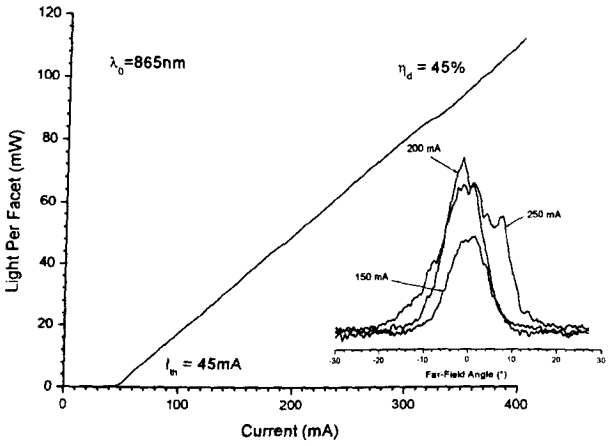

Figure 5.15: Light-current and lateral far-field characteristics of 4 μm wide standard ridge laser. The device is 600 μm long, and has no facet coatings.

Figure 5.16 shows the light-current and lateral far-field characteristics of a 600 μm long, 5 μm wide standard ridge laser. The threshold current of 40 mA is slightly lower than that of the 4 μm device. On first inspection this appears slightly confusing, since one would expect the narrower device to have a lower threshold current, however, the effect of ridge loss mechanisms must be considered; ridge roughness and scattering losses would be more pronounced for narrower ridge devices, hence one would expect higher losses for narrower devices, leading to increased threshold current densities and lower differential efficiencies. Furthermore, current spreading in such narrow devices means that the threshold current can be relatively independent of ridge width. The external quantum efficiency of the device was 53 %, which was 8 % greater than the 4 μm device, possibly due to lower losses in the wider device. One must also consider that microscopic differences between such narrow ridge devices will cause slight variations in device operating characteristics. Clearly the device is not operating with a single spatial mode, leading to poor far-field characteristics. The ridge width is too wide to operate in the fundamental lateral mode. Like the 4 μm device, the light-current characteristic is linear,

and no obvious kinks are present, further evidence that lack of kinks does not necessarily imply stable single mode operation.

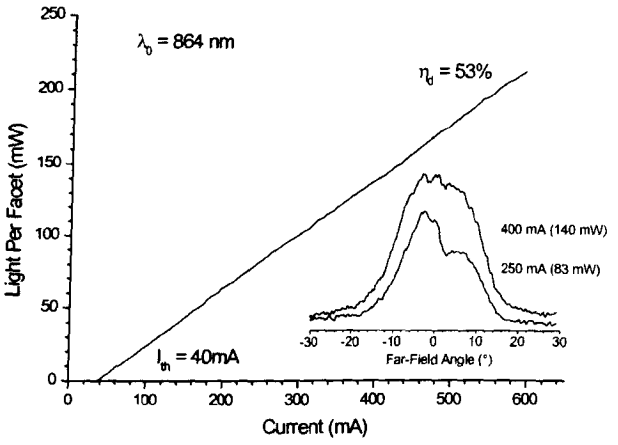

Figure 5.16: Light-current and lateral far-field characteristics of 5 μm wide standard ridge laser. The laser is too wide to operate in the fundamental mode.

5.5.2 Buried Heterostructure Ridge Lasers

Figure 5.17 shows the light-current and lateral far-field characteristics of a 4 μm wide buried heterostructure laser. Initially the characteristic is linear, with an external quantum efficiency of 46 %, as indicated by the dashed line. However, starting at around 300 mA a non-linearity can be seen. After the non-linearity, the characteristic becomes linear again, though at a slightly lower external quantum efficiency than in the initial linear part of the characteristic. This non-linearity is gradual, not a sharp kink typical of lateral mode instability. The threshold current of the device was 85 mA, compared to the standard 4μm wide device having a threshold of 45 mA. The likely reasons for the increase in threshold current are discussed in section 5.5.3. Therefore it is inconclusive whether the buried heterostructure lasers have the potential for lower threshold currents. The lasing wavelength of 864 nm is similar to that of the standard ridge lasers, implying that the central active region of the buried heterostructure laser is not significantly intermixed, and thus the lateral spatial resolution of the intermixing process is sufficient to fabricate such devices. Clearly the spatial mode remains dominantly single mode even up to 500 mA

drive current. As single mode operation is maintained beyond the non-linearity seen in the light-current characteristic, this implies that the non-linearity does not mean a deterioration in the spatial mode.

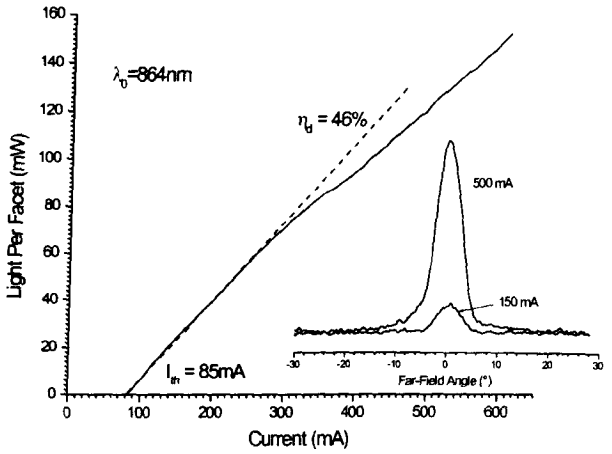

Figure 5.17: Light-current and lateral far-field characteristic of 4 μm wide buried heterostructure ridge laser (600 μm long).

Figure 5.18 shows the light-current characteristic of the 5μm wide buried heterostructure ridge laser. Again, a non-linearity can be seen; the characteristic is linear before and after this. The threshold current and external quantum efficiency were 85 mA and 47 % respectively, almost identical to the 4 μm wide buried heterostructure ridge laser. The far-field profile shows dominantly single-mode operation, and although slight deterioration can be seen at 500 mA, the beam still has one dominant lobe; proof that the buried heterostructure helps reject higher order lateral modes.

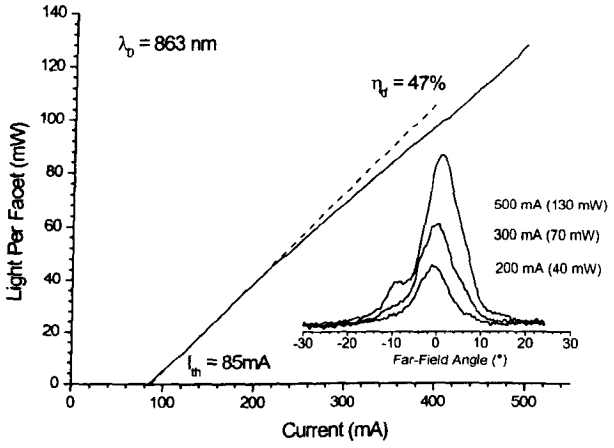

Figure 5.18: Light-current characteristic of 5 μm wide buried heterostructure ridge laser (600 μm long). Single-mode operation is evident from the far-field profile.

5.5.3 Discussion

Comparison of the light-current characteristics of the devices shows an increase in threshold current and slight reduction in external quantum efficiency when a buried heterostructure is used. Since this QWI process has been used to demonstrate waveguides with low losses, the increase in threshold current is likely to be due to a combination of a reduced lateral confinement factor, and losses related to the novel fabrication scheme, though exact analysis of each contribution is difficult to make accurately. Therefore it is inconclusive whether buried heterostructure ridge lasers fabricated in this way have the potential for reduced threshold currents.

Measurements of the operating wavelengths of the devices revealed that the buried heterostructure devices have similar lasing wavelengths to the standard devices. This implies that the lateral spatial resolution of the intermixing process is sufficient to fabricate such devices.

Beam profile characteristics of the buried heterostructure lasers appear to be far superior to the standard ridge lasers; fundamental lateral mode operation of 4 μm and 5 μm wide buried heterostructures was observed, whereas the

standard ridge lasers are too wide to operate in a stable fundamental lateral mode. The standard 4 μm wide ridge laser showed a linear light-current characteristic, and fundamental lateral mode operation at low drive levels, though the beam deteriorates at higher drive levels. The standard 5 μm wide ridge laser also showed a linear light-current relationship, but the beam profile revealed an unstable spatial mode even at low drive currents. As both of these devices displayed kink-free linear light-current characteristics and lateral mode instability, it appears that a linear light-current relationship does not guarantee a stable spatial mode; the beam profile must be characterised. Both the 4 μm and 5 μm wide buried heterostructure devices have non-linearities in their light-current characteristics, though below and above the non-linearity the characteristic is linear. The non-linearity is not like the sharp kinks often associated with spatial mode instability. Beam profiles from the 4 μm wide buried heterostructure laser showed a stable lateral mode even up to 500 mA drive current, giving around 120 mW of power. The 5 μm wide buried heterostructure laser showed fundamental mode operation up to 300 mA, after which the beam deteriorated, but still remained in a single dominant lobe. Clearly the beam characteristics of the buried heterostructure devices are far superior to the standard ridge devices, due to the improved lateral mode discrimination attained by using the narrower gain width. However, one must also consider the effects of additional losses introduced by the "grass" in the buried heterostructure lasers; this would likely be a scattering loss, and as higher order modes would interact more with these regions than the fundamental, then the loss of higher order modes relative to the fundamental would increase, enhancing modal stability.

5.6 Conclusions

De-coupling of the optical and electrical confinement offers interesting benefits for semiconductor lasers, allowing greater flexibility in the device design and potentially superior performance. The most promising aspects of this research were the improved spatial mode characteristics and stability of the buried heterostructure ridge lasers compared to the standard ridge lasers.

Fundamental lateral mode operation up to higher powers was observed when the buried heterostructure was used, indicating improved lateral mode discrimination, as predicted in section 5.3. Furthermore, the improved lateral mode discrimination allows the ridge width to be widened and still operate in the fundamental mode, allowing the potential for reduced optical intensity at the facet, or greater COD levels, beneficial for high power operation. However, the effect of the "grass" on the buried heterostructure devices cannot be ignored; as the mode order increases the light overlaps increasingly with the "grassy" region, hence if this region is lossy then the "grass" itself may help improve the lateral mode discrimination by increasing the losses of higher order modes relative to the fundamental.

The results of this research are inconclusive as to whether the sputtered SiO_2 intermixing process can be used to reduce the threshold current of ridge lasers. Lasers with the lateral buried heterostructure suffered from "grass", hence a likely increase in propagation loss, which may explain the increase in threshold current when the buried heterostructure is used. Furthermore, the reduced lateral confinement factor also influences the threshold current. For a true comparison of the standard ridge laser to a buried heterostructure ridge laser, the fabrication quality must be similar. Ideally, the best way of assessing the capability of the sputtered SiO_2 intermixing process to form a buried heterostructure would be to use gain guided oxide stripe lasers with and without the buried heterostructure, although these are very difficult to fabricate using a self-aligned process.

Very accurate alignment of the ridge to the buried heterostructure was required, hence a novel self-aligned process was developed; a thick SiO_2 layer was used for both suppressing the intermixing, and as etch mask when dry-etching the ridge. Although the process proved capable of fabricating devices, difficulties were experienced; the post-annealed ridge etch mask was not ideal, and the buried heterosturcture lasers suffered from "grass" in the etched regions. An alternative approach to the self-aligned processes would be to use the

extremely high alignment accuracy offered by electron beam lithography (EBL), though this would have required significant alteration of the processes used. From the lasing wavelengths of devices it was apparent that the spatial resolution of the intermixing process was sufficiently good to form the buried heterostructure in devices of ridge widths 4 and 5 μm.

5.7 References

Botez D., "Design considerations and analytical approximations for high continuous-wave power, broad-waveguide diode laser", *Appl. Phys. Lett.*, no.21, pp. 3102-3104, May 1999.

Carlson N. W., "Monolithic Diode-Laser Arrays," published by Springer, 1994.

Cheng Y., Dapkus P. D., MacDougal M. H., and Yang G. M., "Lasing Characteristics of High-Performance Narrow-Stripe InGaAs-GaAs Quantum-Well Lasers Confined by AlAs Native Oxide", *IEEE Photonics Technology Letters*, vol. 8, no. 2, pp. 176-178, February 1996.

Hayson J. E., Delâge A., He J., Koteles E. S., Poole P. J., Feng Y., Goldberg R. D., Mitchell I. V., and Charbonneau S., "Experimental Analysis and Modelling of Buried Waveguides Fabricated by Quantum-Well Intermixing," *IEEE J. Quantum Electronics*, vol. 35, no. 9, pp. 1354-1363, September 1999.

Helmy A. S., Johnson N. P., Ke M. L., Bryce A. C., Aitchison J. S., Marsh J. H., Gontijo I., Buller G. S., Davidson J., Dawson P., "A Study of Impurity-Free Vacancy Disordering in GaAs-AlGaAs for Improved Modelling", *IEEE J. Selected Topics in Quantum Electronics*, vol. 4, no. 4, pp. 661-668, July/August 1998.

Helmy A. S., A. C. Bryce, Ironside C. N., Aitchison J. S., Marsh J. H., and Ayling S. G., "Optical Diagnosticts of Microstructures Fabricated Using Quantum Well Intermixing," MRS 1999 Fall Meeting, Boston, 29 November – 3 December 1999.

Horie H., Arai N., Mitsuishi Y., Komuro N., Kaneda H., Gotoh H., Usami M., and Matsushima Y., "Greater than 500-mW CW Kink-Free Single Lateral-Mode Operation of Weakly Index Guided Buried-Stripe Type 980-nm Laser Diodes," *IEEE Photonics Technology Letters*, vol. 12, no. 10, pp. 1304-1306, October 2000.

Hu S. Y., Peters M. G., Young D. B., Gossard A. C., and Coldren L. A., "Submilliampre-Threshold InGaAs-GaAs Quantum-Well Ridge-Waveguide Lasers with Lateral Confinement Provided by Impurity Induced Disordering," *IEEE Photonics Technology Letters*, vol. 7, no. 7, pp. 712-714, July 1995.

Imafuji O., Fukuhisa T., Yuri M., Mannoh M., Yoshikawa A., and Itoh K., "Low Operating Current and High-Temperature Operation of 650nm AlGaInP High-Power Laser Diodes with Real Refractive Index Guided Self-Aligned Structure," *Selected Topics in Quantum Electronics*, vol. 5, no. 3, pp. 721-728, May/June 1999.

Jiang A. Q., Sun C. Z., Hao Z. B., Luo Y., and Wang J. H., "Novel Laser Structures Based on MQW Interdiffusion Using Rapid Thermal Annealing Technique," *IEEE J. Selected Topics in Quantum Electronics*, vol. 4, no. 4, pp. 736-740, July/August 1998.

Lee J. K., Park K. H., Jang D. H., Cho H. S., Nam E. S., Pyun K. E., and Jeong J., "Improvement of Kink and Beam Steering Characteristics of 0.98μm GaInAs-GaInP High-Power Lasers Utilizing Channel Ion Implantation," *IEEE Photon. Technol. Lett.*, vol. 12, no. 2, pp. 140-142, Feb. 2000.

O'Brien P. A., Skovgaard P. M. W, McInerney J. G., and Roberts J. S., "Broad area semiconductor lasers with improved near and far fields using enhanced current spreading", *Elect. Lett.*, vol. 34, no. 20, pp. 1943-1944, October 1998.

Reithmaier J. P., and Forchel A., "Focussed Ion-Beam Implantation Induced Thermal Quantum-Well Intermixing for Monolithic Optoelectronic Device Integration," *IEEE J. Selected Topics in Quantum Electronics*, vol. 4, no. 4, pp. 595-605, July/August 1998.

Skovgaard P. M. W., O'Brien P., and McInerney J. G. ,"Inhomogeneous pumping and increased filamentation threshold of semiconductor lasers by contact profiling", *Elect. Lett.*, vol. 34, no. 20, pp. 1950-1951, October 1998.

Swint R. B., Woo C. Y., Huber A. E., Roh S. D., Coleman, J. J., Faircloth B. O., and Zediker M. S., "A Novel Separate Lateral Confinement Quantum-Well Heterostructure Laser," *IEEE Photon. Technol. Lett.*, vol. 14, no. 2, pp. 134-136, Feb. 2002.

Thornton R. L., Burnham R. D., Paoli T. L., Holonyak N., and Deppe D. G., "Low threshold planar buried heterostructure lasers fabricated by impurity-induced disordering," *Appl. Phys. Lett.*, **47**, (12), pp. 1239-1241, December 1985.

Welch D. F., Scrifes D. R., Cross P. S., and Streifer W., "Buried heterostructure lasers by silicon implanted, impurity induced disordering," *Appl. Phys. Lett.*, **51**, (18), pp. 1401-1403, November 1987.

Yu S. F., and Li E. H., "Semiconductor Lasers Using Diffused Quantum-Well Structures," *IEEE J. Selected Topics in Quantum Electronics*, vol. 4, no. 4, pp. 723-735, July/August 1998.

Chapter 6

Multi-Mode Interference Coupler Array Laser

6.1 Introduction

High power lasers are increasingly demanded by the opto-electronics industry. To overcome the limitations of single-element lasers, a common approach for obtaining high power is to use an array of low power elements, where inter-element coupling allows coherent locking of the array. However, these laser arrays can suffer from non ideal inter-element coupling and imperfections, both of which can cause elements to drop out of lock, causing instability and consequently poor performance. Furthermore, the near-field of most arrays is of little practical use, and the far-field undesirably multi-lobed. This chapter describes the development of a novel monolithically integrated array laser using a multi-mode interference (MMI) coupler to optically couple the active array elements. Figure 6.1 shows a conceptual diagram of the device investigated. This diagram shows the case for 2 active amplifiers and a 2:1 MMI coupler, though in general N amplifiers could be used with a corresponding N:1 MMI coupler. In one direction the MMI device works as a N:1 coupler (assuming the correct phase relationship), and couples the light from the N active amplifiers into the passive single-mode output waveguide. After reflection at the facet, the MMI device works as a 1:N splitter, thus

feeding the N amplifiers, and consequently forming a coupled cavity resonator. Since the power from the N active amplifiers is coupled into the passive single-mode output waveguide, this should ensure that the output is in a clean fundamental lateral mode. The power in this passive single-mode waveguide should be significantly larger than that obtainable with a typical single-element laser. The near and far-field characteristics from this single-mode output waveguide are far superior to those from a multi-element array output; the near-field is much more useful, especially for coupling into another waveguide. Alternatively, the output can be taken from the array end.

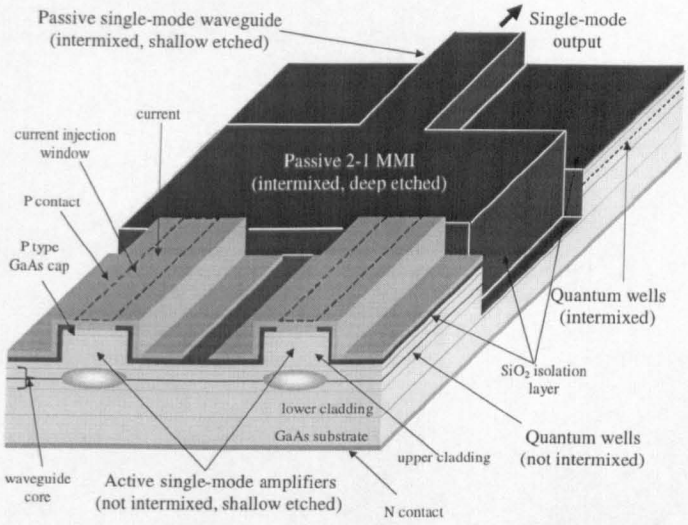

Figure 6.1: Schematic of 2:1 MMI coupled cavity array laser. Light from the 2 active amplifier sections is coupled into the passive single-mode output waveguide using the MMI section as a 2:1 coupler. For the return path the MMI works as a 1:2 splitter and feeds the two amplifiers, thus forming a coupled cavity array laser.

Integration of the active and passive sections is achieved using the quantum well intermixing technique described previously. Extracting large powers from narrow waveguides tends to cause mirror damage, leading to catastrophic optical damage (COD). However, as demonstrated in chapter 4, the QWI technology can be used to create non-absorbing mirrors (NAMs), increasing the power capability of facets. Therefore, that fact that the passive single -mode

output waveguide is intermixed and thus effectively a NAM should offer protection against COD.

Since the MMI coupler is an essential part of the device, section 6.2 describes the MMI and its application in integrated couplers. Section 6.3 gives an overview of array lasers. Analysis of the MMI coupler array laser is covered in section 6.4. Two generations of devices were designed, fabricated and tested. Section 6.5 describes the first generation device, whereas the more advanced second generation device is covered in section 6.6. Conclusions from the MMI array laser are drawn in section 6.7.

6.2 Multi-Mode Interference

Multi-mode interference (MMI) is a phenomenon of multi-mode waveguides whereby interference of the spatial modes along the length of the waveguide results in a self imaging effect and the possibility of generating multiple images of the original input. This effect is not just scientific curiosity, but has been applied to great effect in creating MMI devices capable of splitting and coupling signals, which have now achieved widespread use throughout the opto-electronic community. Following a suggestion by Bryngdahl (1973) regarding self-imaging using light pipes, Ulrich and Ankele (1975) described and demonstrated self-imaging and the ability to create multiple images in planar optical waveguides. Niemeier and Ulrich (1986) further advanced the technology by demonstrating a self-imaging directional coupler with single-mode fibre inputs. Following these early developments in MMI and self-imaging, many more research groups began to realise the potential of the technique for planar optical devices. It is beyond the scope of this section to cover the entire field of MMI, therefore the intention is to summarise the main concepts and applications, referring the reader to suitable texts should they require further detail.

To illustrate the concept of MMI and self-imaging in multi-mode waveguides a simple simulation was performed using the beam propagation method (BPM)

with software from Optiwave Corporation. Figure 6.2 shows the result of the simulation. A single-mode input was fed into the centre of a wide multi-mode waveguide section, thus exciting higher order lateral modes which interfere with each other as they travel along the length of the waveguide. At specific distances along the length of the multi-mode waveguide there exist single and multiple images of the input signal. For example, at a total distance of around 7.5 mm a single image can be seen (hence 6.5 mm of multi-mode waveguide), whereas at around 4.3 mm two self-images are visible. The ability to form multiple self-images is of great significance for splitting and coupling applications in planar optics. By suitable choice of multi-mode waveguide length and positioning of single-mode input and output waveguides, it is relatively simple to create a splitter or coupler. For example, Figure 6.3 shows how a suitable choice of multi-mode waveguide length and positioning of input/output waveguides allows signal splitting and combining. The BPM simulations shown here are for centre fed MMI devices, which represent just one possible configuration.

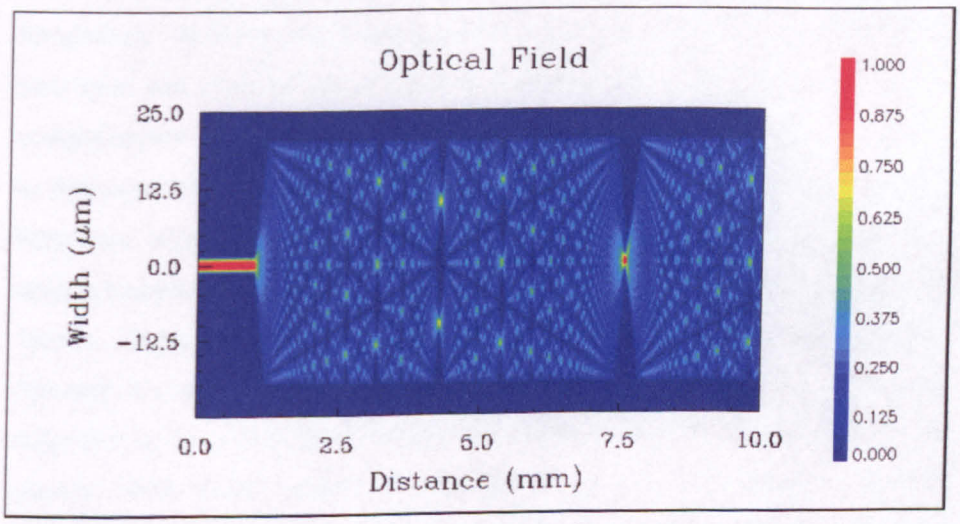

Figure 6.2: BPM simulation showing MMI pattern of a centre-fed 40 μm wide multi-mode waveguide (9 mm long) fed from a 3 μm wide single-mode input waveguide (1 mm long). Once the single-mode input enters the multi-mode waveguide section the mode excites higher order lateral modes which consequently undergo MMI as the light travels along the waveguide. The refractive index of the waveguide is 3.5, and outside the waveguide is air (n=1). The free-space wavelength of the light is 860 nm.

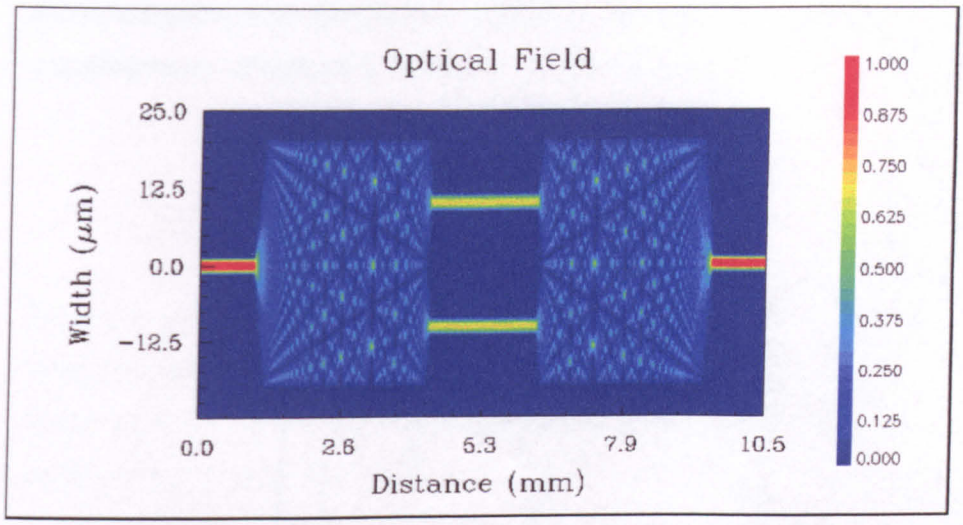

Figure 6.3: BPM simulation showing how the multi-mode waveguides can be used as splitters and couplers by suitable choice of waveguide length and positioning of input/output waveguides. This example shows how a 40 μm wide, 3.25 mm long multi-mode waveguide can be used in one direction as a 1:2 splitter and in the opposite direction as a 2:1 coupler. Two 2 mm long single-mode waveguides are used to pick off the two split images and feed them into the 2:1 coupler.

Smit (2002) highlighted the importance of MMI couplers for photonic integration. Soldano and Pennings (1995) gave an excellent overview of the principles and applications of MMI and self-imaging. Their paper includes a comprehensive description of the MMI effect, and hence the reader is referred to this paper should they require a detailed understanding of the phenomenon. Since the objective of this research involves using the MMI device as a splitter/coupler for the novel array laser, a symmetric N-way splitter was chosen. These restricted interference symmetric MMI devices have the benefit that only the even symmetry modes are excited in the waveguide, resulting in a reduction in the self-imaging length by a factor of four when compared to the generic MMI device which excites both even and odd modes. A brief description of symmetric self-imaging follows, using the analysis from Soldano and Pennings (1995), and Heaton *et al* (1992). Since our objective is to utilise practical devices, the intention is to give a brief understanding of the reason for MMI, and practical design equations/principles suitable for designing actual devices. Symmetric interference uses only the even order modes in the

waveguide, and is perhaps the most useful and practical form of MMI as it allows compact centre-fed 1-to-N way splitters and couplers. Figure 6.4 shows a representation of symmetric MMI in a multi-mode waveguide.

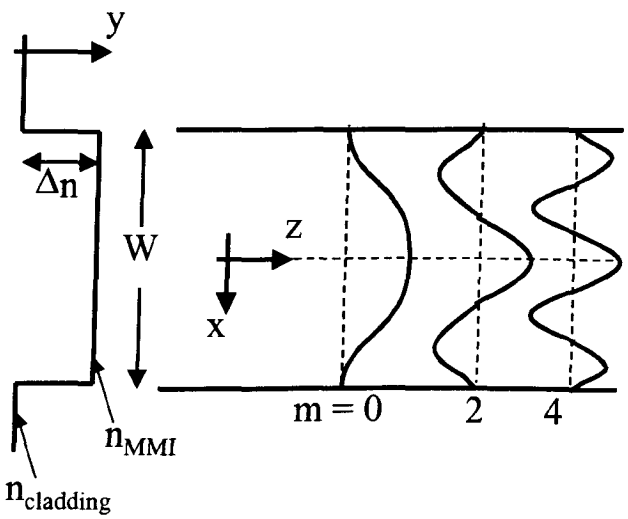

Figure 6.4: Cross section and plan-view of step-index multi-mode waveguide. The light is confined within the waveguide of width W, and propagates along the z-direction. The diagram shows even order modes for the case of symmetrical restricted interference in the waveguide. At any point along the waveguide the field profile is the summation of all the even order modes at that point. This diagram is an adaptation of figures by Soldano and Pennings (1995).

Returning to Figure 6.2, this is an example of symmetric interference. Since the single-mode input signal is fed to the centre of the multi-mode waveguide only the symmetric (even-order) modes are excited in the waveguide, hence the field amplitude $E(x,z)$ at a point within the waveguide is the sum of all the symmetric modes supported at that point, as shown in Eq. 6.1. The amplitude of the mode and the total number of guided modes are given by E_m and M respectively.

$$E(x,z) = \sum_{m=0,2,4,\ldots}^{M} E_m e^{j k_{zm} z} \cos\left(\frac{(m+1)\pi x}{W}\right) \qquad Eq.(6.1)$$

The propagation constant of the mth order mode is given by k_{zm}, which is given by Eq. 6.2, where n is the effective index of the planar waveguide and λ_0 is the free-space wavelength.

$$k_{zm} = k - \frac{(m+1)^2 \pi^2}{2W^2 k} \qquad \text{where} \qquad k = \frac{2n\pi}{\lambda_0} \qquad Eq.(6.2)$$

Returning to Eq. 6.1, it is apparent that self-imaging will occur at a distance along the waveguide if the term $k_{zm}\, z$ is an integer multiple of 2π for all of the supported modes at that point. Due to the quadratic dependence of k_{zm} with the mode order, it is apparent that for self-imaging to occur, the separation between propagation constants of the modes must therefore be an integer multiple of 2π, which consequently allows determination of the self-imaging length, Λ, as shown in Eq. 6.3. Therefore, a symmetric field profile repeats itself periodically along the multi-mode waveguide with a separation distance of Λ.

$$\Lambda = \frac{nW^2}{\lambda_0} \qquad Eq.(6.3)$$

Verification of this equation can be performed by simply inspecting the BPM simulation shown in Figure 6.2. Inserting the simulation parameters into Eq. 6.3 gives a value for 6.5 mm for Λ, which corresponds very accurately to the self-imaging length shown in Figure 6.2. Inspection of Figure 6.2 reveals that N equal amplitude self-images of pitch W/N are formed at certain points along the length of the multi-mode waveguide given by Eq. 6.4.

$$\text{distance to } N \text{ images} = \frac{\Lambda}{N} \qquad Eq.(6.4)$$

Figure 6.3 demonstrates the principle of using this multiple self-image generation for a 1:2 splitter of length $\Lambda/2$. Two suitably positioned 3 μm single-mode waveguides of pitch W/2 are positioned at the end of this $\Lambda/2$ section and thus the input signal is split into two signals of equal power. Due

to the symmetric nature of the multi-mode waveguide around $z=\Lambda/2$ it is therefore possible to use a section of length $\Lambda/2$ to couple the two signals into a single output waveguide, thus regenerating the original signal and demonstrating a 2:1 coupler.

Whilst it is true that for a 1:N splitter, N self-images of equal intensity will be formed at a distance Λ/N, these images do not necessarily have the same phase. Analysis of the phase relations is beyond the scope of this research and is covered by Bachmann *et al* (1994). The phases of the image pairs symmetric about $x=0$ must be the same, however for the case of more than two self-images there will exist a relative phase difference between image pairs not symmetric about $x=0$. For example, a 1:4 MMI splitter will create 4 equal amplitude images: I_1, I_2, I_3, I_4, with phases $\phi_1=\phi_4$; $\phi_2=\phi_3$; $\phi_1\neq\phi_3$. The case of the 1:2 MMI splitter is special; due to the symmetric nature of the two images, these images must have the same phase. This relative phase situation consequently manifests itself when using a N:1 MMI coupler; for efficient coupling into the single output waveguide, the amplitudes of the N input signals must be identical, and the relative phases must have the correct relationship. Effectively the N:1 MMI coupler is phase and amplitude sensitive. To illustrate this point, BPM simulations were performed on a 2:1 MMI coupler since this is the simplest type of N:1 MMI coupler. Figure 6.5 shows the results from the simulation. The amplitude and relative phase of one input signal was varied relative to a fixed input signal, and the coupling efficiency calculated by dividing the power coupled into the single output by the total input power. For the case when both inputs are identical, the coupling efficiency is 100 %, which is the case for the 2:1 coupler shown in Figure 6.3. Keeping the amplitudes equal, but varying the relative phases shows that the coupling efficiency is strongly dependent upon the relative phase; when the two inputs are 180 ° out of phase the coupling efficiency is 0 %, i.e. no power is imaged to the single-image point. When the phases of the two inputs are identical, and the relative amplitude of one of the signals is reduced it is apparent that the coupling efficiency gets smaller as the amplitude imbalance

increases, however this relative amplitude sensitivity is not as prominent as the phase sensitivity. When there is only a single input into the 2:1 MMI coupler it is apparent that the coupling efficiency is 50 %, i.e the device works as a 3 dB coupler.

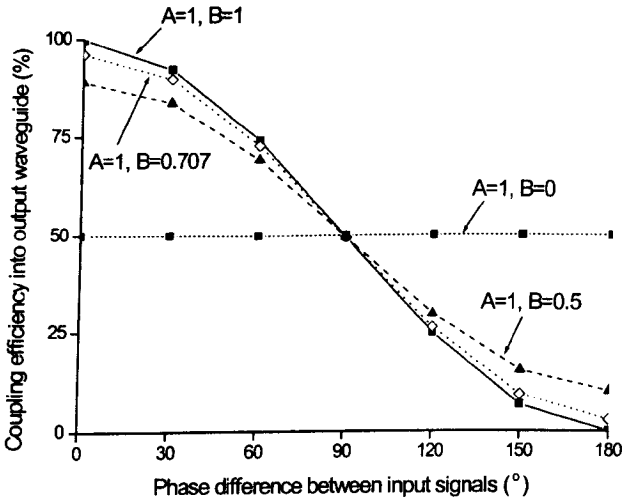

Figure 6.5: Results from BPM simulations showing how the coupling efficiency of a 2:1 MMI coupler varies with the relative amplitudes and phases of the 2 input signals (A and B). Input A was fixed (relative amplitude = 1), and the amplitude and phase of B was varied relative to A. The coupling efficiency is defined as the power coupled into a single-mode output waveguide divided by the total input power, i.e. the coupling efficiency is a measure of how well the 2 input signals are imaged to a single image.

From a practical point of view, MMI devices are compact and offer superior performance and relaxed fabrication requirements when compared to alternative coupler/splitters [Soldano *et al* (1995)]. The MMI device is compatible with the planar device technology commonly used for integrated optoelectronics, making it viable for exploitation. Soldano *et al* (1995) describe some of the various applications that MMI devices have been utilised for including: optical combiner for coherent receiver, out-coupler for a ring-laser and Mach-Zender interferometers. The paper also summarise results from various MMI devices fabricated from III-V semiconductors. Although active MMI devices have been reported [Hamamoto *et al* (1998)], current injection induced refractive index changes in the MMI section can disrupt the

MMI effect, hence the overwhelming majority of MMI devices are based on passive MMI sections.

6.3 Array Lasers

Monolithic array lasers have been investigated extensively by many groups in an attempt to overcome the performance limitations of single-element laser diodes. Carlson (1994) gave an excellent detailed review of monolithic laser diode arrays, and this is used as a source for much of the following discussion. Although the performance of high power single-element lasers is constantly improving due to improvements in laser design, fabrication and material quality, single-element devices will never be capable of achieving the performance levels required by some applications. Limitations for high power single-element lasers diodes include the following.

1) Catastrophic optical damage (COD): this is caused when the optical intensity at the facet is too high and consequently the mirror becomes permanently damaged. COD is discussed in chapter 4.
2) Lateral mode instability: although this is not such a problem when the objective is just creating a large amount of power, lateral mode instability tends to cause deterioration of the beam quality which is problematic for high brightness sources. The underlying reasons for lateral mode instability are explained in chapters 2 and 5.
3) Heating: since only part of the electrical input power is converted to optical output power, the remaining power is dissipated as heat. This heating can reduce the laser performance, and the device may undergo a thermal "roll-over" characteristic whereby heating causes the output power to decrease with increasing input current. Heating is particularly problematic in high power devices since the optical output varies linearly with the input current, whereas the resistive power varies with the quadratic of the input current, therefore as the input current increases, the heat dissipated by the device increases greatly. For high power lasers, the performance of the bonding technique and cooling play a vital part in determining the device capability.

6.3.1 Types of Monolithic Array Lasers

Monolithic array lasers can be differentiated into either coherent or incoherent arrays depending upon whether the elements in the array are coupled together or not. These two families of laser arrays have been developed with different performance objectives to meet their respective application requirements.

6.3.1.1 Incoherent Array Lasers

Incoherent laser arrays consist of a monolithically integrated set of laser elements which effectively have no optical coupling to each other. Individual laser elements can be considered to operate independently and hence there is no spectral coherence. Incoherent laser arrays are particularly useful when the objective is creating a high *quantity* of optical power for applications such as optically pumping a solid-state laser. Integrating a number of high power laser elements onto a single chip offers the potential to create very large optical powers. Such high power laser arrays need large drive currents and consequently dissipate very large quantities of heat, hence bonding and cooling are critical. Another type of incoherent laser array has individually addressable elements suitable for parallel reading and writing in optical disk storage, thus increasing the data rate achievable.

6.3.1.2 Coherent Array Lasers (Edge-Emitting Devices)

Coherent laser arrays are created when the array elements are optically coupled. This optical coupling means that the laser elements should all operate at the same wavelength (spectral coherence). Furthermore, the optical coupling should lock the elements together, resulting in stable lateral super-mode operation (spatial coherence). Typically, the objective for coherent arrays is to create significantly large *quality* power, suitable for the application. One of the difficulties for coherent arrays is maintaining coherence at high power levels. Since edge-emitting individual elements are typically capable of greater power levels than surface-emitting elements, this section will concentrate on coherent lateral edge-emitting arrays, and the following paragraphs summarise the most prominent concepts.

Lateral Optical Coupling

Leakage of light from one laser element into the neighbouring elements provides a very simple way to optically couple the entire array, and consequently achieve coherent operation. This type of array laser has been investigated by many research groups and, although such array lasers are capable of single wavelength operation, their beam-profiles are usually double lobed. The reason for these double lobed profiles resides with the lateral super-mode supported by the array; the gain/loss relationship of the array means that adjacent array elements are typically locked in anti-phase to each other, consequently resulting in the double lobed profile. The near-field of the array is of little practical use since it consists of multiple spots. A further limitation of this type of array is that the inter-element cross-coupling coefficients for the elements are not uniform across the array, and consequently elements near the edge of the array may drop out of lock.

Diffractive Section

Inter-element coupling for a lateral array of laser elements can be provided by a diffractive section. Upon entering this diffractive section, the light from each element mixes with the light from all the other elements, and this summation of light can either be reflected back into the array or feed another array of elements. This mixing of light in the diffractive section means that all the elements are effectively coupled to each other and consequently the array operates with spectral coherence. Of particular interest for array lasers is the case when the diffractive section is of a particular length and forms a Talbot cavity. As explained by Wilcox *et al* (1989), the Talbot effect can provide near-field self-imaging of a periodic source array (see section 6.2 for a discussion of self-imaging in multi-mode waveguides), hence an array of elements can be self-imaged to another array (or to the original array if reflected) and thus provide the inter-element cross-coupling required for coherent operation. Jansen *et al* (1989) used this self-imaging property of Talbot cavities to create a single-lobed beam-profile from an index-guided array of elements, where the diffractive Talbot section was electrically pumped

to avoid absorption. As will be explained in greater detail in section 6.4, Talbot array lasers are not ideal since the near-field is of little practical use, the inter-element cross-coupling coefficients are not ideal, and theoretically the far-field contains a sinusoidal envelope of lobes [Banerji *et al* (1997)].

Beam-Splitting Coupled Arrays

Array lasers based upon using optical splitters to couple only the adjacent array elements have been investigated as potential coherent sources, however the performance is far from ideal. The most common way to split the optical signal is to use Y-type couplers. Welch *et al* (1986) used this Y-coupler approach to coherently couple an array of in-phase index guided elements, which produced a beam profile with three dominant lobes (centre lobe had greatest magnitude). The main problem with this type of array architecture is that, since only adjacent elements are coupled, the array is extremely susceptible to non-uniformities i.e. a single non-ideal element can throw the entire array out of lock.

Anti-Guided Array lasers

Anti-guided array lasers were developed to be robust against the effects causing deterioration of coherent operation in laterally coupled array lasers. In anti-guided arrays, the gain elements have a significantly lower effective index than the regions between the gain stripes. Light generated by the gain stripes leaks into the adjacent higher index regions, and, since these are not injected with current, they are relatively free from index variations caused by the interaction of the gain and optical field. As explained by Botez *et al* (1991), integration of Talbot cavities into an array of anti-guides can further enhance performance, enabling high power dominantly single-lobed diffraction limited beams. As with the previous types of lateral array laser, the near-field is of little practical use, limiting the potential applications.

6.3.1.3 Alternatives to Edge-Emitting Array lasers

Due to the difficulties involved in obtaining stable high-powers from edge-emitting lateral arrays of laser elements, alternative approaches have also been investigated as briefly outlined in the following paragraphs.

Master-Oscillator Power Amplifier (MOPA)

Master-oscillator power amplifiers are based upon using a low power stable single-wavelength oscillator to drive a high power amplifier (or set of amplifiers). A low power signal from the master-oscillator is coupled into the power amplifier and then amplified to obtain a large power level. Ideally the master-oscillator and power amplifier are monolithically integrated. Since the master-oscillator is only driven at a low level, it is relatively free from spatial and spectral instabilities and thus can provide a very high quality single-wavelength input signal to the amplifier. The master-oscillator and power amplifier are separate parts of the devices (though integrated monolithically) and thus can be individually designed to meet their respective requirements. A common approach is to use a grating in the master-oscillator to ensure single-wavelength operation. A tapered active waveguide can be used for the power amplifier to allow large output powers and protect against COD. As explained by Osinski *et al* (1994), it is also feasible to use multiple amplifiers driven by a single master-oscillator to deliver even greater spectrally coherent powers. To ensure good performance from the MOPA, it is essential that the coupling between the master-oscillator and power amplifier is unidirectional such that very little light from the amplifier is injected back into the master-oscillator; if significant light is coupled back into the master-oscillator then the stability of the master-oscillator can be seriously impaired.

Surface Emitting Lasers

Surface emitting lasers have also been investigated as possible coherent sources. A suitably designed grating in an otherwise edge-emitting laser structure can allow out-coupling of the light through the surface of the device. Advantages of this distributed output coupling are that the optical intensity emitted at the surface can remain relatively low and the device can be scaled to

give higher power, though from a device fabrication point of view the grating makes the device relatively difficult to manufacture. An alternative way to achieve surface emission is to use sloped etched facets as out-coupling mirrors. Over the past few years, vertical cavity surface emitting lasers (VCSELs) have received much research attention. Although individual VCSELs have a poor power capability, creating 2-D arrays of closely packed VCSELs has the potential to significantly increase the power capability [Grabherr *et al* (1999)].

6.4 Analysis of MMI Coupler Array Laser

The motivation for developing the MMI coupled array laser was provided by the theoretical comparison of Talbot array lasers and 1:N MMI coupled array lasers by Banerji *et al* (1997). In their analysis, they developed a resonator model for each device type and used this to compare predicted device characteristics. Of particular interest is the comparison of the inter-element self and cross coupling coefficients. These coefficients determine how well each element in the array resonator is coupled to itself and the other array elements. Inter-element coupling coefficients have great significance when analysing array lasers; the coefficients determine how tolerant the array is to manufacturing and operational perturbations, which may result in destruction of coherent operation. Ideally all the inter-element self and cross coupling coefficients should be uniform across the array. Analysis of the Talbot cavity array laser shows that the inter-element coupling coefficients are far from uniform over the array. For example, for the case of 8 array elements, the distant neighbours do not couple at all. This non-uniformity of inter-element coupling coefficients is a typical problem in array lasers; the elements towards the edge of the array are poorly coupled to other elements and consequently drop out of lock. This usually limits the number of elements in the array over which all the elements are coherently locked. Furthermore, the fact that the inter-element coupling coefficients are not uniform means that the optical intensities within each element of the array will not be uniform, which may consequently impact on the device stability. In contrast, analysis of the MMI coupled array laser shows that all the self and cross coupling coefficients are

identical, and, as written by Banerji *et al* (1997), *"The equality of the coefficients means that no elements are discriminated against in the phase-locking process and the photon-mixing characteristics are as good as they possibly can be"*. This equality of the inter-element coupling coefficients should lead to much more stable coherent locking of the device and consequently increased coherent power capability.

Comparison of the near and far-field characteristics of the two array architectures predicted superior performance for the N:1 MMI coupled array laser, when compared to the Talbot array laser. The near-field of the Talbot array laser contains multiple spots, which is of very little practical use for integrated opto-electronics, and the far-field is undesirably multi-lobed. In contrast, taking the MMI coupled array laser output from the passive single-mode end gives just one single-mode near-field signal, which is potentially very useful for butt coupling into another waveguide. Since the power from the N active amplifiers is coupled into the passive single-mode output waveguide, this should ensure that this high power output is in a clean fundamental lateral mode. The far-field characteristic from this single-mode waveguide end should always be a Gaussian beam.

Following these predictions of device performance by Banerji *et al* (1997), a monolithically integrated MMI array laser was demonstrated by Camacho *et al* (1998) at the University of Glasgow. The device used 4 single-mode amplifier sections coupled to a passive single-mode waveguide using a passive 1:4 MMI coupler. Monolithic integration of the active and passive sections was achieved using QWI. The material system used for the experiment was GaAs/AlGaAs. Just a single contact was used to inject current into all of the 4 amplifier sections, hence the amplifiers were not individually addressable. Each amplifier was 1 mm long and 4 μm wide, with a separation of 2.5 μm. The 4:1 MMI section was 675 μm long and 26 μm wide. The single output waveguide was 325 μm long and 4 μm wide, making the total device length 2 mm. To protect against possible facet damage, 30 μm long NAM sections

were included at the ends of the 4 amplifier sections. A single RIE step was used to shallow etch the entire device to around 200 nm above the waveguide core region. Although shallow etching can be used for creating MMI couplers, it is not the ideal configuration since the index step between the waveguide and etched region is relatively small when compared to a deep etched MMI coupler (etched right through the core region). The small index step for shallow etched MMI couplers means that the optical mode in the coupler extends significantly outside the MMI coupler pattern, which consequently increases the length of the MMI section. From a practical point of view, the relatively small index step in shallow-etched MMI couplers makes them sensitive to the etch depth, hence inaccuracies in the etch depth can cause a change in the optimal MMI section length and result in poor MMI coupler performance. Shallow-etched MMI sections also tend to have fewer lateral modes supported in the MMI section, which can reduce the quality of the self-imaging. Even so, the device demonstrated 180 mW of output power from the passive single waveguide end. The threshold current was 120 mA, with a slope efficiency of around 10 % per facet. Although the far-field characteristic from the amplifier array end was poor, with multiple lobes, the pattern remained stable as the injected current increased, implying that the amplifiers were phase-locked. Since the MMI coupler is a phase sensitive device (see section 6.2 for an explanation of the MMI coupler phase sensitivity), coherent operation of the array requires that the amplifiers are locked together with the correct phase relationship into the 4:1 MMI coupler to achieve efficient coupling into the single output waveguide. For the case of the 4:1 MMI coupler array laser, the phase relationship of the MMI coupler means that a 180 ° phase shift must occur between the two inner and outer amplifier arms for optimal coupling. If this phase shift does not occur then, for the case of the 4:1 MMI coupler array laser, the phase relationship of the amplifiers into the 4:1 MMI coupler means that the coupling efficiency into the single output waveguide is low, resulting in poor device performance. However, since the device lased with a reasonable threshold current, Camacho *et al* (1998) commented that they believed that some form of self-adjustment occurred in the amplifier arms to allow coupling

into the single output waveguide. This self-adjustment should select the lowest threshold super-mode for the device, which consequently would require efficient coupling into the single output waveguide, hence phase locking of the amplifiers.

Further analysis of the aforementioned 4:1 MMI coupler array laser was performed by Avrutin *et al* (1999) from the University of Glasgow. Since the amplifier waveguides were shallow etched and only spaced by 2.5 μm, significant lateral coupling between the amplifiers was believed to have occurred; this directional coupling between the amplifiers could provide the phase shift between the inner and outer amplifiers. The analysis calculated the predicted external quantum efficiency of the device as a function of coupling strength between adjacent amplifier sections. Optimising the structure of the parallel amplifier waveguides could provide the phase shift required between inner and outer amplifiers to give a good phase relationship into the MMI coupler, and consequently increase the external quantum efficiency to over 50-60 %. This phase shift due to the lateral coupling between the amplifiers provides an alternative explanation to the self-adjustment phenomenon for why the device operated at a reasonable threshold current.

The objective of the research presented in this chapter is to further investigate the MMI coupled array laser. Research focuses on 2:1 MMI coupled array lasers, since these are the simplest to understand. As explained later in sections 6.5 and 6.6, two generations of devices were fabricated and tested. Since the 2nd generation device was the more advanced, and thus allowed better investigation of the MMI coupled array laser, the results presented focus on the 2nd generation device, though a brief discussion of the 1st generation device is also given. In order to attain a better understating of the device performance, both generations of devices were designed such that the amplifier sections were sufficiently separated such that any directional coupling between them is minimal, and consequently the MMI section provides the only inter-element coupling between the amplifiers. Simulations of directional couplers were

performed using the BPM technique described earlier in section 6.2. The simulations were performed for a pair of 3 μm wide shallow etched waveguides. The separation between the waveguides and the index step (defined by the etch depth) were varied and the coupling length noted. Results from these simulations predicted that, for the typical shallow etch depths used for creating single-mode waveguides, the coupling length should be in the order of 10s of milli-metres or more for a waveguide separation of 3 μm. The coupling distance increases greatly as the separation is increased, therefore using an amplifier separation of greater than 3 μm should ensure that the lateral coupling between the amplifiers is virtually eliminated and consequently the only inter-element coupling mechanism is provided by the MMI coupler. On the downside, using a large amplifier separation means that the width and the length of the MMI are increased.

6.5 First Generation Device

Figure 6.6 shows a representation of the 1st generation MMI coupler array laser investigated in this research. The device had 2 single-mode amplifier sections, coupled to the passive single-mode output waveguide using a passive 2:1 MMI coupler. To achieve lateral single-mode operation in the amplifiers and passive output waveguide, these waveguides were designed to be approximately 3 μm wide and shallow etched to around 100 nm above the core region. For fabrication simplicity, the entire waveguide structure was shallow etched in a single step. As explained previously, shallow etched MMI couplers are not the ideal configuration, though this construction makes the fabrication process much simpler. A single electrical contact was used to inject current through both amplifiers, hence they were electrically connected. A 5 μm wide separation between the amplifiers ensured that the MMI coupler provides the dominant coupling mechanism, thus limiting lateral directional coupling between the amplifiers. In many ways this 1st generation device was similar to the device demonstrated by Camacho *et al* (1998); the MMI coupler was shallow etched and the amplifiers were electrically connected, though there

were only 2 amplifiers instead of 4 and the directional coupling between these amplifiers was significantly reduced.

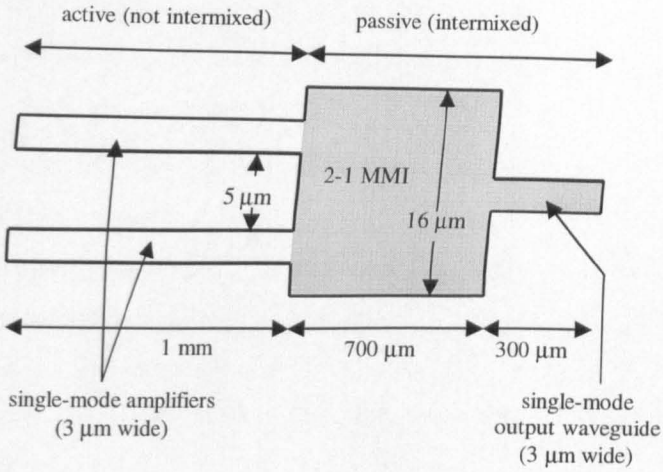

Figure 6.6: First generation 2:1 MMI coupler array laser. A single shallow etch step was used to etch the entire device waveguide structure. The two amplifier sections were electrically connected since only a single contact was used. A separation of 5 μm was used between the amplifiers to ensure that the dominant coupling mechanism is provided by MMI.

Fabrication of this 1st generation MMI coupled array laser was achieved using the same process sequence as the NAM laser described in chapter 4, incorporating the techniques described in the ridge waveguide laser chapter (chapter 2) and the QWI chapter (chapter 3). Therefore, in order to avoid repetition of the fabrication process description, the reader is referred to chapters 2 to 4. The material used for the laser was a standard GaAs/AlGaAs DQW wafer, described in chapter 2. For the laser results shown in this section, a 53 nm differential shift was achieved in the intermixing stage.

Figure 6.7 shows the lasing characteristics of the 1st generation device. The threshold current of the device was 250 mA, which is around twice that of the device demonstrated by Camacho *et al* (1998). This 1st generation device threshold current of 250 mA appears high since only 2 single-mode amplifiers were used. Part of the reason for the high threshold current could reside with the fact that the MMI section was shallow etched instead of the more preferable deep etching. However, Camacho *et al* (1998) also used a shallow

etched MMI. One possible explanation for the high threshold current could be due to a lack of stability since the amplifiers had very little coupling to each other through the lateral directional coupling mechanism. If the amplifier pair is not perfectly phase maintaining, then there will be a poor phase relationship into the 2:1 MMI coupler, and consequently very poor coupling into the single output waveguide, resulting in a high effective loss for the 2:1 coupling. Therefore, directional coupling between the amplifiers may be beneficial for array stability. However, this is just conjecture; in order to investigate the device operation further, 2nd generation devices with individually addressable amplifiers and deep etched MMI sections were investigated. Furthermore, the 2nd generation devices were developed at a later period of the research, and consequently the issues involved in achieving good fabrication were better understood.

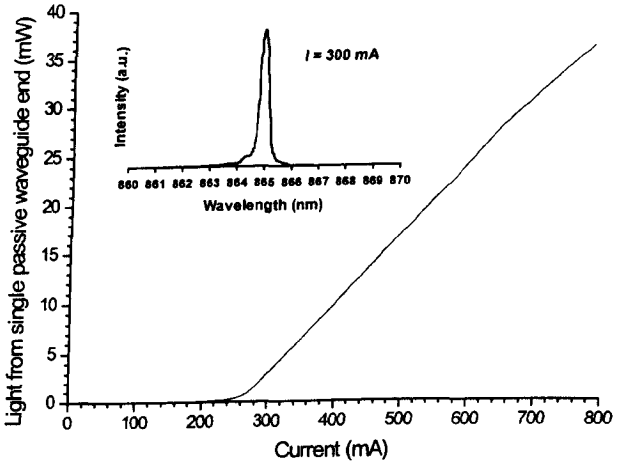

Figure 6.7: L-I characteristic from 1st generation 2:1 MMI coupler array laser. Inset shows the lasing spectrum of the device. Pulsed testing (see chapter 2) was used for extracting the characteristics.

6.6 Second Generation Device

6.6.1 Device Design

Figure 6.8 shows a schematic of the 2nd generation MMI coupler array laser; the device is very similar to that shown earlier in Figure 6.1. The device has two individually addressable amplifiers, and a deep etched MMI section (i.e. etched through the waveguide core region). NAMs were included at the facet end of the amplifiers to help protect against COD. To allow sufficient separation of the active contact pads, the amplifiers were placed 8 μm apart. This large separation should ensure that there is negligible lateral directional coupling between amplifiers; the only coupling mechanism is therefore provided by the MMI coupler. The single-mode active and passive waveguides were designed to be 3 μm wide, with an appropriate etch depth required to cut-off higher order lateral modes. Therefore, the MMI coupler was designed to be 22 μm wide. Potential inaccuracies in the fabrication process were accommodated by using a set of MMI couplers with lengths 870, 930, 990 and 1050 μm. To protect against undesirably deep etching a short length of a single-mode waveguide at the shallow etch to deep etch interface, the deep etched region was designed to be very slightly shorter than the MMI length; this reduces the tolerances required for the photolithographic alignment of the deep etch region, and reduces back reflections into the MMI coupler from the interface between the MMI coupler (deep etched) and the single-mode output waveguide region (shallow etched).

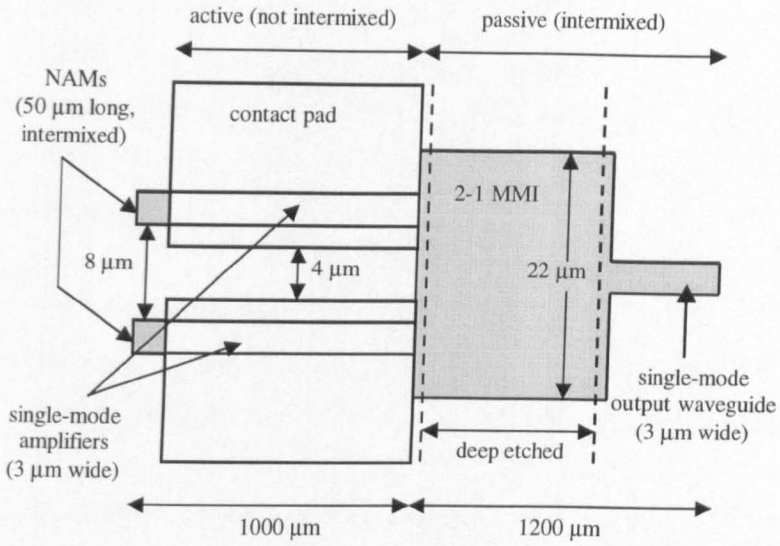

Figure 6.8: Schematic of 2nd generation 2:1 MMI coupler array laser.

6.6.2 Fabrication

Developing the fabrication process for the 2nd generation device required careful consideration; the process must incorporate a deep etch for the MMI coupler as well as a means to create individual contact pads. Alternative possibilities for integrating the deep etched MMI section with shallow etched single-mode waveguides were considered and the most promising solution selected. This solution is based upon defining the whole device in an initial shallow etch, followed by patterning and protecting the single-mode waveguide regions with photoresist, leaving the MMI coupler region exposed (no photoresist) and a subsequent second etch step results in deep etching the MMI coupler. Creating the individual contact pads is not particularly problematic as this can be achieved using a photolithographic lift-off process. A summary of the fabrication process sequence for the 2nd generation device follows. Individual processes used in this sequence have been described earlier in chapters 2, 3 and 4; the reader is referred to these should they require further details on the processes.

1) Alignment markers:

Use photolithography and $SiCl_4$ RIE to etch alignment markers into the sample. These markers make alignment of the subsequent photolithographic steps much easier and are essential when using QWI, since the interface between the QWI and non-QWI regions is virtually impossible to see.

2) Quantum well intermixing:

Create the QWI regions using the process described in chapters 3 and 4. After annealing the sample, the SiO_2 cap layer should be removed.

3) Pattern device structure and shallow etch:

Deposit 500 nm of PEVCD SiO_2 on the sample surface. Use photolithography (S1818 photoresist) to define the whole device waveguide structure, i.e. the single-mode waveguides (active and passive) and the MMI coupler. Transfer this pattern into the SiO_2 layer using CHF_3 dry etching. Remove the remaining photoresist with acetone. Use this SiO_2 etch mask to transfer the pattern into the laser sample using $SiCl_4$ RIE. This is the shallow etch and should stop approximately 100 nm above the waveguide core region; in-situ laser interferometery was used to accurately control the etch depth. After etching, do not remove the SiO_2 etch mask as this is required for the second etch of the MMI section.

4) Deep etch the MMI:

In the previous process step, the whole device including the MMI section was shallow etched. However, as explained previously, the MMI section must be deep etched through the waveguide core. A second etch of the MMI section is therefore required, making sure that the single-mode waveguides are not etched. This is achieved by using photolithography (S1818 photoresist) to cover and hence protect the

single-mode waveguides and leave the MMI coupler region exposed (no photoresist). The sample is then subjected to another $SiCl_4$ RIE step which deep etches the MMI coupler. Following this etch, the photoresist and SiO_2 etch masks are removed.

5) Contacts:

The electrical contacts are formed following the procedure in chapter 2. However, since definition of separate contacts is required, an additional photolithographic lift-off stage is performed. Before deposition of the p-contact metallization, photolithography is used to leave resist in areas where no metallization is wanted, and no photoresist in the contact pad regions. The p-contact metallization is then deposited. The sample is then soaked in acetone which dissolves the photoresist and hence lifts-off the metallization from areas not to be contacted. This only leaves the metallization on the contact pads as desired. Standard processing is then used to complete device fabrication.

Figure 6.9 shows the photoluminescence spectra from as-grown, suppressed and intermixed test samples. Successful intermixing was demonstrated by the 47 nm differential blue-shift between the intermixed and suppressed peaks.

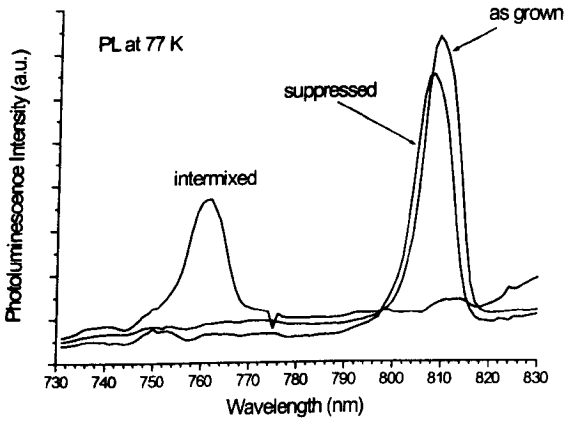

Figure 6.9: Photoluminescence spectra showing differential blue-shift achieved by intermixing. The intermixed and suppressed samples were annealed at 850 °C for 60 s.

An optical image of a fabricated 2nd generation MMI coupler array laser is shown in Figure 6.10. It is clearly apparent that the lift-off procedure worked well for devices since the only metallization is on the amplifier contact pads. The waveguides look well defined, and the interface between the deep etched MMI coupler and shallow etched waveguide is clearly visible.

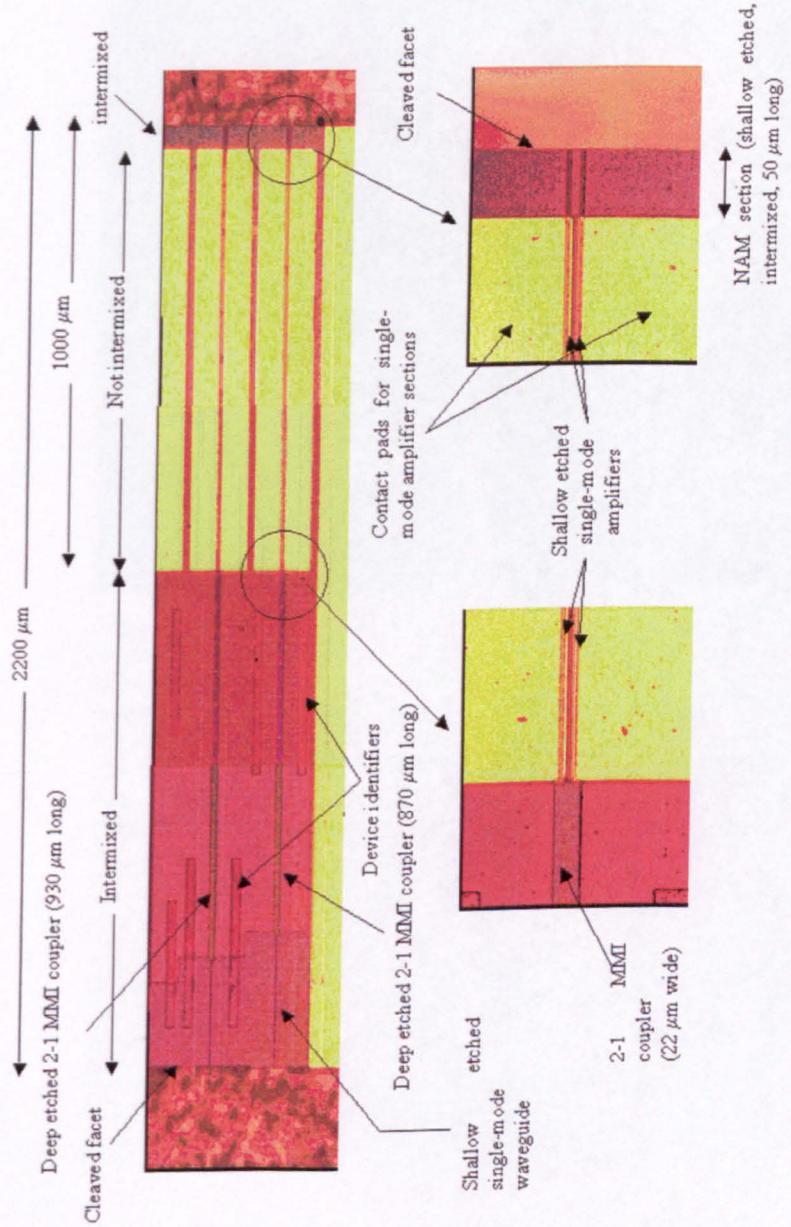

Fig. 6.10: Optical image of MMI coupler array laser. The image shows two adjacent devices with 2-1 MMI couplers of lengths 870 and 930 μm. The ridge width of the active and passive single-mode waveguide sections is 3 μm. Due to the large device size, the main image was built up from three separate images.

Figures 6.11 to 6.13 show SEM images from fabricated devices. Inspection of the images shows that the fabrication process worked very well. In particular, the etching appears good, giving well defined waveguides with almost vertical side-walls. The images show very little contamination or imperfections.

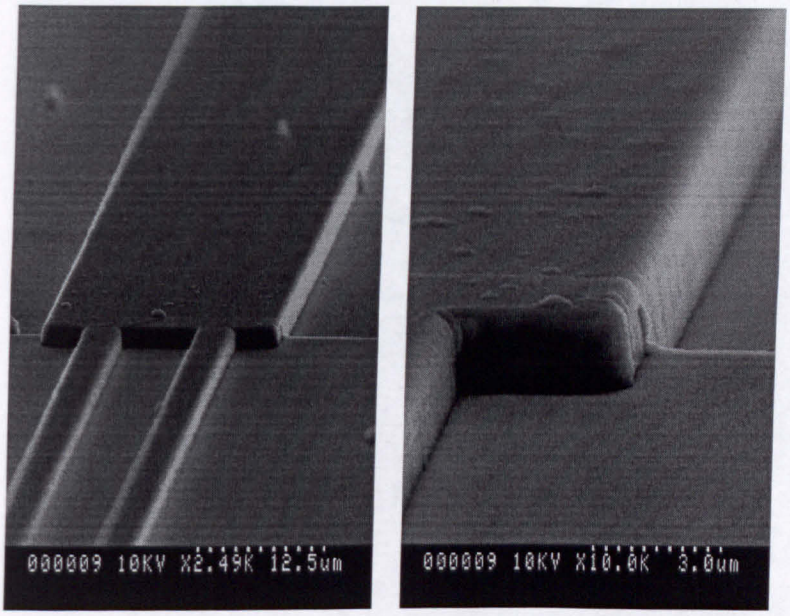

Figure 6.11: SEM images of the interface between a pair of shallow etched single-mode waveguides and the deep etched MMI coupler section. These images were taken from a completely passive device; the whole structure was intermixed and no contacts were used. The image on the right shows a higher magnification image of the shallow etch to deep etch interface. The etched side-walls appear almost vertical and smooth. The interface between the shallow etched single-mode waveguide and deep etched MMI coupler section is easily identifiable and demonstrates the viability of this fabrication process for integrating shallow etched and deep etched structures.

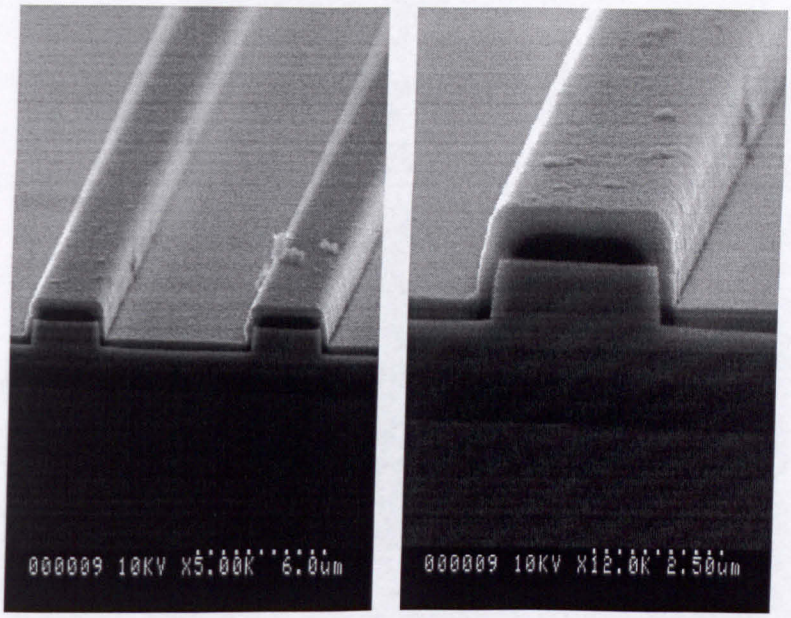

Figure 6.12: SEM image of the cleaved facet for a pair of passive single-mode waveguides. A higher magnification image of one of the waveguides is shown on he right. The single-mode waveguides look well defined, with smooth almost vertical side-walls.

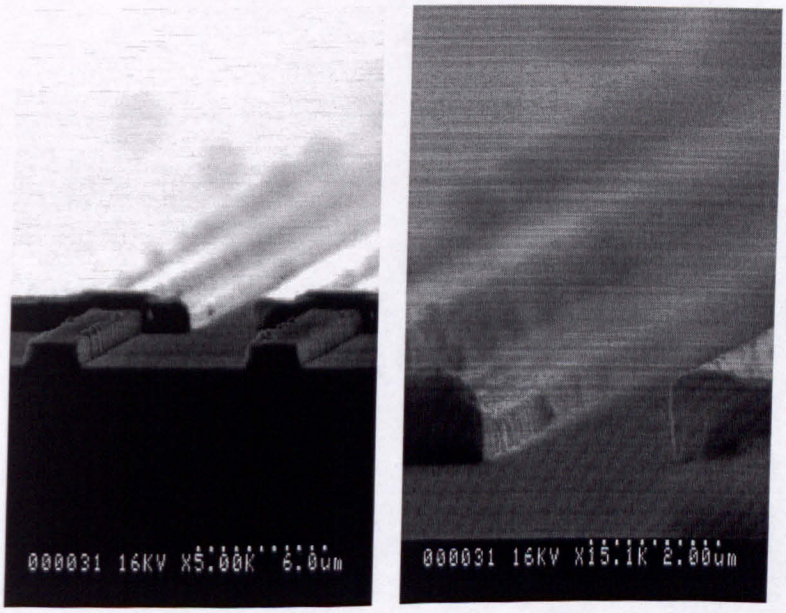

Figure 6.13: SEM images of the cleaved facet for a pair of single-mode amplifier waveguides. The contact pads are clearly visible on these amplifiers. Since the facet region is a NAM, the contact does not extend the whole way to the facet. The images show a clear separation of the contact pads, thus demonstrating that the lift off process worked well.

6.6.3 Passive MMI Coupler Measurement

To verify the operation of the passive 2:1 MMI couplers and single-mode waveguides, completely passive devices were fabricated alongside the MMI coupler array lasers. These passive devices had identical dimensions to the active devices, but the twin waveguides out of the MMI coupler were intermixed and no contacts were formed. A simple characterization of the passive devices was performed using an external Ti/sapphire laser operating at 860 nm. Light from this laser was coupled into the single waveguide end of the device, and the resultant near-field output from the twin waveguide end was inspected using a CCD camera. Figure 6.14 shows the measured near-field intensity profile from a passive device, with a MMI coupler length of 990 μm. Clearly the MMI has worked well as a 1:2 optical splitter, and is therefore likely to work well as a 2:1 coupler. Secondly, the modes appear well confined, proving that the passive shallow-etched waveguides are guiding well.

Figure 6.14: Near-field intensity profile from a passive 2:1 MMI coupler with single input waveguide and twin output waveguides.

6.6.4 Laser Characteristics

Lasing characteristics from the MMI coupler array lasers were extracted under various test configurations. First of all, the devices were tested using current injection into just one amplifier. The devices were then tested using current injection into both amplifiers. For each of these cases, the light was characterised from both facets. To clarify the characteristics, small illustrations of the device showing where current was injected and where the light was

measured are inset in the results figures. Devices were tested under the pulsed conditions described earlier. The laser results are from devices with an MMI length of 990 μm.

6.6.4.1 Current Injection Into Single Amplifier

Figure 6.15 shows the lasing characteristics out of the passive single-mode output waveguide facet for the case when only one of the amplifiers was injected with current. As demonstrated earlier in section 6.2, when only one of the two waveguides into the 2:1 MMI coupler has a signal, the MMI coupler works as a 3 dB coupler into the single output waveguide. For the return path, the MMI coupler works as a 1:2 splitter and hence 3 dB is coupled into the injected amplifier (the other 3 dB is coupled into the non-injected amplifier). Therefore, using just one amplifier, the device can perform as a laser resonator, but suffers an additional 6 dB loss, which explains the high threshold current of around 85 mA. The far-field beam profile characteristic shows dominantly single-lobed operation, which is precisely what was expected since the output was taken from the passive single-mode output waveguide facet.

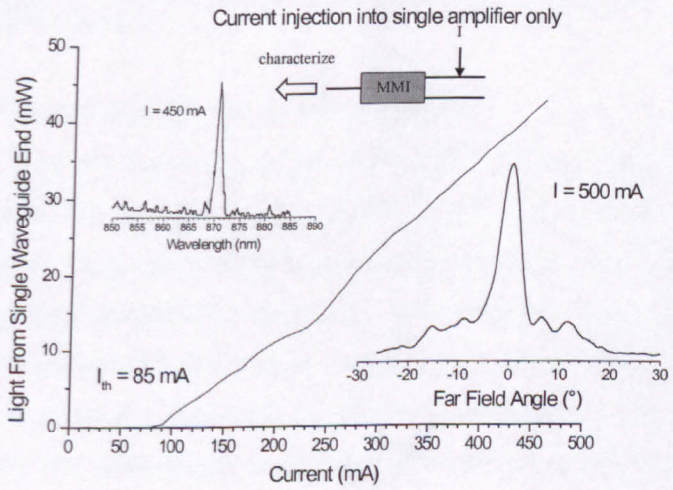

Figure 6.15: Laser characteristic measured out of single output waveguide facet for the case when only one of the amplifiers was injected with current. Inset shows the lateral beam profile and spectral characteristic.

Figure 6.16 shows the lasing characteristic from the amplifier end of the device for the case when only one amplifier was injected with current. As expected,

the threshold current is the same as when measuring the characteristic from the passive single output waveguide end of the device (Figure 6.15). Figure 6.16 shows that the beam profile is dominantly single-lobed, thus demonstrating that the amplifier operates in the fundamental lateral mode as desired.

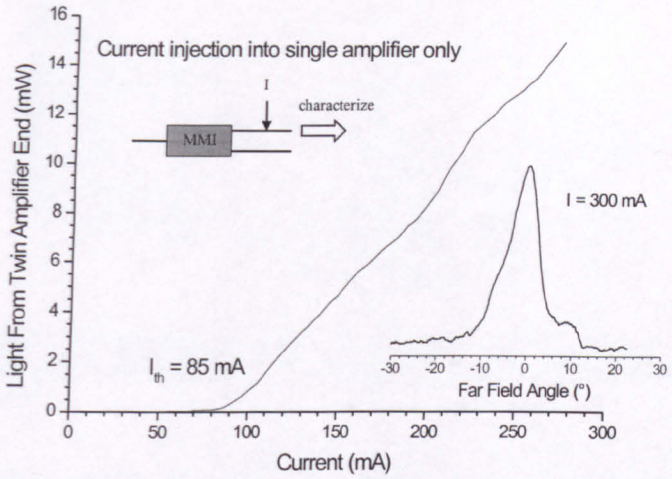

Figure 6.16: Lasing characteristic measured out of amplifier end for the case when only one of the amplifiers was injected with current. Inset shows the lateral beam profile measured.

6.6.4.2 Current Injection Into Both Amplifiers

Figure 6.17 shows the lasing characteristic from the single waveguide end of the device for the case when both amplifiers were injected with current. Both the amplifiers were driven from a single current source, hence the amplifiers were effectively electrically connected. The threshold current for the device increased to around 150 mA, almost double that for the case when only a single amplifier is injected. Although the device can be driven to a considerable power level, the beam-profile is not ideal; a dominant central lobe is evident, however there are also lower intensity peaks and the profile looks rather poor. The dominant central lobe is most likely the light guided by the single-mode output waveguide, however the source of the other peaks is not obvious and is discussed later.

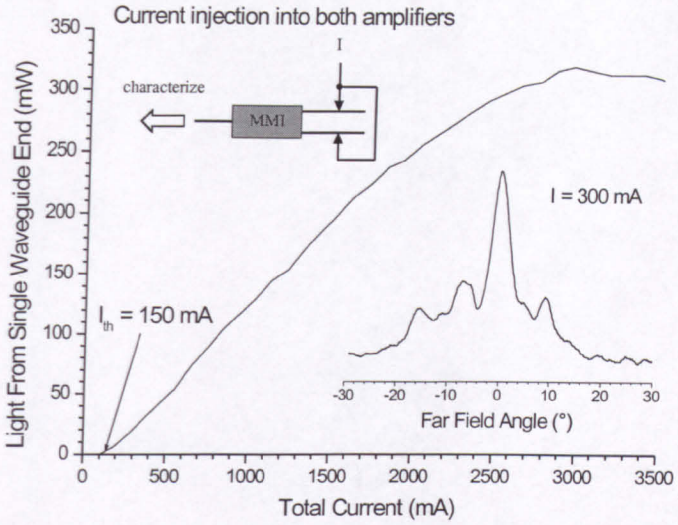

Figure 6.17: Lasing characteristic measured out of single waveguide end for the case when both of the amplifiers were injected with current. Inset shows the lateral beam profile.

Figure 6.18 shows the L-I and beam-profile characteristics out of the twin amplifier end of the device for the case when both amplifiers were injected with current (single current source, amplifiers electrically connected). The lasing turn-on characteristic is not sharp, however the L-I characteristic becomes linear as the injection current is increased. The beam profile shows multiple peaks for each of the injection current levels. Although a multiple peaked output is expected from this twin amplifier end of the device, the profile does not have a dominant central lobe, indicating that the amplifiers are not perfectly phase matched at the output facet; this is explained in greater detail later.

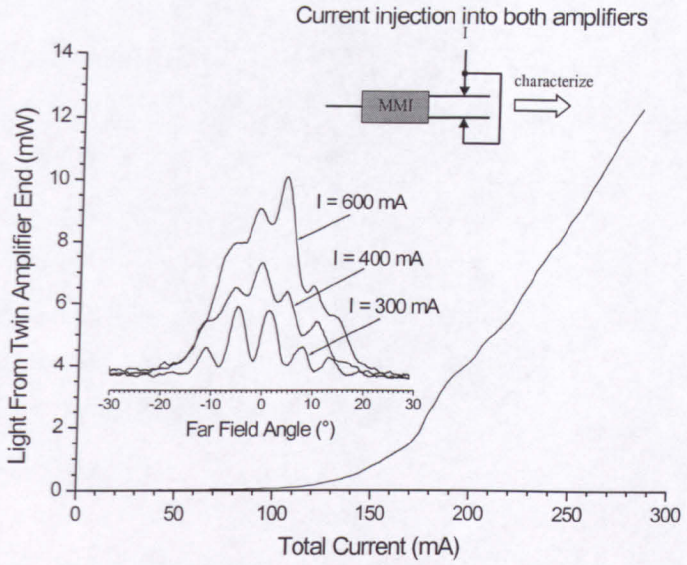

Figure 6.18: Lasing characteristic measured out of amplifier end for the case when both of the amplifiers were injected with current. Inset shows the lateral beam profile.

6.6.4.3 Discussion

First of all it is useful looking at the results from the case when only one of the amplifiers is injected with current (results in section 6.6.4.1). It is clear that the far-field beam profiles from both facets of the device are dominantly single lobed, which is entirely as expected since the index-guided active and passive waveguides were designed to operate in the fundamental lateral mode. It is apparent that the device can form a laser resonator when only one of the amplifiers is injected with current and therefore provides the gain. However, operating the device with only one injected amplifier gives an additional 6 dB loss due to the MMI coupler working as a 3 dB coupler in both directions, which explains the reason for the high threshold current of around 85 mA.

Results from when both amplifiers are injected with current (section 6.6.4.2) give an interesting insight into the device performance. First of all, consider that the threshold current increases from around 85 mA (single injected amplifiers) to 150 mA when both amplifiers are injected with current.

Therefore, injecting current into both amplifiers instead of just a single one almost doubles the threshold current. Consider now that if the amplifiers were perfectly phase locked (i.e. have zero phase difference along the amplifier length), then the MMI would have 100 % coupling efficiency into the single passive output waveguide, and that no light would be lost for the return path when coupling back into the two amplifiers. Therefore, if both injected amplifiers are perfectly phase locked then the device does not suffer from the additional 6 dB MMI coupler loss that afflicted the device when only a single amplifier was used. However, since the threshold current for the case when both amplifiers were pumped was almost twice that for the case when only one amplifier was pumped this provides evidence that the amplifiers were not ideally phase locking.

Beam-profile characteristics from both facets of the device when both amplifiers are pumped provide further evidence on the operation regime of the device. Consider the far-field from the twin amplifier facet (Figure 6.18); the beam contains multiple peaks and the profile changes as the injection current is increased. If the amplifiers were perfectly phase locked, the beam profile would contain a dominant central lobe and much smaller side lobes, however this is clearly not the case for the measured device. Furthermore, phase locked amplifiers would give a stable beam profile that does not change as the injection current is increased. These results provide further evidence that the amplifiers are not phase locked. Now consider the beam profile from the single output waveguide for the case when both amplifiers are injected with current (Figure 6.17); the profile contains a dominant central lobe believed to be due to light coupled into the passive single output waveguide. However, the profile also shows secondary peaks and considerable "noise"; these can be considered to arise as a consequence of non-ideal phase locking of the amplifiers. If the amplifiers were perfectly phase locked, all their power would be efficiently coupled into the single passive output waveguide (see Figure 6.5 for coupling efficiency of 2:1 MMI coupler for various pairs of inputs); this would result in a single lobed beam profile similar to that shown in Figure

6.15. However, since it is apparent that the ideal phase locking of the amplifiers is not occurring, the coupling efficiency into the single passive output waveguide would be considerably lower than 100 %, which raises the question of where the un-coupled light is going. Although the MMI coupler was designed to be deep-etched, to ease fabrication and avoid back-reflections the interface between the MMI coupler and shallow-etched single-mode waveguides was shallow etched (see Figure 6.8 for pictorial explanation). This means that light not coupled into the single passive output waveguide can leak out of the MMI coupler, and thus show up in the beam profile. Therefore, the origin of the secondary peaks and "noise" in Figure 6.17 is likely to be due to light not coupled into the single passive output waveguide as a consequence of non-ideal phase locking in the amplifier sections. Further evidence of light leakage from the interface between the MMI coupler and the shallow etched single-mode output waveguide region can be seen in Figure 6.15; although the beam profile shows a single dominant lobe, there is significant noise, which can be attributed to light not coupled into the single-mode output waveguide.

The lack of phase-locking in the amplifiers suggests that there was no "self-adjustment" phenomenon for minimizing the losses in the device. Since the amplifiers were sufficiently separated to minimize any directional coupling between them, the only optical coupling between the amplifiers was supplied by the MMI coupler. This lack of directional coupling between the amplifiers may explain the poor phase locking and stability displayed by the device; therefore it seems likely that directional coupling between the amplifiers is necessary to stabilise the device.

6.7 Conclusions

This chapter has described the development of a novel multi-mode interference coupled array laser using quantum well intermixing to monolithically integrate active and passive waveguide sections. Although the operating characteristics of these lasers were not as initially hoped for, the results give a useful insight into the device performance, thus permitting future improvements in the device

design. First of all, as explained in section 6.6.4.3, the lack of phase locking suggests that there is no "self-adjustment" phenomenon for minimizing the losses in the device. This lack of self-adjustment suggests that for the 4:1 MMI device reported by Camacho *et al* (1998) the phase adjustment between the amplifiers necessary for the device to lase was not due to self-adjustment, but rather directional coupling between the amplifiers. Since this device showed phase locking of the amplifiers, this suggests that the directional coupling between the amplifiers described by Avrutin *et al* (1999) was necessary for device stability; moreover, by optimising the coupling, the efficiency can be increased. The device investigated in this chapter was designed to have minimal directional coupling between the amplifiers, thus the only optical coupling between the amplifiers was provided by the MMI coupler; this lack of directional coupling may explain the poor phase locking and device stability. As predicted by Avrutin *et al* (1999), optimising the directional coupling between the amplifiers could maximise device performance and provide the device stability. However, in practice this is very difficult to do since the coupling strength between the amplifiers is very dependent upon the ridge etch depth, which usually varies run to run (unless an etch-stop layer is used in the material). Results from the devices highlight the difficulty involved in achieving coherent operation from an array of amplifiers.

6.8 References

Avrutin E. A., Camacho F., Bryce A. C., Hamilton C. J., Yanson D., Arnold J. M., and Marsh J. H., "Analysis of monolithic parallel-compound-cavity semiconductor lasers for high brightness, single-frequency, and short pulse operation", CLEO'99, Baltimore, USA, 23-28 May, 1999.

Bachmann M., Besse P. A., and Melchior H., "General self-imaging properties in N×N multimode interference couplers including phase relations", *Applied Optics*, vol. 33, no. 18, pp. 3905-3911, June 1994.

Banerji J., Davies A. R., and Jenkins R. M., "Comparison of Talbot and 1-to-N-way phase-locked array resonators", *Applied Optics*, vol., 36, no. 7, pp. 1604-1609, March 1997.

Botez D., Jansen M., Mawst L. J., Peterson G., and Roth T. J., "Watt-range, coherent, uniphase powers from phase-locked arrays of antiguided diode lasers", *Appl., Phys. Lett.*, vol. 58, no. 19, May 1991.

Bryngdahl O., "Image formation using self-imaging techniques", *J. Optical Society of America*, vol. 63, no. 4, pp. 416-419, April 1973.

Camacho F., Hamilton C. J., McIlvaney K., Bryce A. C., and Marsh J. H., "Laser structure for generating high optical power in a singlemode waveguide", *Electron. Lett.*, vol. 34, no. 5, pp. 460-461, March 1998.

Carlson N. W., "Monolithic Diode-Lasers Arrays," published by Springer, 1994.

Grabherr M., Miller M., Jäger R., Michalzik R., Martin U., Unold H., and Ebeling K. J., "High-Power VCSEL's: Single Devices and Densely Packed 2-D-Arrays", *IEEE J. Sel. Top. Quant. Electron.*, vol. 5, no. 3, pp. 495-502, May/June 1999.

Hamamoto K., Gini E., Holtmann C., and Melchior H., "Single transverse mode active multimode interferometer InGaAsP/InP laser diode", *Electon. Lett.*, vol. 34, no. 5, pp. 462-464, March 1998.

Niemeier Th., and Ulrich R., "Quadrature outputs from fiber interferometer with 4 x 4 coupler", *Optics Lett.*, vol. 11, no. 10, pp. 677-679, Oct. 1986.

Osinski J. S., Mehuys D., Welch D. F., Dzurko K, M., and Land R. J., "High-Power, Spectrally Coherent Array of Monolithic Flared Amplifier-Master

Oscillator Power Amplifiers (MFA-MOPAs)", *IEEE Photon. Technol. Lett.*, vol. 6, no. 10, pp. 1185-1187, October 1994.

Smit M. K., "InP Photonic Integrated Circuits", IEEE/LEOS Annual Meeting, Glasgow, November 2002.

Soldano L. B., and Pennings E. C. M., "Optical Multi-Mode Interference Devices Based on Self-Imaging: Principles and Applications," *J. Lightwave Technol.*, vol. 13, no. 4, pp. 615-627, April 1995.

Ulrich R. and Ankele G., "Self-imaging in homogeneous planar optical waveguides", *Appl. Phys. Lett.*, vol. 27, no. 6, pp. 337-339, Sept. 1975.

Welch D. F., Cross P., Scrifes D., Streifer W., and Burnham R. D., "IN-PHASE EMISSION FROM INDEX-GUIDED LASER ARRAY UP TO 400 mW", *Electron. Lett.*, vol. 22, no. 6, pp. 293-294, March 1986.

Wilcox J. Z., Simmons W. W., Botez D., Jansen M., Mawst L. J., Peterson G., Wilcox T. J., and Yang J. J., "Design considerations for diffraction coupled arrays of monolithically integrated self-imaging cavities", *Appl. Phys. Lett.*, vol. 54, no. 19, pp. 1848-1850, May 1989.

Chapter 7

Conclusions and Future Work

The research presented in this thesis has described how monolithic opto-electronic integration using quantum well intermixing (QWI) can be applied to improve the high brightness performance of ridge waveguide GaAs/AlGaAs QW lasers. High brightness semiconductor lasers are a subset of high power lasers, but with the emphasis on the *quality* of the light generated, typically giving a stable single-lobed beam profile. Although such lasers have requirements dependent upon the specific application, these lasers tend to have the following performance limitations: mirror degradation leading to catastrophic optical damage (COD), spatial mode instability, and overheating. Three distinct devices were investigated to suppress these performance limitations, illustrating the inherent flexibility of the QWI technology. Firstly, a laser with non absorbing mirrors (NAMs) was developed, where the NAMs suppress facet degradation. A ridge laser with a buried heterostructure was also investigated, where the de-coupling of the optical and electrical confinement can enhance fundamental mode operation by suppressing higher order lateral modes. Finally, an array laser using a multi-mode interference (MMI) coupler to optically couple the gain elements was investigated, which offers the potential to achieve high power in a stable fundamental mode.

Since all three of the investigated devices were based around standard ridge laser technology, the issues involved in developing single-mode ridge waveguide lasers were described. Lateral mode control was discussed, highlighting the advantage of an index-guided waveguide over a gain-guided waveguide. Index-guided lasers operating in a single lateral mode require careful design of the structure to ensure that the mode is well guided and that higher order lateral modes are not supported. Simulations of ridge waveguides were performed to determine appropriate ridge dimensions to achieve single-mode propagation. Fabrication of good quality lasers can be a whole topic in itself, and a suitable process for the fabrication of ridge waveguide lasers in the GaAs/AlGaAs system was demonstrated. Light-current and beam profile characteristics from the ridge laser showed that the laser operated as intended, giving single-mode operation in both vertical and horizontal directions, with good agreement to the simulations.

Since this research was concerned with the application of QWI to improve the high brightness performance of lasers, a selective process suitable for device manufacture was demonstrated. Promotion of intermixing was achieved using a thin layer of sputtered SiO_2 on the semiconductor surface, followed by high temperature annealing to intermix the QWs under the sputtered SiO_2 cap. Suppression of intermixing with respect to the sputtered SiO_2 area was achieved using a PECVD SiO_2 cap. Therefore, patterning the surface with sputtered SiO_2 and PECVD SiO_2, followed by subsequent annealing allows selective control of where intermixing occurs. Intermixing results from GaAs/AlGaAs DQW laser structures demonstrated the technology for producing large differential blue-shifts suitable for integrating passive intermixed sections with active as-grown sections.

Successful demonstration of a non absorbing mirror laser technology was achieved, which can significantly improve the power capability of high power lasers prone to mirror degradation and COD. Under pulsed test conditions designed to induce COD, the standard ridge laser suffered COD at an output

power of 230 mW/facet, whereas the NAM ridge laser suffered COD at 600 mW/facet, thus demonstrating an improved COD level by a factor of 2.6. This clear experimental evidence demonstrated the viability of this QWI process in creating high performance NAMs. The COD failure mechanism was confirmed by facet inspection, and removal of the damaged facets.

De-coupling of the optical and electrical confinement offers interesting benefits for semiconductor lasers, allowing greater flexibility in the device design and potentially superior performance. One possible implementation of the concept was demonstrated, using a ridge waveguide for the optical confinement, and a buried heterostructure defined by QWI for the electrical confinement. Experimental results demonstrated enhanced fundamental lateral mode operation up to higher powers when the buried heterostructure was used, indicating improved lateral mode discrimination due to the suppression of higher order modes. Furthermore, the improved lateral mode discrimination allows the ridge width to be widened and still operate in the fundamental mode, allowing the potential for reduced optical intensity at the facet, or greater COD levels, beneficial for high power operation. Comparison of standard ridge lasers and buried heterostructure ridge lasers with ridge widths of 5 μm clearly demonstrated the improvement gained. The standard ridge lasers were too wide to operate in the fundamental mode; the waveguide supports higher order modes, and the excitation of these cause modal instability and a poor beam. However, the buried heterostructure ridge laser showed dominantly single mode operation up to 130 mW/facet (the limit of the *L-I* measurement). Since the optical confinement was identical for both devices, this provides proof that the buried heterostructure helps reject higher order lateral modes. However, the "grass" on the buried heterstucture devices cannot be ignored; as the mode order increases it overlaps increasingly with the "grassy" region, hence if this region is lossy then the "grass" itself may help improve the lateral mode discrimination by increasing the losses of higher order modes relative to the fundamental. Although the "self-aligned" process developed for the lasers is conceptually straightforward and ensures perfect alignment of the buried

heterostructure to the ridge, the technique suffers from insufficient control of the buried heterostructure, thus limiting the laser design flexibility.

The third device investigated was a novel multi-mode interference coupled array laser using QWI to monolithically integrate active and passive waveguide sections. The MMI coupled array laser has the potential to generate large optical powers in a stable fundamental spatial mode, which is more usable than other types of array laser. In theory, the array laser benefits from ideal photon mixing characteristics, giving uniform inter-element cross-coupling coefficients across the entire array, which is advantageous for the array stability. Although the operating characteristics of the lasers were not as initially hoped for, the results give a useful insight into the device performance, thus permitting future improvements in the device design. The device showed unstable operation, with a lack of phase locking, suggesting there was no "self-adjustment" phenomenon for minimizing the losses in the device. Since the device investigated in this research was designed to have minimal directional coupling between the amplifiers, the only optical coupling between the amplifiers was provided by the MMI coupler; the lack of directional coupling may explain the poor phase locking and device stability. Therefore, it may be necessary to optimise the directional coupling between the amplifiers to achieve high power stable operation from the array, though this is difficult to do in practice since the coupling strength between the amplifiers is very dependent upon the ridge etch depth. Results from the MMI coupled array laser illustrate the difficulty involved in achieving coherent operation from an array of laser elements.

The research has highlighted the flexibility and capability of the QWI technique for monolithic opto-electronic integration. Three distinct devices were developed, all using the same QWI process and material. Results from the NAM laser and buried heterostructure ridge laser clearly showed improved performance in terms of the COD level and fundamental mode operation respectively. Although the performance of the MMI coupled array laser was

rather disappointing, a possible reason for this has been proposed, allowing future developments of the device to improve the performance. Indeed, the research has highlighted various avenues of future research, which are discussed in the following paragraphs.

The NAM laser performance could be improved by including good quality LR/HR facet coatings in the process; the coatings should lead to even higher COD levels, and better optimised output power from one facet. It would be interesting to perform life-time testing on a large batch of devices to investigate the long term degradation and reliability, however this research is of a more industrial nature, requiring additional equipment and a large number of devices. Another possible direction of future research would be to transfer the technology to other material systems prone to facet degradation.

Since the self-aligned buried heterostructure fabrication technique suffers from insufficient control of the buried heterostructure width, an alternative would be to use the extremely high alignment accuracy offered by electron beam lithography (EBL); this would allow totally independent control of the ridge and buried heterostructure, allowing improved flexibility in the laser design, though significant alteration of the fabrication processes would be necessary. If such a process was developed, it would be very interesting to investigate the modal stability as a function of the widths of ridge and buried heterostructure, allowing optimisation of the device design to maximise the fundamental mode power and stability. Additionally, an obvious avenue of future research would be to integrate NAMs onto the buried heterostructure ridge laser, thus creating a laser benefiting from QWI to suppress facet degradation and enhance fundamental mode operation.

Future research on the MMI coupled array laser should concentrate on achieving stable operation by attempting optimisation of the directional coupling between array elements. However, this places very high tolerance demands on the fabrication, which may make the task very difficult.

A possible direction of future research could be to investigate passive mode filters and expanders, which are longitudinally integrated with active gain sections. Since passive single-mode ridge waveguides do not support high order lateral modes, integrating a long passive single-mode waveguide with a length of gain region could be used to ensure that only the fundamental lateral mode propagates along the length of the device; the passive single mode waveguide acts as a mode filter by rejecting higher order lateral modes. In its simplest form, this just requires the NAM regions to be lengthened, and should ensure that the output is in a clean fundamental mode. One of the problems with the single element laser is the high optical intensity emitted at the facet, which causes facet degradation. Although a successful NAM technology was demonstrated, if even greater output powers are required, then a passive taper or diffractive section could be used to expand the optical mode at the facet, thus allowing an increased output power before COD occurs.

Photonic band-gap (PBG) technology is very powerful for monolithic opto-electronic integration, and has received much interest over the past few years. Therefore, combining the PBG and QWI technologies is an obvious route for future research, and should allow even more advanced devices, for example, the integration of passive PBG structures with active gain sections. Furthermore, the PBG technology may have the potential to significantly improve the performance of high brightness and high power lasers. One possible device to investigate is an array of gain elements embedded in a PBG structure, where inclusion of defect states in the PBG structure between the gain elements could be used to achieve controllable lateral optical coupling between the gain elements, thus creating a novel type of array laser.